# University of Southampton Research Repository

UNIVERSITY OF SOUTHAMPTON

Faculty of Physical Sciences and Engineering

Optoelectronics Research Centre

# Design and Fabrication of Novel Polymer Antiresonant Waveguides

DOI:

by

Lieke D. van Putten

ORCID ID 0000-0002-4428-1727

A thesis submitted for the degree of Doctor of Philosophy

February 2019

UNIVERSITY OF SOUTHAMPTON

## ABSTRACT

Faculty of Physical Sciences and Engineering
Optoelectronics Research Centre

Doctor of Philosophy

by Lieke D. van Putten

Over the past twenty years, hollow core fibres have been one of the most exciting innovations in optical fibre technology. Hollow core fibres have extended the optical properties achievable in conventional step-index fibres and open up new applications such as nonlinear optics. Despite numerous breakthroughs, the fabrication process of such fibres remains time consuming and costly.

This thesis describes the use of additive manufacturing as a fabrication method for hollow core fibre preforms and waveguides. I explore the use of polymers, which can be 3D printed using the inexpensive fused deposition modelling technique. As polymers have high absorption across the electromagnetic spectrum, I focus on hollow core fibre designs. Using finite element simulations, I propose a novel antiresonant fibre design that can be fabricated using additive manufacturing. The detailed simulations of this design give a new understanding of the effect of the cladding elements' curvature has on the leakage loss of the structure.

Several fibre preforms are successfully fabricated using different polymers. To understand the drawing process required for these materials, systematic drawing experiments are performed to aid the understanding of the fundamental differences between glass and polymer fibre fabrication. I developed a fluid dynamics model that is validated experimentally to predict the polymer capillary drawing process, taking into account the Non-Newtonian shear-thinning behaviour of these materials.

To further demonstrate the capabilities of additive manufacturing for photonic components, I design, fabricate and characterise a novel hollow core waveguide for the terahertz regime. These waveguides have the potential to replace costly terahertz components and detailed simulations suggest their attenuation can be improved by orders of magnitude with improvements in the quality of the fabrication process.

# Contents

# List of Figures

# List of Tables

# Abbrevations

| | |
|---|---|
| **ABS** | Acrylonitrile Butadiene Styrene |
| **ARF** | Antiresonant Fibre |
| **BVP** | Boundary Value Problem |
| **C-H** | Carbon-Hydrogen |
| **CAD** | Computer Aided Design |
| **CPU** | Central Processing Unit |
| **FD** | Finite Differences |
| **FDM** | Fused Deposit Modelling |
| **FEM** | Finite Element Method |
| **FEP** | Fluorinated Ethylene Propylene |
| **FFT** | Fast Fourier Transform |
| **FM** | Fundamental Mode |
| **GUI** | Graphical User Interface |
| **HC** | Hollow Core |
| **HOM** | Higher Order Mode |
| **ID** | Inner Diameter |
| **IVP** | Initial Value Problem |
| **MCVD** | Modified Chemical Vapor Deposition |
| **OD** | Outer Diameter |
| **PBG** | Photonic bandgap |
| **PC** | Polycarbonate |

| | |
|---|---|
| **PDE** | Partial Differential Equation |
| **PLA** | Polylactic Acid |
| **PML** | Perfectly Matched Layer |
| **PMMA** | Polymethyl Methacrylate |
| **POF** | Plastic Optical Fibre |
| **RI** | Refractive index |
| **SLA** | Stereolithography Apparatus |
| **SLS** | Selective Laser Sintering |
| **SRS** | Stimulated Raman Scattering |
| **SMF** | Single Mode Fibre |
| **SNR** | Signal to Noise Ratio |
| **STL** | Stereolithography |
| **THz-TDS** | Terahertz Time Domain Spectrometer |
| **TIR** | Total Internal Reflection |

# Declaration of Authorship

I declare that this thesis and the work presented in it is my own and has been generated by me as the result of my own original research. I confirm that:

- This work was done wholly or mainly while in candidature for a research degree at the University of Southampton;
- Where I have consulted the published work of others, this is always clearly attributed;
- Where I have quoted from the works of others, the source is always given. With the exception of such quotations, this thesis is entirely my own work;
- I have acknowledged all main sources of help;
- Where the thesis is based on work done by myself jointly with others, I have made clear exactly what was done by others and what I have contributed myself
- Parts of this work have been published in the conference proceedings and journal articles as listed in the List of Publications.

Lieke Dorine van Putten

February 2019

# Acknowledgements

I would like to express my sincere gratitude to my supervisors Prof. Francesco Poletti and Dr. Eric Numkam Fokoua. At challenging times during my PhD they have always been supportive and understanding and the help they have given me during my project has enabled me to complete this project. I would also like to thank Xian Feng and Joris Lousteau, who have both helped me and supervised me before they moved on from the ORC. I am very grateful to have been given the opportunity to do this project, for which I would like to thank the Engineering and Physical Sciences Research Council for the funding to support my PhD.

It has been a great pleasure to work with Francesco's group and I would like to thank all group members for their support during my PhD. I would especially like to thank Dr. Joris Lousteau, Dr. Walter Belardi, Dr. Xian Feng and Nick White for assisting me with the polymer fibre drawing experiments.

I would also like to thank Dr. Vasilis Apostolopoulos and Jon Gorecki from the Terahertz Laboratories, for helping me with the characterisation of the terahertz waveguides and the useful discussions we had about the results.

Working in the ORC has been an amazing experience and I have made many friends along the way. I have had the privilege of being part of the ORC's student outreach team Lightwave and have enjoyed working with this team. I learned a lot about presenting to different audiences and had so much fun at all the different activities. While the whole team has been an incredible joy to work with, I would like to thank Matt, Jake, Dean, Andrei and Callum for always being inclusive and making arrangements however complicated for me to be able to take part. During my time at the ORC I also met John and Ali who have both helped me tremendously. I am grateful for their support and friendship. John inspired me to learn to code in Python, as well as to use version control, which has proven to be a great skill not only for programming, but also to keep track of the progress in my thesis.

Although Nell, my amazing Canine Partner, has only been part of my life during the last phase of my PhD, I would also like to thank Canine Partners and all their volunteers, especially Nell's puppy parent and family, for making our partnership possible. Nell has given me a new independence and supported me in many ways while I was writing this thesis. I am also very grateful for the support I received from the Koning Willem Fonds to enable me to remain independent.

Last but not least I would like to thank all my friends for their support. They have been there for me and never stopped encouraging me, however bumpy the road may have been. I would not have been able to get this far without them. I especially want to express my gratitude to James for his support over the last few years. Thank you for motivating me, believing in me and being there for me on this journey.

# Chapter 1

# Introduction

## 1.1 Motivation

Fibre optics are the backbone of our interconnected society. Hundreds of millions kilometres of single mode silica fibres span our planet, and it is forecasted that by the end of 2021 these fibres will carry around 3.3 zettabytes of data traffic each year [1]. However, long-haul data transmission is not the only area where fibres are of great use, there is also a wide variety of short-range fibre applications. These applications include, but are not limited to, biomedical diagnostics, navigation systems and high-power laser applications for the manufacturing industry, such as laser cutting, welding and cladding.

Conventional step-index single mode fibres consist of a core with a high refractive index, surrounded by a cladding with a lower refractive index. Light is guided through total internal reflection (TIR) at the interface between the two materials. Although these fibres have been used successfully for many applications, there are limitations in solid core fibres due to the fundamental limits imposed by the interaction between the propagating optical waves and the solid materials. As a result, the waves are slowed down compared to propagation in a vacuum and their intensity dissipates due to scattering. Furthermore, increasing the optical power in the fibre causes problems too. Firstly, when the incident power is high, the oscillatory response of the bound electrons of the glass molecules is no longer proportional to the driving optical field. As a result, non linear phenomena become present. Although this could be useful for certain application, it is detrimental when it comes to optical communications as the wavelength of the propagating light can be converted and noise is generated. This effect is also known as the non-linear Shannon limit. Secondly, amorphous glasses suffer irreversible damage when subjected to very intense optical fields in the fibre due to the heat generated.

To overcome these limitations, hollow core (HC) fibres are of great interest to researchers. In HC fibres the light is guided in an air-filled core that is surrounded by a microstructured cladding designed to confine light to the core of the fibre. Light guidance in air afforded by HC fibres opens up new opportunities in a variety of applications. HC fibres are the ideal medium in which light can propagate free of interactions with a solid material that dissipates the signal and creates noise, thereby limiting the data-carrying capacity. Furthermore, they offer an ideal platform for delivering intense radiation without non-linear distortions or damage to the fibres, and can also allow controlled interactions between light and gases.

Compared to step-index fibres, HC fibres have a higher damage threshold and low nonlinearity due to the light propagating in air [2; 3]. At the same time, HC fibres can be used to control interactions between light and gases to study and create non-linear effects [4]. Furthermore, as only a small part of the light propagates in the cladding, HC fibres and waveguides can potentially achieve low losses at wavelengths where the solid material has high losses [5; 6]. The bulk loss in polymers and glasses is usually high for the terahertz regime, so HC waveguides could be a suitable solution to create low-loss waveguides for these frequencies.

The fundamental difference between step-index fibres and HC fibres is the guiding mechanism. There are two different operating mechanisms that can be used for HC fibres: the photonic bandgap (PBG) and antiresonance. I will discuss the guiding mechanisms of different fibre types in more detail in Chapter 2, but in short it can be said that the cladding structure of the HC fibre plays the main role when it comes to the fibre's performance. The cladding is designed to enable low-loss propagation at the desired wavelengths, by using thin membranes that surround the central (hollow) core and provide a high reflection to confine light in the core. The reflection coefficient of these membranes depends on the refractive index of the cladding material, the thickness of the membrane and the wavelength of the light propagating through the fibre. HC fibres have seen enormous improvements in the last decade with regards to the lowest attenuation achieved. Initially, research focussed on PBG fibres for HC fibre applications as these fibres had promising characteristics for data-transmission. However, with the latest developments in antiresonance fibres (ARF), this fibre type is gaining more and more interest and there are many research groups that work on ARFs, for example the Department of Photonics Engineering at DTU, the department of Physics at the University of Bath and the Optoelectronics Research centre in Southampton. Numerical simulations have shown that ARFs can outperform any existing technology at nearly every wavelength [7]. So far, HC PBG fibres have demonstrated losses as low as 1.7 dB/km [8] as well as high capacity data transmission [9]. Antiresonant fibres (ARF) have recently achieved losses as low as 1.3 dB/km [10]. Although these results are promising, currently available fabrication techniques for HC fibres can be time-consuming and costly.

Whilst fibre optics have seen an enormous development, the field of additive manufacturing has also witnessed advances over the past two decades. An increasing range of materials can now be used for processes such as 3D printing, including polymers, ceramics and even some metals [11].In this work, I explore the feasibility of using 3D printing as a manufacturing method of low-loss HC optical fibre preforms for subsequent drawing on a fibre tower. Currently, 3D printing of optical glasses is still an area that needs more development, as the glasses usually have a very high softening temperature and it can be difficult to shape them. To the best of my knowledge, reports of successful 3D printing of optical grade glass are limited, though recently this area has started to develop. A group at MIT demonstrated a process where glasses can be processed using a set-up similar to a 3D printer [12]. Kotz et al have printed a nanocomposite using stereolithography 3D printing. The printed nanocomposite is converted via heat treatment to high-quality fused silica [13].

Although there are difficulties in printing optical glasses, the 3D printing of polymers is well developed. Polymers have lower softening temperatures and can easily be shaped up to a few tens of micrometres resolution, depending on the printing technique used, with the help of computer-aided design (CAD) tools [13]. The aim of this project was to explore the use of these technologies and to use 3D printing for the fabrication of HC fibre preforms. Continuing improvements in the optical properties of polymers, combined with the relaxed requirements in HC fibres due to the core consisting of air, make polymer 3D printing an excellent platform for inexpensive HC preform and waveguide fabrication. This process could open up a variety of new applications, ranging from short-haul data links to HC fibre-based components for wavelengths where glasses and polymers are opaque. Even more important, this technique could allow for rapid prototyping of fibre designs, and ultimately identifying the optimal fibre designs faster, as the fabrication cycle is significantly shorter.

Creating fibres for the visible and near-IR regime using 3D printing is not the only potential application for the fabricated preforms. Without a drawing process, these preforms could be used as waveguides for the terahertz regime, due to the longer wavelengths at these frequencies. Waveguides for the terahertz regime could be used for microscopy, terahertz quantum-cascade lasers, and imaging [14], but could also be useful in spectroscopy applications to replace complicated lens systems. The invention of terahertz spectroscopy opened up a range of applications, including the analysis of interactions between molecules [15; 16].

## 1.2 Highlight achievements

Key contributions from this thesis include the following:

- Novel design antiresonant HC fibre using semi-elliptical cladding elements
- New insight into the effect of the curvature of the cladding element on the leakage loss of the antiresonance fibre
- Inexpensive fused deposition modelling printing of HC fibre preforms, and subsequent analysis of print quality. Systematic studies of post-fabrication quality improvements through thermal annealing.
- New theoretical model of polymer capillary drawing, taking into account the shear-thinning behaviour of Non-Newtonian materials. This model is validated using experimental results
- Fabrication through 3D printing and characterisation of novel HC antiresonant waveguide design for operation in the terahertz regime

## 1.3 Outline of this thesis

After this brief introduction into the work presented in this project, the remainder of the thesis is organised as follows:

Chapter 2 discusses the relevant technological background for the work presented in this thesis, particularly focusing on:

- the applications and guiding mechanisms of HC fibres, their optical properties and the fabrication process
- different techniques of additive manufacturing and the specific requirements these techniques must meet to be applied to the production of HC fibres
- polymers suitable for optical devices
- HC polymer fibres

Chapter 3 describes the modelling of wave propagation in a waveguide and the finite element method as a tool to solve the wave equation. A novel HC fibre and waveguide structure is proposed. The design uses half ellipses in the cladding design. The use of half-ellipses enables the study of the effect of the curvature of the core boundary on the leakage loss of the waveguide. Using the finite element method an optimum curvature for the half ellipses in the cladding and a new insight in the leakage loss through the cladding elements is found.

In Chapter 4 the progress towards fabricating fibres from 3D printed preforms is reported. Using Polycarbonate and Poly(methyl methacrylate) as well as the standard polymers ABS and PLA for 3D printing, different preform structures are printed and tested. A new theoretical model is used to describe polymer fibre fabrication and validated using capillary drawing experiments with two different polymers.

In Chapter 5 3D printing is utilised to manufacture an antiresonant waveguide for applications in the terahertz regime. Several waveguides have been fabricated and characterised. Imperfections caused by the limitations of the printer available are studied in more detail in the post-fabrication analysis, showing possible improvements of orders of magnitude in the waveguide's performance when the print quality can be improved.

In Chapter 6 the conclusions of the previous chapters are summarised and possible directions for future research into this field are suggested.

# Chapter 2

# Background

In this chapter I will give an overview of the relevant technological background for this project.

The first section describes HC fibres, more specifically antiresonant fibres (ARF) in more detail. The applications that HC fibres can open up and the historical development of HC fibres are discussed. I will also look into ARFs and their operating mechanism in more detail. The fabrication process for HC fibres will be discussed, and polymer fibres and their applications will be introduced in greater detail.

After that, different 3D printing techniques are discussed and selected for the purpose of manufacturing optical fibre preforms. A literature review of the state-of-the-art work in 3D printing of polymer optical devices and an overview of polymers suitable for fibre optics and additive manufacturing is given.

In the last section of this background chapter, the use of HC waveguides for the terahertz regime is discussed. As HC fibres can operate in frequency ranges where the material's absorption is high, HC waveguides could solve the problems in finding suitable waveguides for the terahertz regime.

## 2.1 Hollow core fibres

In this section HC fibres and their applications are described. For the type of HC fibres studied in this thesis, antiresonant fibres (ARF), the guiding mechanism is studied in more detail and the different fabrication methods are described.

### 2.1.1 Applications

As stated in the introduction, guidance in a hollow-core frees the light from deleterious interactions with bulk materials, potentially bringing vast improvements in many applications whilst enabling several new others.

Firstly, the absence of bulk contributions to loss imply that these fibres could potentially offer lower attenuation than the standard single mode fibre [17]. Such loss levels have not yet materialised in the more established hollow-core photonic bandgap fibre, with lowest reported attenuation levels standing at 1.7dB/km and fundamentally limited by scattering from surface roughness [8]. Nonetheless, several ground breaking experiments have demonstrated high capacity low latency data transmission in fibre samples as long as 11km [18] and over 70 km in recirculating loop experiments [19]. Current HC fibres are thus slowly establishing themselves as serious contenders for communication applications where loss is not the limiting consideration. Furthermore, numerical simulations have shown that surface roughness scattering is significantly reduced in antiresonant fibres [20], and many structures have been proposed with predicted loss levels below that of the standard single mode fibre. This has fuelled a resurgence into developing HC fibres specifically for the purpose of long-haul optical communications.

Secondly, the low fraction of power carried in glass results in nearly three orders of magnitude reduction in optical non-linearity when compared to single-mode fibres [21] and a significantly increased laser damage threshold. These features uniquely position HC fibres as ideal candidates for applications in high-power laser delivery, with demonstrations of successful delivery of power levels in excess of 70W [22; 23]. The reduced optical non-linearity and backscattering in HC fibres are extremely attractive for ultra precise fibre-optic gyroscopes for rotation sensing and navigation applications. In [24] Fini et al report a polarization-maintaining HC fibres for the purpose of rotation sensing and [25; 26].

Beyond these applications where HC fibres bring significantly improved performance, they also uniquely enable new ones, for example by constituting a unique platform for controlled and enhanced light interaction with gas/liquid species. Benabid et al have reported electromagnetic induced transparency [27], stimulated Raman Scattering and later octave-spanning frequency combs in hydrogen-filled HC fibres [4]. Filling HC fibres with noble gases has also led to the demonstration of high-power tunable supercontinuum pulses for wavelengths where conventional sources don't exist [28]. Light interaction with gases and liquids in HC fibres has further been exploited for sensing [29].

By lifting requirements on the transparency of the optical materials, HC fibres are extremely attractive for spectral regions where common materials are almost opaque, for example at very short (UV) or very long wavelengths (THz). Low loss guidance of optical waves at these wavelengths enable a wide range of applications from healthcare diagnostics, imaging to spectroscopy [30].

This wealth of potential applications is what has fuelled research on HC fibre technology over the past two decades .

### 2.1.2 History

The first concept of HC fibres was studied over a century ago by Lord Rayleigh [31]. Rayleigh had studied different aspects of waves, including lightwaves, sound waves and waves in fluids [32]. In the study that led to the concept of HC fibres, he studied the propagation of waves in hollow tubes, an attractive idea in his time, where no transparent and low loss medium existed for guiding light, he found that certain modes existed for which the waves could propagate in the hollow tubes [31; 32]. He also found that the limitation for the wavelengths of the waves propagating in the tubes were directly related to the size of the waveguide [32].

Although there was still an interest in the propagation of waves in hollow media, it took a few decades for the idea to gain more applications and interest [32]. In the 50s and 60s considerable attention was devoted to the development of metallic HC waveguides for millimetre wave propagation. In 1964, the concept was extended to a hollow dielectric waveguide which was studied theoretically by Marcatili et al [2]. A schematic overview of this waveguide is shown in Figure 2.1. They studied the mode propagation and field configuration in a hollow circular waveguide and concluded that sufficiently low propagation was possible for a core diameter significantly larger than the wavelength. In 1978, this design was improved upon by Yeh et al, who proposed the concept of Bragg reflections in waveguides to obtain lower losses. It was shown that modes could be confined by utilising these Bragg reflections in a medium with lower dielectric constants than the material surrounding this medium [33]. In 1976 they used the same principle to design a hollow core fibre surrounded by alternating cladding layers. The cladding layers thickness and refractive indices can be chosen to transmit certain wavelengths [34]. This fibre design is known as the 'Bragg Fibre' [34]. In Figure 2.1 an example of this type of fibre is shown.

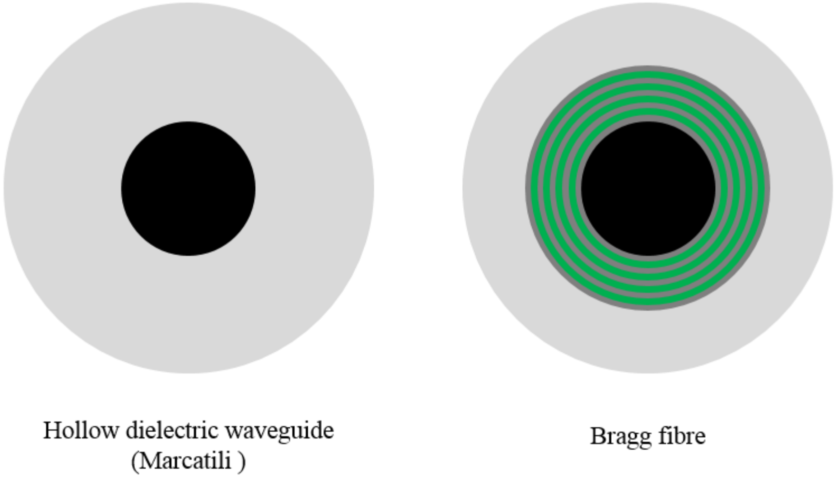

FIGURE 2.1: Schematic overview of Marcatili's HC waveguide, a circular air-hole surrounded by a dielectric (left) and HC Bragg fibre, a circular air-hole surrounded by periodic layers of two materials (with a different refractive index) (right).

In 1980, the first hollow metallic waveguide was fabricated for the infrared regime. The rectangular waveguide was made out of inexpensive aluminium sheets and was flexible [35]. Due to the high power-threshold of the fibre it was and still is a suitable option for high-power laser transmission. Garmire et al show in their paper that the transmission efficiency of the fibre for a $CO_2$ laser is over 80% over a length of 1.2 m [35].

In 1987 the concept of the photonic bandgap (PBG) was discovered [36], which inspired concepts of hollow-core photonic bandgap fibres. In hollow core PBG fibres, the core is surrounded by a periodic arrangement of air holes. The period of such an arrangement and the refractive index of the glass material together determine a spectral window for which no states are allowed in the cladding, i.e. the photonic bandgap. Light at those wavelengths is therefore effectively confined and guided in the fibre core [37]. The first PBG fibre was fabricated at the University of Bath in 1999, with a cladding consisting of stacked silica tubes [38]. Although the very first fibre had very high losses, it was a remarkable breakthrough. With the concept proven experimentally, the challenge then became to reduce attenuation. In 2003 Smith et al fabricated a PBG fibre with a hexagonal core surrounded by stacked silica tubes with a loss of 13 dB/km at 1500 nm [5]. This loss was reduced to a minimum of 1.7 dB/km at 1565 nm in 2004 by Mangan et al [8]. This low loss has held the record until this year, using a different type of fibre: the antiresonant fibre (ARF).

The loss in ARF fibres has been steadily decreasing. In 2017, the lowest loss achieved with a single-ring tubular lattice ARF was 7.7 dB/km at 750 nm. Although this is still far off the performance of silica fibres, nested elements have been theoretically studied and it has been shown these nested elements can reduce the loss. The challenge in the nested elements lays in the fabrication methods. Gao et al fabricated a fibre in 2018 with conjoined tubes in the cladding, reducing the loss to 2 dB/km at 1512 nm [7]. More recently, the ORC reported a new record for the lowest loss in a nested ARF where the loss was as low as 1.3dB/km [10], breaking the record from Mangan et al in 2004.

Since the late 90s, the field has progressed tremendously with different guiding mechanisms, materials and applications actively researched by groups across the world. The guiding mechanisms can be divided into subcategories, two common types are the PBG fibre and the ARF discussed in this section. In Figure 2.2 both fibre types are shown.

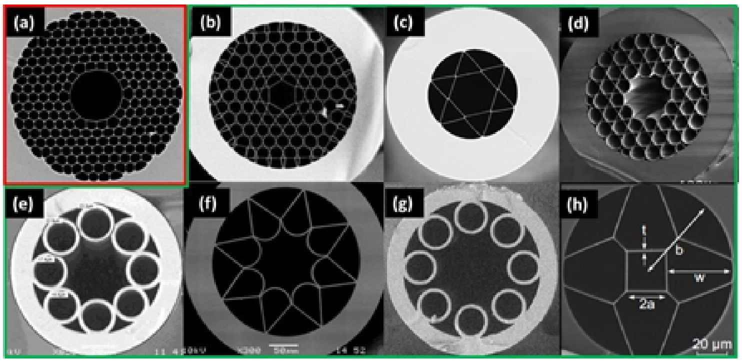

Figure 2.2: Cross-section of various HC fibres, antiresonant and simplified HC with negative curvature. Reprinted with permission from [20]. 2.2a shows a photonic bandgap fibre [39], 2.2b shows a large-pitched kagome structured ARF [40], 2.2c shows a hexagram ARF [41], 2.2d shows a kagome-type ARF with a hypo-cycloid core surround [42], Figure 2.2e [43], 2.2f [44], 2.2g [45] and 2.2h [46] all show ARFs with negative curvature core surrounds.

Both PBG fibres and ARFs can be made using different cladding designs. One antiresonant structure for low-loss transmission is the stacked tubes in a jacket, as shown in Figure 2.2e and 2.2g. This fibre is also called a simplified HC fibre with negative curvature [20]. In Figure 2.2b and 2.2d a Kagome cladding type fibre is shown. Figure 2.2c and 2.2h show antiresonant fibres with a hexagram cladding in 2.2c and a double antiresonant cladding in 2.2h [20].

Although PBG fibres have been studied longer than ARFs, recent theoretical works suggest ARFs can outperform PBG fibres when it comes to loss [7]. Compared to PBG fibres, ARFs have a wider bandwidth, as PBG fibres only have a bandwidth of 10-30% of their operating wavelengths, whereas the bandwidth of ARFs can be as wide as an octave [20]. ARFs also have simpler structures and therefore these structures are more suited for fabrication by additive manufacturing, which will be discussed in the next section. As a result, the work in this project is focused on ARFs whose physical principle of guidance I expand in the following section.

### 2.1.3 Guiding mechanism in antiresonant fibres

The fundamental difference between a step-index fibre and a HC fibre is the guiding mechanism. In a step-index fibre, the guiding mechanism is based on Total Internal Reflection (TIR). The core of the fibre has a higher refractive index (RI) than the cladding, and as a result the light is confined in the core by TIR. For HC fibres, TIR can not be the guiding mechanism, as the RI of the air-filled core is lower than the RI of the cladding. In an antiresonant fibre (ARF), the guiding mechanism is based on antiresonance. Essentially, the core is surrounded by an arrangement of thin membranes of solid material whose thickness is chosen so that it highly reflects incident light at the wavelength of interest [47; 48].

In an ARF, the thin membranes in the cladding surround a central hollow core region and provide high reflection to confine and guide light in the hollow-core. The transmission and the reflection coefficient of these membranes depend on the thickness and RI of the material and the wavelength of the light in the fibre. To aid the understanding of the antiresonance, I consider transmission through a membrane with thickness $t$ and a RI of $n_2$ surrounded by a medium with a RI of $n_1$, where $n_1 < n_2$, as shown in Figure 2.3. Such a thin membrane behaves as a resonator (a Fabry-Perot etalon) whose transmission coefficient, $T$, depends on the reflectivity of each interface, $R$, as well as the phase difference, $\delta$, accumulated between any two transmitted rays [49]. In Figure 2.3 a schematic overview of the transmission and reflections in this membrane are shown. The transmission coefficient for a thin membrane is defined as [50]

$$T = \frac{(1-R)^2}{(1-R)^2 + 4Rsin^2(\delta)} \tag{2.1}$$

Where R is the intensity reflection coefficient at a single air-membrane interface and the phase-shift delta is given as [50]

$$\delta = \frac{2\pi}{\lambda} \times n_2 \times t \times cos(\theta) \tag{2.2}$$

A maximum in transmission occurs when the phase shift satisfies the following condition [50]:

$$\delta = \frac{2\pi}{\lambda} \times n_2 \times t \times cos(\theta) = m\pi \text{ for } m = 1, 2, 3.. \tag{2.3}$$

where m is an integer. At grazing incidence ($\alpha$ very nearly equal to 0° as shown in Figure 2.3) the angle of refraction can be found using Snell's law and one obtains:

$$sin(\theta) = \frac{n_1}{n_2} \tag{2.4}$$

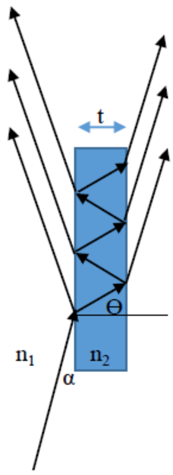

FIGURE 2.3: Fabry-Perot membrane with thickness $t$ and RI $n_2$.

Therefore, $cos(\theta)$ can be approximated using:

$$cos(\theta) = \sqrt{1 - \frac{n_1^2}{n_2^2}} \tag{2.5}$$

So the phase shift can be rewritten to:

$$\delta = \frac{2\pi t}{\lambda}\sqrt{n_2^2 - n_1^2} \tag{2.6}$$

Using Equation 2.3 the resonance wavelengths can be found:

$$\lambda_m = \frac{2t}{m} \times \sqrt{n_2^2 - n_1^2} \tag{2.7}$$

Using Equation 2.1 the transmission and reflection coefficient can be plotted as a function of the normalised frequency. The normalised frequency is defined using:

$$f = \frac{2t}{\lambda}\sqrt{n_2^2 - n_1^2} \tag{2.8}$$

Using the normalised frequency, the criterion for optimum transmission is:

$$f\pi = m\pi \tag{2.9}$$

In Figure 2.4, an example of the transmission and reflection coefficients is shown. Using a membrane with a thickness of 0.45 µm consisting of a material with a RI of 1.45, surrounded by air ($n_1 = 1$) and with an intensity reflection constant of 0.94 (the reflectivity constant for an incident angle of 89°, grazing incidence as shown in Figure 2.3. It can be seen that there are several windows with a high reflection and an equal number of high transmission peaks. The high transmission peaks match with the criterion given in Equation 2.9, as they are all located at an integer normalised frequency. These peaks are also called resonance peaks. At resonance, the transmission of the thin membrane is very close to unity. Therefore, in a fibre setting, light coupled into the core easily escapes through the membranes, resulting in a high loss peak. In contrast, at antiresonance the transmission through the thin membrane is low. As a result, light coupled in the core is confined in the core by antiresonance.

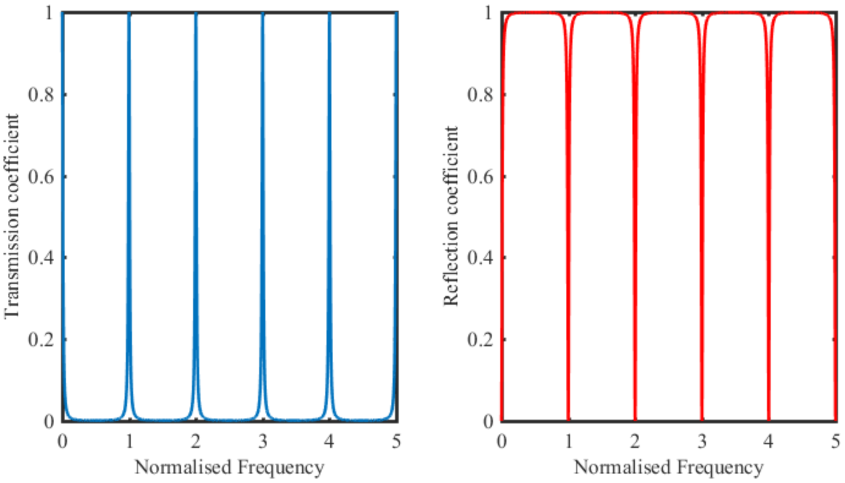

FIGURE 2.4: Transmission and reflection plotted as a function of the frequency for $n_1$=1, $n_2$=1.45, R=0.94 and t=0.45 µm.

In an ARF, the thin glass elements behave exactly as these membranes at grazing incidence. Therefore, within an antiresonant window, they provide high reflection to confine the light within the hollow core. Equation 2.1 shows that the minimum of T is $((1-R)/(1+R))^2$ for a single membrane, implying that a fibre will suffer from a loss known as leakage loss. Leakage loss however isn't the only source of loss in an ARF, in the next section I will examine other sources of loss in HC fibres.

### 2.1.4 Loss in antiresonant fibres

Equation 2.7 is one of the key starting points when designing an ARF, as the membrane thickness and RI can be chosen in a way such that the operational wavelength of the fibre lies between the high loss resonant wavelengths [20]. Within antiresonance windows, the light guided in the core is effectively reflected by the thin membranes and remains confined in the core. When designing the fibre, it is also important to study the attenuation in the fibre, as many applications require low-loss fibres. Origins of loss in HC fibres can come from absorption and scattering in the bulk materials, contributions from scattering (or indeed absorption) at the interfaces, leakage loss and extrinsic sources of attenuation such as bending loss or imperfection in the fibre structure.

In ARFs, only a small fraction of the light travels through the cladding elements, and as a result absorption and scattering in bulk loss is negligible.

Scattering loss in ARFs is due to light scattering from the membrane-air interfaces, which is dependent on the roughness of the surface of the structure inside the ARF. The loss contribution from roughness scattering is believed to impose a fundamental limit to loss values achievable in PBG fibres [51; 52]. In ARFs at antiresonance the electromagnetic field on the membrane-air interface is minimised, which reduces the contribution from scattering loss at antiresonance [20]. As a result of this, leakage is still the dominant source of loss in ARFs [51].

Leakage loss, also commonly referred to as confinement loss, is the loss due to the light escaping through the cladding elements via tunnelling. The leakage loss in ARFs depends on the cladding structure. As shown in Figure 2.2 several different structures have been used as a cladding in ARFs. Cladding designs are usually selected for loss reduction, ease of fabrication, or to control the number of guided modes. Kagome-type fibres have a more intricate arrangement of air holes and membranes than hexagram fibres and simplified negative curvature fibres as shown in Figure 2.2, however, simulations have shown that the extra cladding layers do not lead to lower leakage losses [53]. Therefore negative curvature fibres made from a single ring of stacked tubes have become of prominent interest, as they have an easier fabrication process that requires less tubes in the stack than PBG fibres. The fabrication of these hollow fibres will be discussed in more detail in the next section. The simplified ARFs also have low bending losses and benefit from the same broad bandwidth as kagome-type fibres [20; 54].

In both the kagome-type fibre and the simplified ARFs, the effect of the curvature of the membranes surrounding the core has been studied [55; 56]. In these studies a decrease in loss for an increasing curvature of the arcs that form the core boundary has been reported. However, even though this effect of the curvature has been found, very little is known about the physical reasons for this decrease in leakage loss. In Chapter 3 I will look further into the effect of the curvature of the cladding structure on the leakage loss and provide a physical explanation for the reduction. I will use the more recent simplified version of a HC fibre. In this simplified HC fibre, an air core is surrounded with either touching or non-touching circular elements [20; 45], but replace the circular elements by half elliptical elements.

Loss due to macro-bending occurs when the whole fibre is bend around an object, for example when wound around a bobbin of constant diameter. The loss depends on the bending radius of the fibre as well as on the fibre design [54; 57; 58]. For ARFs, the bending loss also depends on the core size of the fibre. Although a larger core size reduces the intrinsic loss, macro-bending losses increase for fibres with larger cores [2].

Loss due to imperfections are caused by structural inhomogeneities. Imperfection in the fibre can arise during the fabrication of the preform, as well as during the drawing process of the fibre. In the next section the fabrication process for HC fibres is discussed.

### 2.1.5 Fabrication

In this section I will describe the fabrication methods used for HC fibres. To aid the understanding of the difficulties in fabricating HC fibres, I will first describe the fabrication process of conventional solid core fibres to emphasize the differences.

All optical fibres are drawn from a macroscopic replica called a preform on the fibre drawing tower. Essentially, the glass/polymer of the preform is heated until it softening point and drawn to fibre under an imposed vertical flow. This manufacturing process, for standard all solid fibres, has matured over the years, with industrial drawing towers capable of producing several hundreds of meters of fibre per minute. The drawing of HC fibres differs in two respects. First, the process has traditionally involved an the production of an intermediary preform called a cane, and canes are subsequently drawn into fibre in a second step. Second, the presence of void regions in the fibre cross-section requires the application of pressure differences without which such regions would close under the effects of viscous forces and surface tension.

#### 2.1.5.1 Solid core fibre fabrication

To fabricate a silica step-index fibre, a preform can be fabricated using a chemical vapour deposition method. Commonly used methods are vertical axial deposition, outside vapour deposition and modified chemical vapour deposition (MCVD). The process used in MCVD is based on oxidation of chemicals in a silica tube that is rotated and heated to temperatures over 1600 degrees [59]. The chemical reagents are put in the tube using either carrier gases (for example helium or oxygen) or through dopant sources [60; 59]. When the tube is heated a fine layer of silica (or doped silica) forms on the inside of the silica tube, which is then sintered into a clear glass. The last step for the preform fabrication using MCVD is to collapse the tube to form a solid preform when the required core to cladding thickness ratio is achieved [59].

To fabricate a fibre from the produced preform, the preform is usually drawn in a drawing tower. In Figure 2.5 a schematic overview of a typical fibre drawing tower is shown. Before the drawing process starts, the preform is put in the chuck, which can then be lowered into the furnace at a controlled speed (the feeding speed). The preform is heated in the furnace to its softening point (around 1900-2000 °C for Silica). The furnaces uses a coil (also called susceptor) to heat the preform via inductive heating. The fibre is then drawn by the capstan, using the set drawing speed [61; 62]. The final dimensions of the fibre depend on the ratio between the selected feeding and drawing speed. Assuming a non-compressible material, the diameters of the preform are related through mass conservation by:

$$\frac{d_p^2}{d_f^2} = \frac{v_f}{v_p} \tag{2.10}$$

Where $d_p$ is the diameter of the preform, $d_f$ the diameter of the fibre, $v_f$ the fibre drawing speed and $v_p$ the preform feeding speed.

To keep the diameter of the fibre constant the fibre diameter is constantly monitored and the drawing speed can be adjusted to keep the dimensions of the fibre output constant for the whole length of fibre produced. After the drawing, a (commonly polymer) coating is applied to the fibre to protect it from damage and the fibre is collected around the drum.

The drawing tower described in this section can be adapted to accommodate different materials, such as soft glasses and polymers and can also be used to fabricate HC fibres.

#### 2.1.5.2 Hollow core fibre fabrication

The methods described that can be used to produce step-index fibre preforms, are not suitable for the production of a HC fibre version. For HC preform fabrication there are three commonly used methods: stacking, drilling and extrusion.

Stacking is the most commonly used method for fabricating preforms for HC fibres. Although labour-intensive and time consuming, it offers the flexibility to produce a variety of different designs. A hollow fibre is typically created using the two-stage stack and draw technique. In Figure 2.6 a schematic overview of this preforms used in this two-stage process is shown. On the left the initial preform is shown. Glass or polymer

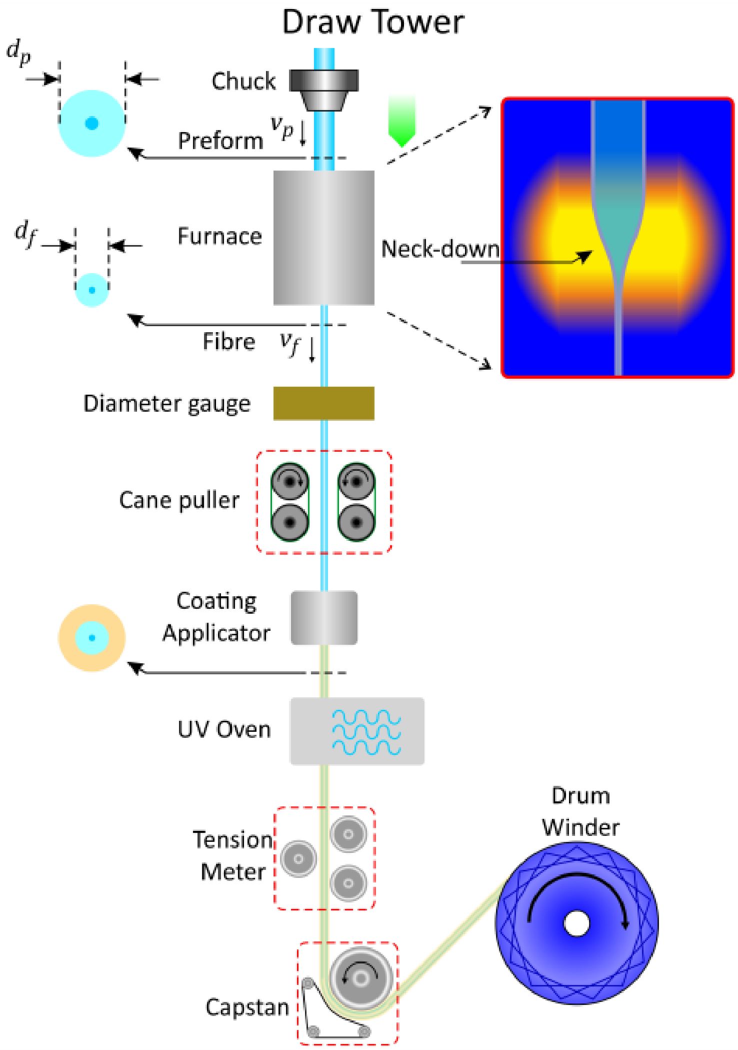

FIGURE 2.5: Schematic drawing of fibre tower. Image reprinted with permission from [63].

capillaries are stacked to the desired pattern in a size that can be drawn by the drawing tower into a cane. Typically the initially stacked preform will have a diameter in the range of centimetres, and the drawn cane will have a diameter usually below 5 mm. The cane is drawn on the drawing tower, but due to the larger dimension is not pulled around the drum. Instead the cane puller is used. The drawing speed of the cane puller is lower compared to the drawing speed of the capstan. As a result, the cane can be drawn with a diameter of a few millimetres, whereas fibres would have smaller dimensions in the order of a few 100 micrometres. To create the preform, the cane is inserted into a jacket tube, as shown in the right in Figure 2.6.

Drilling can be used when the fibre's design only needs circular air holes in the preform. An example of such a fibre is a fibre where the core of the fibre is solid but is surrounded by multiple circular air holes [64]. The holes can be drilled into silica using

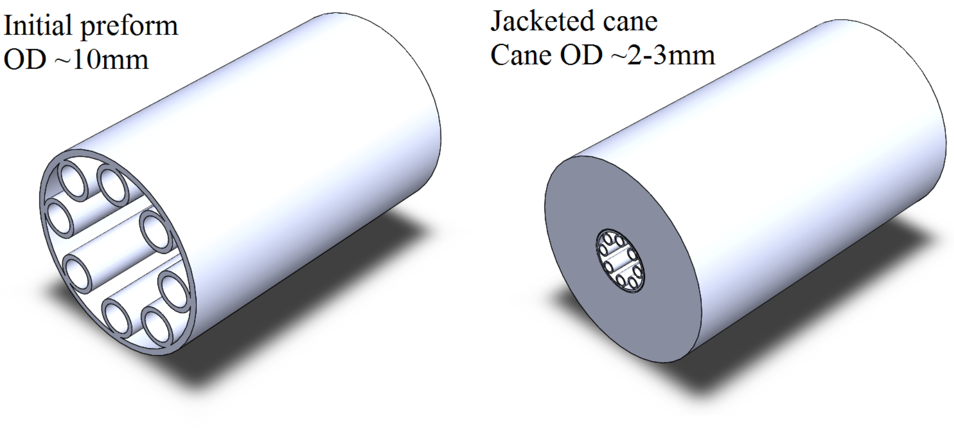

FIGURE 2.6: Schematic overview of the two-stage stack and draw technique. On the left the initial preform structure is shown, which can be used to fabricate a cane. The structure of the cane surrounded by a jacket tube is shown on the right.

an ultrasonic drill [64]. Although the drilling process can be faster, it poses limitations in how close the holes can be spaced due to the brittle nature of glasses [65]. Ultrasonic drilling however should reduce this risk compared to conventional drilling methods, and index-guiding microstructured fibres have been produced using this method in silica and tellurite among other materials [64; 65]. However, due to the structures that can be achieved using drilling, drilling is not suitable for the fabrication of ARF preforms.

For polymers and soft glasses, preforms can also be fabricated using extrusion. To extrude a preform, a die is needed. While using a die might work well on a steady-state production line, it is complex and expensive for research purpose, as the extruded preform might be different from the die, depending on the temperature the material is extruded at and the speed of the extrusion [66; 67]. This is known as the 'Die Swell', as the diameter of the extruded preform is usually larger than the diameter of the die itself [68; 67]. The die swell depends on the speed the material is extruded at and the viscosity, but also on the friction between the material and the die [68]. As a result of the die swell, it is hard to predict the exact preform that will be extruded from a die. Another complicating factor is the fabrication time and cost for each die. Dies often cannot be re-used as not all materials can be fully removed from the die. As a result a new die (or an intensive cleaning process) is needed for each extrusion, making it expensive and time-consuming to fabricate the right preform through trial-and-error [67]. This method has been used for microstructured fibre designs [69; 66], but also for ARF designs. Gattass et al used extrusion to create an sulphide-based chalcogenide preform for an ARF with eight tubes in the cladding. The fibre drawn from this preform has a loss of 11 dB/m at a wavelength of 9.5 µm [70].

Once the preform is fabricated for a HC fibre, the next step is to draw it down using the fibre tower. A preform incorporating hollow regions needs extra consideration when drawn to avoid any of the air gaps collapsing in the structure [71]. To achieve this, the air gaps of the preform are filled with a gas such as Nitrogen under pressure. The pressure applied in the preform needs to be chosen carefully, as too little will cause the structure to collapse and too much could cause the structure to expand, and burst in some cases. The pressure in the preform can also be used to expand the structure on purpose, for example when the thickness of the membranes in the structure needs to be reduced [72].

Similar to the differences between the die and the extruded preform, there are deviations between the preform design and the drawn fibre. To predict the structure in the fibre after the drawing process, fluid dynamics models can be used. The first models focussed on the simplified case of capillary drawing [73], but more recently fluid dynamics models to predict the final structure of the fibre based on the preform and the fibre drawing parameters have been used too [74; 75; 76]. However, the models currently existing are set-up for silica or other glasses. Polymer fibres, as studied in this project, do not behave exactly the same as these glasses during the drawing process due to the Non-Newtonian properties of polymers. Non-Newtonian fluids do not follow Newton's laws of viscosity. Newtonian fluids have a viscosity that does not depend on stress, whereas the viscosity of non-Newtonian materials can either increase or decrease as a result of stress. In Chapter 4 I will discuss these effects in more detail, and the existing models for capillary drawing are adapted to include this Non-Newtonian behaviour and to aid the understanding of the differences between polymer fibre drawing and glass fibre drawing.

Although stacking and extrusion have both been used successfully for the fabrication of HC ARFs, both techniques are time-consuming and labour-intensive. With the field of rapid prototyping and additive manufacturing growing over the last decades, the question that raises to mind is whether these 3D printing techniques could be used for HC fibre preform fabrication. Although several groups have made a start with 3D printing glasses, the field of 3D printing polymers is more established. To study the possibilities of 3D printing polymer fibre preforms, a literature review on polymer fibres is performed and an overview of 3D printing techniques is given in section 2.2.

### 2.1.6 Polymer hollow core fibres

Although the first HC fibres were demonstrated using silica, other materials such as soft glasses and polymers have also been explored. Plastic optical fibres (POF) are fibres where the optical material is a polymer instead of the more conventional glasses. Commonly used materials include PMMA, PS and PC, as these materials are low-cost and widely available [77]. In addition to Rayleigh scattering, light propagating in PMMA suffers from absorption due to the Carbon-hydrogen vibrations at wavelengths longer than 850 nm. To reduce this effect a heavier atom can be used instead of hydrogen. The additional weight of the atom reduces the vibrations that cause the increase in loss, which explains why fluorinated or deuterated polymers, have lower losses than for example PMMA [6; 78]. However the cost of fabricating these polymers is higher, making it a less attractive choice for POF fabrication [6].

Some benefits of using polymers instead of glasses are directly related to the material's properties. In Table 2.1 some of the material properties of PMMA, the most commonly used polymer for POF fabrication, and silica are compared. It can be seen that PMMA is much more flexible than silica as well as a lot lighter. This flexibility can be of great importance for large-core fibres, to aid an easy connection for short-range applications [78]. It can also be seen from Table 2.1 that silica is less sensitive to temperature changes than PMMA, however, it depends on the application whether this is a benefit or not. Another difference between silica and PMMA (and other polymers) is the fact that PMMA fibres are not as sharp when broken. Combined with their low cost, this makes polymer materials extremely useful for single-use fibre applications in both domestic and medical use.

For PMMA the theoretical loss is 106 dB/km at 650 nm [78]. POF have considerable advantages over silica fibres, not only their low cost, but also their ability to remain flexible with large cores as well as ease of coupling these larger fibres [77; 78]. By making HC fibres out of polymer materials, the bulk contributions to attenuation are greatly reduced, therefore paving the way for inexpensive and low-loss optical fibres with attractive properties for a wide-range of applications.

The first polymer HC fibres was reported by Argyros et al in 2006, who produced a PMMA HC preform using drilling. Their work showed that polymer HC fibres could improve transmission where bulk absorption is high, and with improvements in the fabrication method could make polymer HC fibres a suitable alternative to conventional polymer fibres [79], with the same group going on to demonstrate for example the use of

TABLE 2.1: Properties of PMMA and silica compared. Data taken from [78]

| **Property** | **Silica** | **PMMA** |
|---|---|---|
| Young's modulus | 72GPa | 3.2GPa |
| Density | $2200 kg/m^3$ | $1195 kg/m^3$ |
| Elastic limit | 1% | 10% |
| Thermal Expansion Coefficient | $5.5 * 10^{-7} K^{-1}$ | $9 * 10^{-5} K^{-1}$ |
| Glass Transition Temperature | 1500 °C | 150 °C |
| Refractive index @ 632nm | 1.46 | 1.49 |

these fibres in sensing applications when the holes of the fibre are filled with a liquid [80].

With the interest in polymer fibres growing, more research into their fabrication methods is also being conducted. Although the existing fabrication methods have led to useful fibres, these fabrication methods can be labour-intensive and time consuming. Over the last few decades, there has also been a growth in the field of rapid prototyping and 3D printing. Rapid prototyping has proven useful in the field of medicine for surgical planning and education as well as personalised braces and splints [11]. 3D printing is also being trialled for food production/decoration [81]. However, 3D printing also has applications in the field of optics and optical instruments.

In 2015, the first fibre with air holes produced with a 3D-printed preform was produced [82] as can be seen in Figure 2.7. This fibre, made of a butadiene polymer consists of a ring of holes around the solid fibre core. The preform had to be annealed before being drawn in order to reduce scattering. Pre- or post-annealing however was not needed for the fabrication of the fibre. The fibre's loss was 1.5 dB/cm at 632 nm and 0.75 dB/cm at 1064 nm [82].

This project aims to achieve 3D printed ARF preforms and waveguides. In the next section an overview of different 3D printing techniques and materials is given.

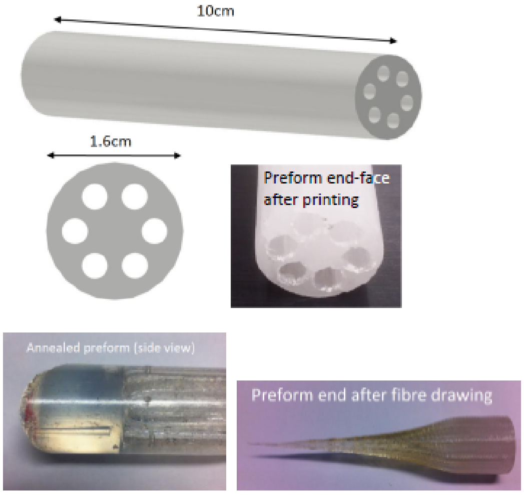

Figure 2.7: Reprinted with permission from [82], OSA. The 3D-printed preform for a solid-core microstructured fibre from Cook et al before and after annealing and the fibre structure.

## 2.2 3D printing

In this section different 3D printers are described and compared as a potential fabrication method for ARF preforms. There are many 3D printing techniques, each of which is suited to a range of applications and materials. Some 3D printers are commercially available, whilst other techniques are more suited to industrial applications. The cost of the printer can be as low as £500, but for more complex printers the cost can be over £250,000 [83] .

### 2.2.1 Stereolithography apparatus

One of the earlier 3D printing types is called a Stereolithography Apparatus (SLA) printing. A schematic overview of an SLA printer can be seen in Figure 2.8. In SLA printing, the process starts with a liquid resin that is photo curable and a platform that can be moved up and down in this resin [84]. The platform is moved up so that only a thin layer of liquid resin is on top of the platform, and a UV laser scanner is used to solidify parts of the resin. The platform is then moved down, allowing more liquid resin to move over the solidified part. Again, the parts of the object that is being made will be solidified and this step will be repeated until the object is completed [85; 86].

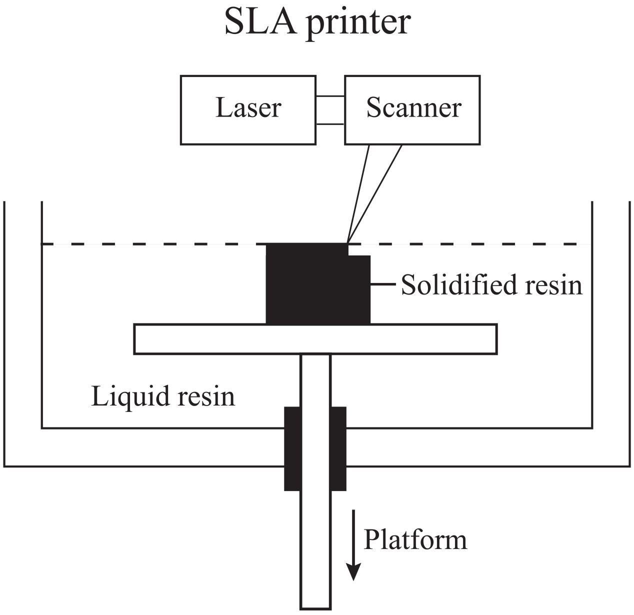

Figure 2.8: Schematic drawing of a SLA printer.

The liquid resin that isn't solidified during the printing process can be re-used, but also functions as a support system for the printed item. For example when printing an arc or ball, the liquid supports the printed layer.

### 2.2.2 Selective laser sintering

Another commonly used method is Selective Laser Sintering (SLS) printing, as shown in Figure 2.9. An SLS printer starts with a thin layer of powder of the material that will be used in the sintering process. The (high power) laser (for example a $CO_2$-laser) sinters the powder according to the 3D model, after which another thin layer of powder is pushed on top of the object using a powder roller. The stage with unused powder is moved up to enable the roller to deliver a small layer of powder on top of the printed object, to sinter the next layer, whilst the stage with the printed object is moved down. The sintering process is repeated for each layer until the 3D object is finished and can be removed from the powder. The unused powder forms a support for the printed object and can be reused [85].

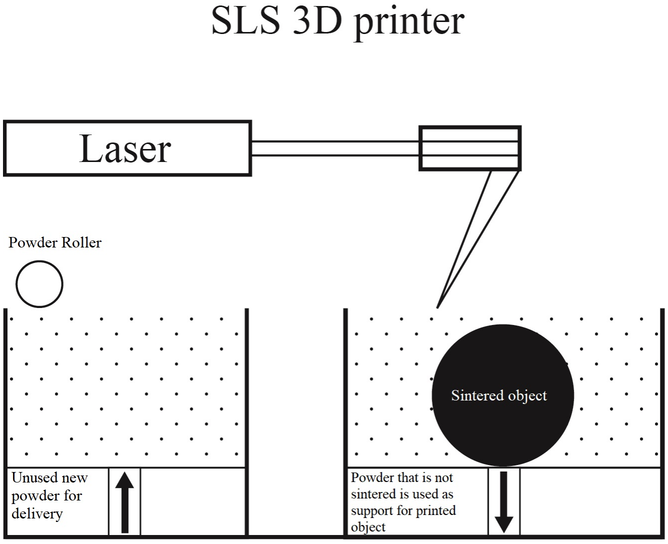

Figure 2.9: Schematic drawing of a SLS printer.

### 2.2.3 Fused deposition modelling

Commercially, the most common technique is Fused Deposition Modelling (FDM) [87]. A schematic overview of the FDM printer can be seen in Figure 2.10. An FDM printer has an extrusion head with a heated nozzle, which extrudes the filament onto the printing board. The filament is pushed into the hot-end by the two wheels it is clamped between, the speed of these wheels combined with the ratio between the filament diameter and the nozzle diameter determine the printing speed. Several configurations are possible, the nozzle can be moved at this printing speed to shape the printed part, or the object itself can be moved under the nozzle, or a combination of both [87]. FDM printers can be used to print a wide range of polymers, including nylon, acrylic (Polycarbonate (PC)), ABS, PLA and Polyethylene terephthalate (PET).There are different brands and types of FDM printers, and they can have different options in printing capabilities. Some printers may have different nozzle sizes available, or a larger printing board and/or a taller printer for larger objects. More advanced (and more expensive) printers can also use multiple nozzles to print different materials at the same time, which could be used when more complex fibre preforms are printed, for example where the cladding is coated with a different material. For our ARF printing project, only one material is needed.

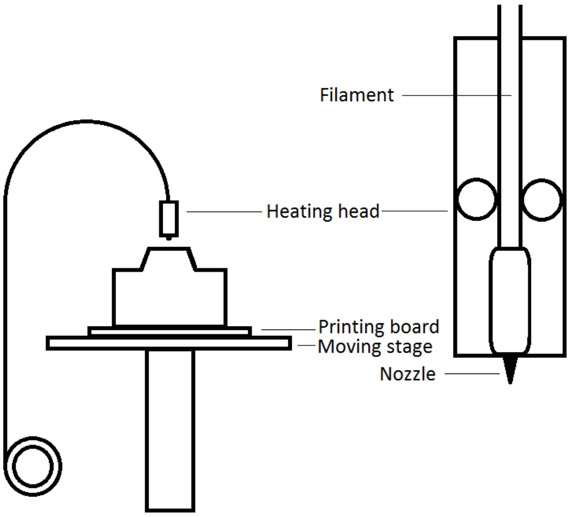

Figure 2.10: Schematic drawing of a FDM printer.

The different types of printers each have different advantages and disadvantages. One important factor to consider when comparing the different printing techniques is the materials the printer can use. Due to the photo curing process used, SLA printing is used for thermoset polymers. Thermoset polymers cannot be reheated and remoulded, and SLA is therefore not chosen for the fabrication of polymer fibre preforms. SLS and FDM printing both work with thermoplastics, polymers that can be reheated and remoulded, but SLS printers are mainly set up to work with nylon materials, whereas an FDM printer can use a wider range of materials, including nylon. To increase the range of polymers that can be used for the preform fabrication, FDM printing is selected for this project.

The printer used for this project is the UP2 Plus printer, which is shown in Figure 2.11. This printer has a minimum layer height of 150 µm and a nozzle size of 0.4 mm [88]. As a result, the extruded filament has a diameter of 0.4 mm, but when printed into layers the resolution printed depends on the layer height setting, as the layer is flattened out more when the layer height is decreased. The filament compatible with this printer needs to have an outer diameter of 1.7 mm and is set up with two temperatures to print Acrylonitrile Butadiene Styrene (ABS) (at 260 °C) and Polylactic Acid (PLA) (at 200 °C) [88]. I have purchased a separate module to be able to adjust the temperature between 160 °C and 320 °C in 5 °C increments, to enable me to print materials that require a different printing temperature[89]. More recent updates to the software from the manufacturer have made it possible to change the printing temperature without this separate module, but this was not yet an option at the start of this project in 2014.

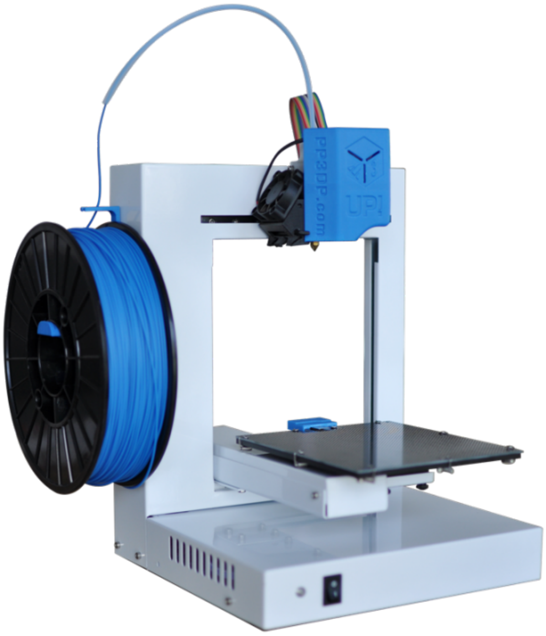

Figure 2.11: Image of commercially available UP2 Plus printer used in this project.

Like many 3D printers, the object to be printed needs to be written into a STL (stereolithography) file. Commercially available CAD programs such as Solidworks offer a straightforward route to creating and exporting three dimensional models to this particular file format. In Figure 2.12 an example of a 3D model of a preform for a nested tube fibre made in Solidworks is shown. The STL file is then uploaded into the software provided with the UP printer, UP!, and the printing settings are selected before printing. UP! does not have the same flexibility as some open source programs with regards to printing settings and options. The printing speed is between 3 and 30 $\mathrm{mm}^3$ per second, the layer height can be set between 0.15 and 0.40 mm with increments of 0.05 mm and the filling density has several pre-defined settings, including the option to print an unfilled object by just printing the outer shell [88].

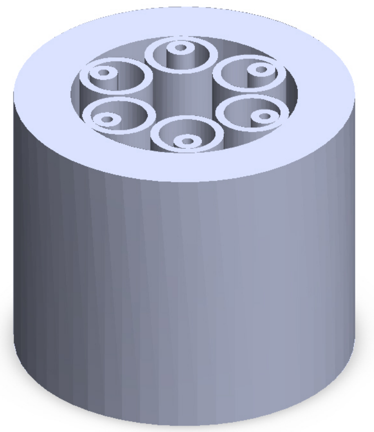

Figure 2.12: Example of 3D model made in Solidworks of a preform for a nested tube fibre.

## 2.3 Transparent polymers for 3D printing

With the printer choice identified, a suitable polymer also has to be chosen. As the aim of this project was to use the printer to fabricate preforms for subsequent fibre drawing, the polymer has to be both suitable for 3D printing and must possess suitable optical properties for waveguiding applications. For the material to be suitable for 3D printing and fibre drawing, the material must be able to be heated and remoulded repeatedly, as it will be heated during the printing process and also during the fibre drawing process. Commonly used polymers for polymer fibre optics include Polymethylmethacrylate (PMMA), Fluorinated ethylene propylene (FEP), Topas and Polycarbonate (PC) [90; 91]. In Table 2.3 these commonly used polymers for fibre fabrication are compared. ABS and PLA are also included, although they are not commonly used for polymer fibre fabrication, they are common polymers used for FDM 3D printing and as the bulk loss of the material is less important when it comes to HC fibres, they could still be used for ARF fabrication. Nylon is also considered, as it is a commercially available polymer for 3D printing that can be used to print optically clear items.

One of the properties of materials to consider when selecting a polymer for 3D printing is the behaviour of the material under stress. Young's modulus is a measure of how the material withstands changes in length when under tension or compression in the longitudinal direction. It can be seen from table 2.3 that FEP and Nylon both have a low Young's modulus, and the printed preforms from these materials may be more prone to deformation as a result.

TABLE 2.2: Overview of properties of polymers suitable for 3D printing

| | Young's modulus (GPa) | RI at 632 nm | $T_g$( °C ) | Density (g/cm$^3$) |
|---|---|---|---|---|
| ABS | 1.79-3.2 [92] | - | 90-102 [93] | 1.02-1.2 [94] |
| FEP | 0.3-0.7 [92] | 1.338 [95] | 80 [96] | 2.15 [96] |
| Nylon | 0.8-2 [92] | 1.565 [95] | 57 [97] | 1.12-1.14 [94] |
| PC | 2.2-2.5 [92] | 1.581 [98] | 150 [97] | 1.15-1.2 [94] |
| PLA | 3.4-3.6 [92] | - | 55-60 [93] | 1.23-1.25 [94] |
| PMMA | 1.5-3.5 [92] | 1.489 [98] | 155 [97] | 1.17-1.2 [94] |
| Topas | 2.6-3.2 [92] | 1.53 [99] | 136-180 [93] | 1.01-1.03 [94] |

The glass transition temperature of the polymer is also important. As mentioned in the previous section, the printer temperature can be set between 160 and 320 °C. The material starts to soften at the glass transition temperature, and a high temperature is needed for the material to be successfully extruded. Most materials in Table 2.3 have low enough softening temperatures, the only potential with a temperature higher than can be printed using the UP printer is Topas.

Although material loss contributes little to the overall attenuation in HC fibres, it is preferable that it be as low as possible. In Figure 2.13 the loss for PC and PMMA is shown for the visible regime. ABS and PLA are not plotted in this figure, as they are opaque in the visible. It can be seen that PMMA has the lowest attenuation in the visible, and would therefore be the most suited for a HC polymer fibre operating at these wavelengths. Both PC and PMMA are used in Chapter 4 for 3D printing and drawing experiments. In Table 4.2 more of their properties are shown which will be used in Chapter 4 to understand the behaviour of these materials during fibre fabrication.

Polymers are not only suitable for fibres in the visible regime, terahertz waveguides have also explored the use of polymers. As the terahertz regime suffers from high absorption, HC polymer waveguides could be an option for this regime. In the next section, materials and waveguide applications for the terahertz regime are discussed.

## 2.4 Terahertz waveguides for spectroscopy

The terahertz regime of the spectrum contains the frequencies between 0.1 THz and 10 THz, corresponding to wavelengths between 30 µm and 3 mm. This part of the spectrum is of particular interest for applications such as material characterisation and (medical) imaging. Compared to the other parts of the electromagnetic spectrum, the terahertz regime was researched less due to the lack of available sources to generate terahertz signals. However, this has changed since the invention of freely propagating broadband,

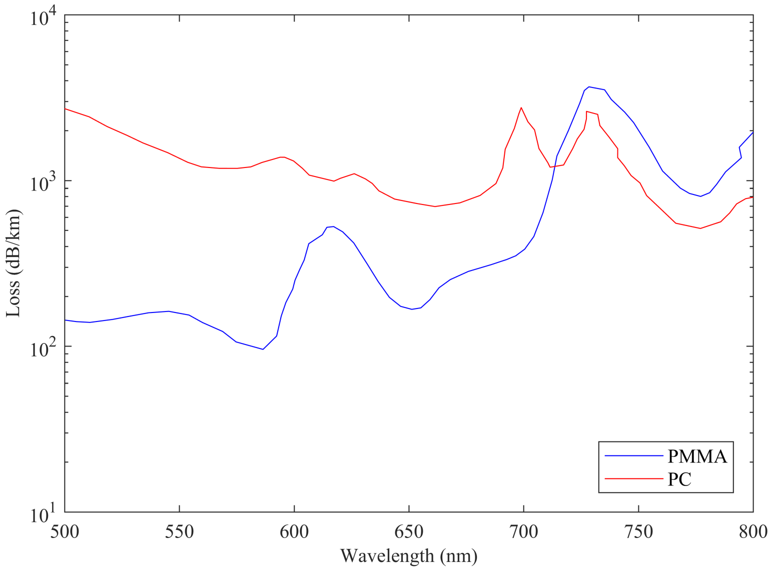

FIGURE 2.13: Attenuation of PC and PMMA in the visible regime. Data taken from [100].

single cycle terahertz pulses from photo conductive antennas [101].

One of the applications coming from the development of single cycle terahertz pulses was the Terahertz Time Domain Spectrometer (THz-TDS). The terahertz pulses were combined with pulsed lasers, which led to the THz-TDS. Due to the synchronous detection scheme the THz-TDS it has accurate measurements, and it also THz-TDS allows pulses with energy below the black-body radiation to be measured. This is possible because the thermal radiation will average to zero, which means high signal to noise ratios (SNR) can be achieved and pulses with low energy can still be detected [102]. Besides these advantages, the THz-TDS measures the transient electric fields, instead of the intensity of the signal. The transient electric field measurement can reveal the complex permittivity of the measured sample, without the need to use the Kramers-Kronig relations using the Fast Fourier Transformation (FFT) [103] [30]. Terahertz pulses can also be used to differentiate and analyse different molecular structures, as the frequency of the classical vibration of the polar molecules is in the terahertz regime [104].

As photo conductive dipole antennas were found to be a solution for terahertz signal transmission where no waveguides were needed [101], research focused on improving the transmission and reception through the dipole antennas. However, this is not suitable for all applications, for example when the source is inaccessible for the detector, such as in gas detection or endoscopies.

As an increasing number of terahertz applications are being developed, a growing need arises for reliable signal delivery systems. Data transmission systems in the terahertz range could benefit from a low-loss and flexible waveguides, which would allow for a terahertz pulse to be delivered to remote locations, but could also be used for efficient coupling between emitters and detectors. Waveguides for the terahertz regime have a range of applications, including microscopy, terahertz quantum-cascade lasers and imaging [14], but could also be useful in laboratory table-top applications to replace complicated lens systems. On top of that, hollow waveguides could also be used for sensing applications

HC fibres as described in Section 2.1 are not limited by the material's absorption, and as the signal travels in air would also not suffer from signal distortion as a solid core waveguide would. Furthermore, due to the larger wavelengths in the terahertz regime compared to the visible and infrared, the dimensions of the waveguide would be much larger. Several theoretical and experimental studies have established scaling laws between the loss of a fibre, its dimensions as well as the wavelength at which it operates. A recent study by Bird et al suggests that for single-ring antiresonant fibres such as shown in Figure 2.2e and g the loss scales as $\lambda^4/r_c^5$ [41; 105]. Commonly, the core radius of the fibres is somewhere between 10-20 times the wavelength. When considering a frequency of 0.5 THz, which corresponds to a wavelength of 0.6 mm the required core size would be 6-12 mm. As a result, HC ARF waveguides for short-range terahertz applications could be printed directly using the FDM printer described in Section 2.2.3, without the need for a drawing process.

There have already been reports of 3D printed polymer waveguides for the terahertz regime. One of these was a kagome type waveguide, printed using the Objet30 Prime printer, which is an SLA printer. The lowest loss reported through this fibre was $0.002\,\mathrm{cm}^{-1}$ (0.868 dB/m) at 0.75 THz [106]. Another waveguide was printed using the commercially available Project 3500HD plus 3D printer. This waveguide consisted of a hollow tube with an anti-reflective outer layer consisting of cones. Two different designs were tested, one with cones with a height of 600 µm and another with cones with a height of 1200 µm and are compared with a tube. It was shown that the tubes coated in an anti-reflective layer have superior transmission compared to the dielectric tube [14]. Other terahertz components than waveguides have also been fabricated using 3D printing; Jahn et al. [107] have designed and fabricated a focusing grating coupler for the terahertz regime using FDM 3D printing of a polystyrene filament. Due to the design in this component the beam was only focused in one direction creating an oval shaped focal spot. A 3D printed quasi-Wollaston-prism has also been demonstrated for THz applications via the FDM printing method where macroscopic birefringence is produced via manufacturing a grid-like structure [108]. The component allowed for two orthogonally polarised beams to be split, achieving a separation angle of 23. They same group also demonstrated a 3D printed THz q-plate [109] to generate cylindrical vector beams. These examples show that 3D printing can be used to create terahertz components, and it raises the question whether inexpensive FDM printing could be used to print antiresonant waveguides for the terahertz regime.

To decide on a material for the 3D printing of terahertz waveguides using FDM printing, the bulk loss of the polymers needs to be considered. In Figure 2.14 the attenuation of several polymers is compared. Common choices for terahertz waveguides are Cytop and Topas, which both have low losses in the terahertz regime. However, from the commercially available polymers identified for 3D printing (ABS, PLA, PC and PMMA), PC would make the most suitable candidate for HC terahertz waveguides as it has the lowest loss in this frequency range. In Chapter 5, the design, fabrication and characterisation of PC antiresonant waveguides for operation in the terahertz regime is described.

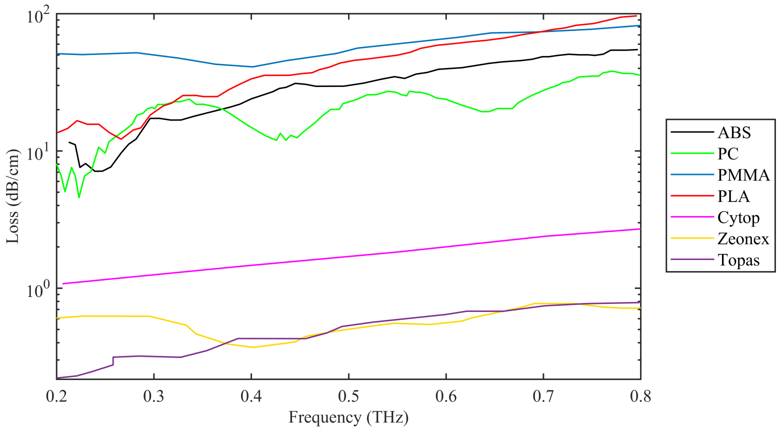

FIGURE 2.14: Attenuation of polymers used for THz waveguides in terahertz regime. ABS, PC and PLA data taken from [110], Cytop, PMMA, Topas and Zeonex taken from [90].

## 2.5 Summary and outlook

The aim of this chapter was to provide the technological background of the work described in the rest of this thesis. Different HC fibres, specifically ARFs, and the fabrication methods available to produce this type of fibre have been discussed. The different fabrication methods currently used for ARFs have successfully produced different types of HC fibres, but are time-consuming and labour intensive. As a result of this, we looked at 3D printing techniques to speed up the fabrication process. We identified FDM printing as the printing technique to try for the fabrication of HC fibre preforms. In Chapter 4 FDM printing will be used for the fabrication of HC fibre preforms. As we have also seen that the performance of an ARF fibre is directly related to the cladding design used in the fibre, it is important to identify a suitable low-loss cladding design that can be fabricated using the FDM printer. In order to find a suitable design, numerical simulations are performed in the next chapter on the attenuation through ARFs with semi-elliptical elements.

Lastly, the possibilities of printing preforms for the terahertz regime were discussed. As terahertz waveguides need a larger core than fibres for the visible and infrared, no drawing process is needed and the waveguide can be printed directly. In Chapter 5 the design, fabrication and characterisation of these waveguides is reported.

# Chapter 3

# Design of novel, 3D-printable hollow-core antiresonant fibres

In this chapter I propose a novel HC fibre design that is suitable for fabrication through additive manufacturing. To achieve the aim of 3D printing a waveguide, a suitable design for the cladding that can be printed will have to be chosen. The limitations of the different printer types and the used printer for this project are discussed in Chapter 2, and as such it is important to keep the structure relatively simple to have a design that can be produced using 3D printing. For this reason, half elliptical cladding elements are chosen. These semi-elliptical cladding elements offer two benefits compared to tubes. First, the curvature of the ellipses can be varied to aid the understanding of the not well understood effect of the negative curvature in ARFs. Second,semi-elliptical elements have two anchor points to the fibre and are therefore less likely to shift during the drawing process.

By varying the number of ellipses in the cladding design, the effect of the curvature on the leakage loss is studied. The loss contributions from leakage through different areas of the fibre design are determined in more detail to aid in understanding the optimum curvature found.

## 3.1 Numerical Modelling

Numerical modelling is usually the first step in the design of any optical device and HC fibres are no exception. Due to the often complex and expensive fabrication procedures of ARFs, numerical modelling can be used to predict crucial properties such as loss, mode-field distributions, dispersion, effective index and bend performance and/or to design fibres with desired properties. In addition to these initial predications and design indications, modelling can also be used at the end of the process to verify that the device functions as intended and to refine the design, if needed, to achieve the targeted optical properties.

To model light propagation in an optical fibre that is longitudinally invariant (i.e. the structure does not change along the longitudinal direction z), one needs to start with the Maxwell equations, which govern all macroscopic electromagnetism [111]:

$$\nabla \times \vec{E} = -\frac{\partial \vec{B}}{\partial t} \tag{3.1}$$

$$\nabla \times \vec{H} = \vec{J} + \frac{\partial \vec{D}}{\partial t} \tag{3.2}$$

$$\nabla \cdot \vec{D} = \rho \tag{3.3}$$

$$\nabla \cdot \vec{B} = 0 \tag{3.4}$$

Where $\vec{E}$ is the electric field, H the magnetic field, D the electric displacement field, B the magnetic flux density, J, the current density vector and $\rho$, the free charge density, represent the sources for the electric field. The electric displacement field and magnetic flux density are related to E and H given by the following constitutive relations:

$$\vec{D} = \epsilon_0 \vec{E} + \vec{P} \tag{3.5}$$

$$\vec{B} = \mu_0 \vec{H} + \vec{M} \tag{3.6}$$

Where P and M are the polarization field and magnetisation field, $\epsilon_0$ the vacuum permittivity and $\mu_0$ the vacuum permeability. An optical fibre is a medium without free chargers, meaning that J and $\rho$ will both equal zero. An optical fibre is also a non-magnetic medium, so $M = 0$. This means that the Maxwell equations can be rewritten to:

$$\nabla \times \vec{E} = -\mu_0 \frac{\partial \vec{H}}{\partial t} \tag{3.7}$$

$$\nabla \times \vec{H} = \epsilon_0 \frac{\partial \vec{E}}{\partial t} + \frac{\partial \vec{P}}{\partial t} \tag{3.8}$$

$$\nabla \cdot (\epsilon_0 \vec{E} + \vec{P}) = 0 \tag{3.9}$$

$$\nabla \cdot \vec{H} = 0 \tag{3.10}$$

These conditions and Maxwell's equations together can be used to find the wave equation that can be used to describe the light propagating in an optical fibre [112; 113]:

$$\nabla \times \nabla \times \vec{E} = -\frac{1}{c^2}\frac{\partial^2 \vec{E}}{\partial t^2} - \mu_0 \frac{\partial^2 \vec{P}}{\partial t^2} \tag{3.11}$$

For a mixed dielectric medium free of unbound electric charges and current sources, which is the case for most ARFs, the Maxwell equations can be manipulated assuming time-harmonic solutions to give the wave equation describing the light propagating in a fibre [114]:

$$\nabla \times \frac{1}{\mu_r} \nabla \times \vec{E} - k_0^2 \epsilon_{\mathrm{r}} \vec{E} = 0 \tag{3.12}$$

where $k_0$, the wave number ,and $\epsilon_r$, the relative permittivity, are defined as:

$$k_0 = \frac{2\pi f_0}{c} = \frac{2\pi}{\lambda} \tag{3.13}$$

$$\epsilon_r = (n - ik)^2 \tag{3.14}$$

Where $n$ is the real part of the refractive index, $k$ the imaginary part of the refractive index, $f_0$ the frequency, $\lambda$ the wavelength and $c$ the speed of light. To find a solution for Equation 3.12, one must also satisfy the boundary conditions. In the case of a fibre, there are different material media in the geometry. The number of media in the fibre depends on the type of fibre and the design, but for ARFs as described in this chapter, this is limited to two materials, air and the glass/polymer the fibre's cladding structure is made off. With no surface charges and surface currents the following boundary conditions must be satisfied [115]:

$$n \times (\vec{E_1} - \vec{E_2}) = 0 \tag{3.15}$$

$$n \times (\vec{H_1} - \vec{H_2}) = 0 \tag{3.16}$$

$$n \cdot (\vec{B_1} - \vec{B_2}) = 0 \tag{3.17}$$

$$n \cdot (\vec{D_1} - \vec{D_2}) = 0 \tag{3.18}$$

From Equation 3.15 and 3.16, it can be concluded that on these boundaries the tangential components of the electric and magnetic field must be continuous [115]. As the normal components of the magnetic flux density and the electric flux density must also be continuous (as shown in Equation 3.17 and 3.18), the normal component of the magnetic field is also continuous for non-magnetic media. However, the normal component of the electric field is not continuous on the boundary between two media [115].

Because of the complexity of the refractive index distribution in ARFs, analytical solutions for Equations 3.12, 3.15, 3.16, 3.17 and 3.18 are almost always impossible to obtain. It is however known that the field will be time-harmonic and because the waveguides studied in this case are longitudinally invariant, the field will assume the form shown in Equation 3.19 as described by Bloch's theorem [116].

$$\vec{E} = A(x, y) \times e^{i\beta z} \tag{3.19}$$

where A is the transverse amplitude, and $\beta$ the propagation constant along the z-axis, defined as $\beta = n_{eff} + ik_z$. The propagation constant is made up of a real part, but can also have an imaginary part when there is gain or loss in the system. Using the boundary conditions, the wave equation can be considered as an eigenvalue problem. Its eigenvectors are the mode field distributions, where from its eigenvalues one can obtain $\beta$. Subsequently, the loss for a modelled fibre can thus be determined from the imaginary component of the propagation constant [117; 118]. In the next section a numerical method for solving the equation when no analytical solution can be found is described.

## 3.2 Finite Element Method

The complexity of the permittivity profile of microstructured fibres and ARFs in particular often dictates the use of numerical methods to solve for propagating modes within these fibres. Many such methods have been developed and perfected over the years, with several companies now offering various commercial softwares relying on different algorithms to find the desired solutions. For my project, I selected the Finite Element Method (FEM) [117; 114]. The FEM was first used in 1956 in the mechanical industry [119]. To analyse an elastic two dimensional domain, the studied surface was represented using triangles with a linear displacement across the surface [120]. Each triangle's behaviour could be described using an elementary stiffness matrix, which is used to describe a complex system numerically. The finite element method has found more and more applications from this point onwards, as it can numerically solve very efficiently systems of partial differential equations (PDE), which is the most general way in which all physical problems can be mathematically described. The first use of the FEM to solve electromagnetic problems was in 1968 by S. Ahmed, to analyse the modes in a metallic waveguide [121; 122; 123]. For my project, the FEM was my preferred method for calculating the model properties of HC fibres as it is fully vectorial, it allows one to take the material dispersion into account, and it allows partial calculations for symmetrical problems [124; 125], reducing the calculation time needed.

Maxwell's equations as shown in equation 3.12 with boundary conditions as shown in Equation 3.15 -3.18 are an example of a PDE with known boundary values. FEM solvers manipulate these equations into a generalised eigenvalue problem, where $\beta$ is the eigenvalue and the fields are the eigenvectors. The domain is then meshed into a grid and the solution is found accurately on each grid point by solving for the eigenvalues. In Figure 3.1 a model for a SI fibre is shown. The mesh used to solve for the fundamental mode (FM) in the structure is shown and the solution found for the fundamental mode is shown.

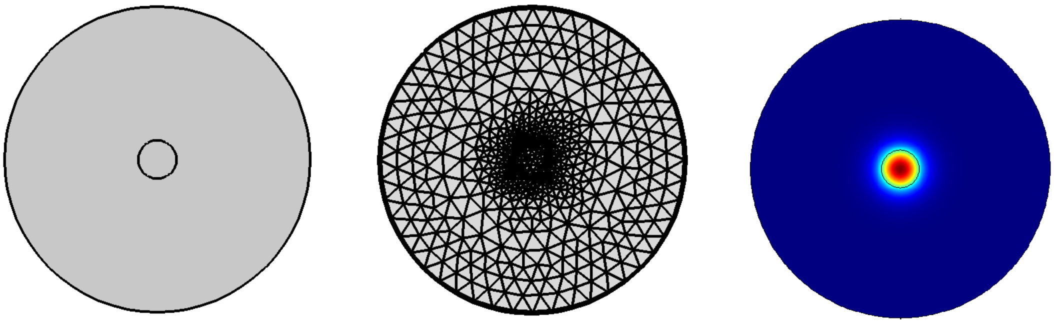

Model of SI fibre. Mesh used in SI fibre. FM found in SI fibre.

Figure 3.1: Three stages of numerical modelling of fibres

To create a mesh for the studied domain, the structure is divided into a grid. The grid contains elements that can vary in size and shape. For 2D problems, triangles or quadrilaterals are commonly used [117]. Triangles are often the preferred shape to use for circular structures as they can mimic circular shapes better, and are thus often used when studying fibre optics with the FEM. This grid in the model is commonly referred to as the mesh. Apart from the shape, the dimensions of the elements in the mesh, the mesh size, are important in determining the accuracy of the solutions. For each grid point a set of linear equations is solved which leads to the results for the initial problem. The accuracy of these results will depend on the mesh size used [114]. In general, smaller mesh sizes yield more accurate solutions. However, as for every partition of the structure a solution has to be found, reducing the mesh size increases the calculation time drastically. It is therefore important to choose the mesh size as large as possible so that it still accurately represents the geometry and manages to show all local effects. One way to focus on the local effects is to use a smaller mesh size in the areas of interest and a coarser mesh in areas less relevant. For example, in a step-index fibre, the mesh in the core can be made smaller to focus on the modes in the core, as shown in Figure 3.1. To make sure the mesh size used is giving accurate solutions, convergence studies on well known cases where semi-analytical solutions are known can be run, for example in the case of a circular hole in a dielectric [2].

To mimic the fact that the medium surrounding real fibres extends indefinitely, numerical models employ absorbing layers known as perfectly match layers (PML) to surround the fibre geometry to be studied. The PML is an artificial layer that avoids reflections and scattering, and absorbs any field incident on it [126; 127]. The PML is of crucial importance to be included in the model when calculating the leakage loss in the fibre, as without the PML light would reflect back into the fibre instead of leaking away, which would lead to an incorrect calculated leakage loss for the structure.

Out of the various commercial FEM packages available, for this project COMSOL Multiphysics is chosen [118]. COMSOL has a wide array of applications, and also benefits from add-on modules that can be used for the simulation of different processes such as heat transfer, acoustics and fluid flow. To model fibre optics and waveguide the 'wave optics' module can be utilised. COMSOL can be used using the graphical user interface (GUI), but also can be used through Livelink. Livelink enables the user to script programs for pre- and post-processing on top of the functions COMSOL Multiphysics offers to solve complex problems. The code used for the work reported in this chapter is based on the work by my colleague M.S. Abokhamis and uses COMSOL Livelink to communicate to a Matlab script [128].

In order to illustrate the effect of the mesh size on the calculation time and accuracy of the results, a mode analysis is performed on a step-index single mode fibre. The fibre modelled has a core radius of 5 µm, cladding radius of 30 µm and a refractive index of 1.4508 and 1.45 in the core and cladding respectively. For simplicity equal mesh density is used in this example. The number of elements in the model that needs to be solved for is therefore directly related to the chosen mesh size. In Figure 3.2, the element size is plotted against the calculation time for the mode analysis of one mode at a wavelength of 632 nm. As expected, as the element size decreases (and thus the number of elements increases) the calculation time increases. It should be noted that the exact calculation time for this specific problem will be different when different computers are used, as it depends on the memory and processing speed available. In this case, the processor used was the Intel Xeon E5-2637 at 3.5 GHz with a memory of 256GB. As these tests are all done with the same computer, it is a reliable way of showing the relation between the element size and computation time.

The choice of mesh size is a balance between accuracy and computation time. To look at the impact of the mesh size on the accuracy of the results, the convergence of the calculated effective refractive index is plotted using the relative error in Figure

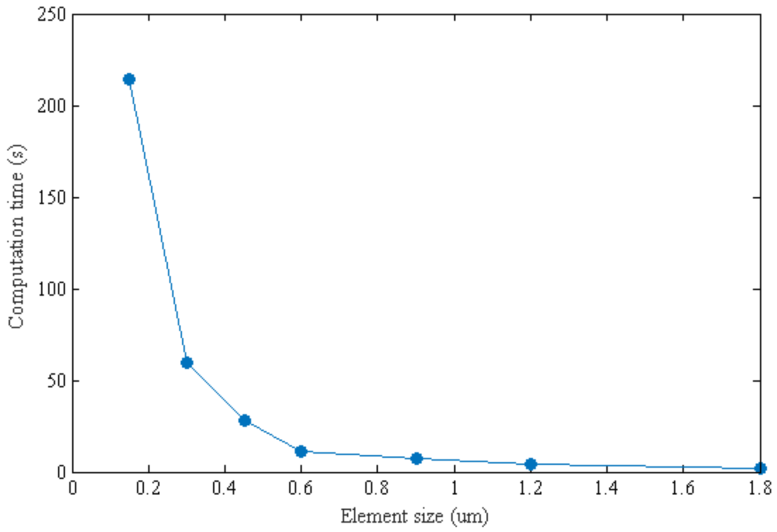

FIGURE 3.2: Calculation time dependence on element size for studied step-index fibre with a core radius of 5 µm, cladding radius of 30 µm and a refractive index of 1.4508 and 1.45 in the core and cladding respectively.

3.3. The relative error for this comparison is defined as the absolute error between the smallest mesh tested divided by the calculated effective refractive index for the smallest mesh tested. It can be seen that the solution converges quickly, and that it is therefore acceptable to slightly increase the mesh size in order to drastically reduce the computation time when multiple wavelengths and modes are studied.

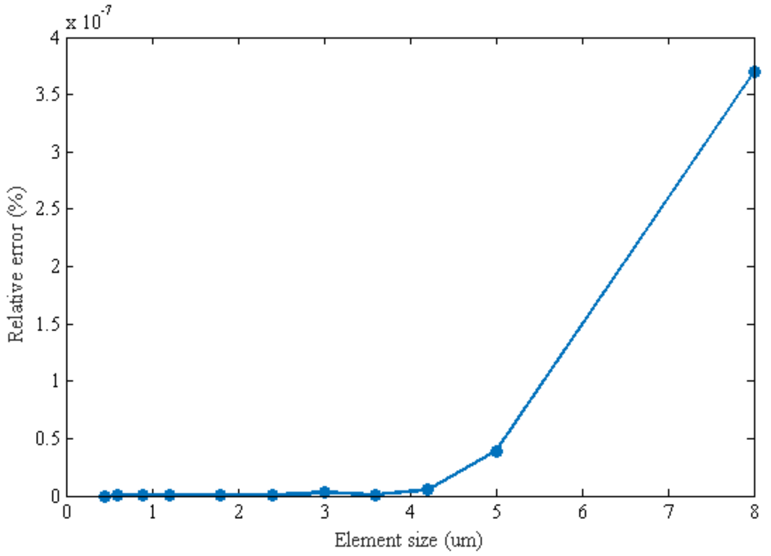

FIGURE 3.3: Convergence plot for relative error in the effective refractive index calculated for studied step-index fibre. The relative error is calculated compared to the smallest element size studied.

To reduce computation time, different mesh sizes can be used along the structure, with the finest mesh in the area of interest. For example in a step-index fibre a fine mesh is needed in the core to find the modes supported in the core. The same step-index fibre as used in the previous example is studied again with a coarser mesh in the cladding area. The number of elements can be decreased in this way to 14336 instead of 98402 for a uniform mesh and the computation time is reduced by 84%, whilst the difference between the results is less than $6\mathrm{e}^{-9}$ %. This shows that adjusting the mesh size to fit the problem modelled can drastically reduce the computation time required for parametric sweeps.

In a HC fibre, the geometry of the cladding area is different from the cladding area in a step-index fibre. The thin cladding membranes in an ARF are usually thinner than the wavelength used, and therefore sometimes thinner than the mesh-size that could be used to accurately describe a step-index fibre. In order to achieve an accurate solution of the wave equation in the thin cladding membranes, the mesh-size needs to be reduced in these areas to ensure that the cladding membranes are clearly defined in the mesh by using at least five layers of mesh elements in the cladding membrane.

Choosing the right mesh size is one way of optimising calculation time, but depending on the geometry's symmetry the studied domain can also potentially be reduced [125]. In the case of circular fibres as well as in the case of relevance in this project of fibres with a six-fold azimuthal symmetry, often only a part of the domain needs to be studied to solve for the behaviour across the whole domain. The plane of symmetry in the structure is replaced with a suitable combination of boundary conditions, to effectively cut the domain and reduce the calculation time without affecting the results of the simulation [125].

## 3.3 Fibre design with half elliptical elements

Now that I have covered the numerical tools employed in my thesis for fibre design modelling, I will describe theoretical and numerical work performed on the design of novel, 3D-printable antiresonant structures. It is well established that in ARFs with a kagome-type cladding, increasing the inwards curvature of the core boundary results in a dramatic reduction of the leakage loss of the fibre [42; 43; 55]. However, at the time I performed this work, the reason why this was the case was far from clear. More recently, there has also been research into the effect of semi-circular nested elements [129] in ARFs. In this design, the curvature was changed in the nested element rather than a change in curvature in the cladding element forming the core boundary. In this case, the curvature did not seem to affect the leakage loss. However, the position of the nested element had an impact on the loss [129]. In this section a systematic study into the effect of the curvature is described and analysed, in order to design an ARF with a lower leakage loss compared to ARFs with different cladding structures to understand what causes the reduction of leakage loss of the fibre.

Half elliptical cladding elements offer the flexibility of a systematic and gradual change in curvature, as well as for changes in the major semi-axes of the elements without changing the separation between them. Together with researchers from Pennsylvania State University, I studied the loss of a fibre with full elliptical cladding elements and it has been shown that there are curvatures where the leakage loss is lower compared to a fibre where circular cladding elements are used [130]. In practice, due to the effect of surface tension which tends to promote circular shapes, the use of fully elliptical capillaries could pose a problem of shape retention during the fibre drawing [74]. To reduce the likelihood of deformations during the fabrication process, half ellipses are used for the cladding elements instead of full ellipses. This design benefits from the same flexibility in allowing changes to the curvature, but is more likely to retain its shape under high tension and high viscosity fibre draws due to having two anchor points with the outer ring of the cladding. As a result of this, the half ellipses are also less likely to tilt during fabrication compared to full ellipses. Half ellipses also have the advantage of taking up less space in the fibre, and thus allow a larger core size compared to a same-sized fibre with full ellipses, in cases where the fibre's outer diameter is restricted. The larger core size will lead to lower losses, as the loss in this type of fibre scales with approximately $\lambda^4/r^5$ [41; 105].

### 3.3.1 Parameters studied

The novel design I propose is shown in Figure 3.4. Key design parameters include the core size, the major and minor semi-axes of the elliptical elements, the thickness of the membranes and the gap $d$ along the inner cladding boundary between adjacent elements. The curvature of the elliptical elements is defined as

$$c = \frac{l}{w} \tag{3.20}$$

where $l$ is the major-axis and $w$ the minor-axis of the ellipse. In order to study the effect of change in curvature on the leakage loss of the fibre, it is important to keep as many other parameters in the structure constant throughout the simulation as possible. To isolate the effect of the curvature as much as possible, the core radius of the fibre is fixed, as well as the fibre size (and thus the ellipse's major axis). To keep a constant separation between the ellipses, the number of ellipses is varied between 4 and 14 in order to vary the curvature. To avoid potential issues with changes in symmetry and to enable the use of quarter structures to reduce the calculation time, only even numbers of cladding elements are used. In Figure 3.4 the parameters of the structure are shown.

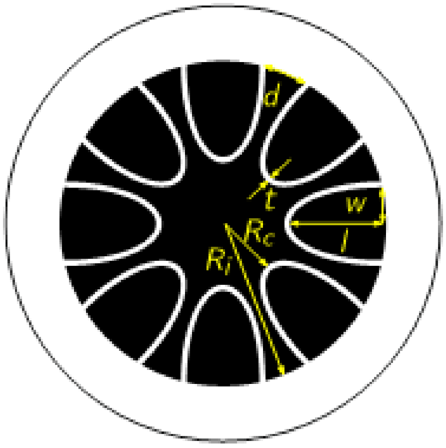

FIGURE 3.4: Geometrical parameters of the fibre under study, here with 8 half elliptical strands. The core radius is $R_c$, the major semi-axis $l$, the minor semi-axis $w$, wall thickness $t$, cladding radius $R_i$ and separation $d$.

To compare the effect of the elliptical elements to circular cladding elements, the case where the curvature equals 1 is included in this study. Using a core radius of 12.5 µm, a fibre radius of 24.84 µm and a separation of 5.3 µm, an ellipse length of 11.39 µm is needed to have semi-circular elements when there are 6 elements in the structure. The structures studied are shown in Figure 3.5. Material dispersion and absorption loss are not included in the simulations to distinguish the effect of the curved elements compared to other loss factors.

### 3.3.2 Results

Using FEM, the leakage loss for the fundamental mode in the structures in Figure 3.5 is simulated. In Figure 3.6 the leakage loss for each structure is plotted against the normalised frequency, f, defined as

$$f = \frac{2t}{\lambda}\sqrt{n_2^2 - n_1^2} \tag{3.21}$$

where $t$ is the cladding element thickness, $n_2$ the refractive index of the cladding and $n_1$ the refractive index of the core, which in the case of an ARF consists of air, so $n_1 = 1$.

In Figure 3.6, it can be seen that the lowest loss is found for the structure with 10 ellipses, which corresponds to a curvature of 2.29. It can also be seen that, even though the fibres have the same core and fibre diameter, the loss can be reduced by 2 orders of

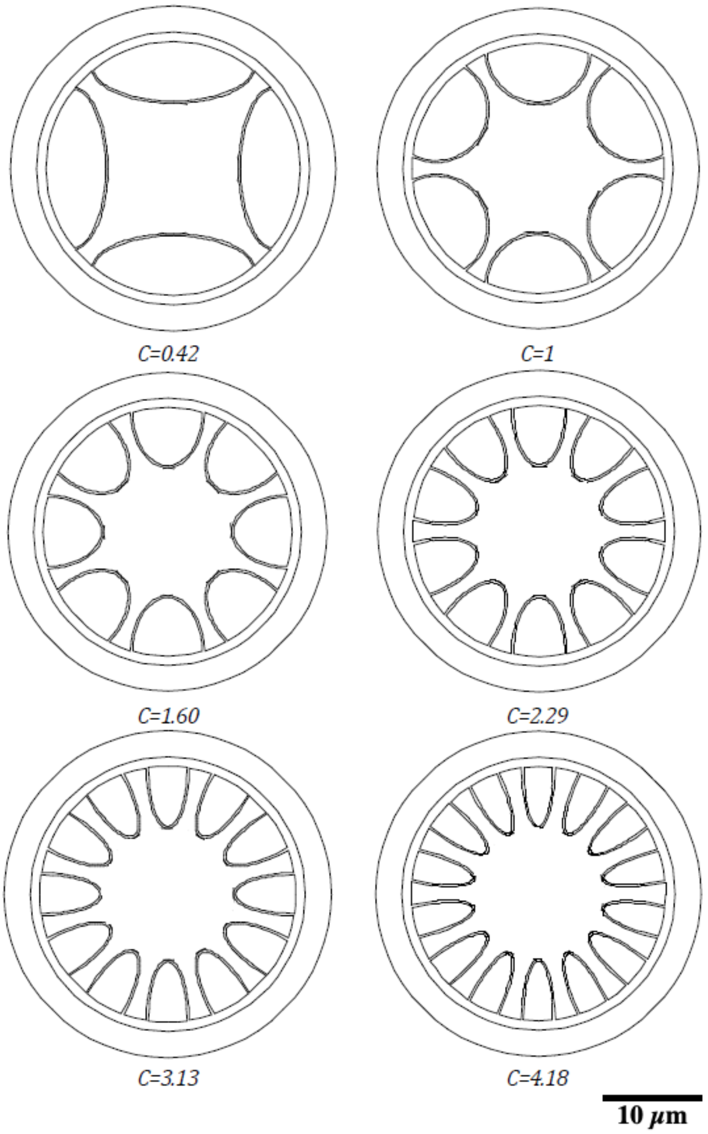

Figure 3.5: Simulated structures with 4, 6, 8, 10, 12 and 14 cladding elements with a corresponding curvature of 0.42, 1, 1.6, 2.29, 3.13 and 4.18 respectively.

magnitude by increasing the curvature of the elliptical elements.

Apart from a change in the leakage loss, there is also a change in the antiresonance window for the different structures. The width of this window decreases for an increasing number of elements. The decrease in the antiresonance window width is likely due to the increasing blue shift at the low frequency edge as a result of the increasing curvature. A similar effect was seen in fibres with circular cladding elements as the refractive index of the cladding elements was increased. This effect was attributed to the changes in the cut-off frequency of the modes guided within the thin membranes [131]. The fraction of

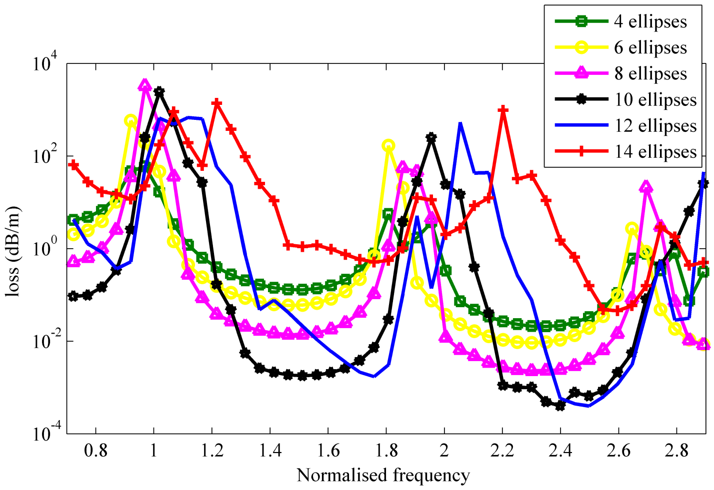

FIGURE 3.6: Calculated leakage loss for structures shown in Figure 3.5 with a core size of 12.5 µm and inner radius of 24.84 µm plotted against the normalised frequency.

power in the cladding is defined as:

$$R = \frac{P_{cladding}}{P_{cladding} + P_{core}} \tag{3.22}$$

The change of the window width due to the blue shift is more apparent in Figure 3.7, where the fraction of power in the cladding is plotted. It can also be seen in this figure that the absolute minimum of the fraction of power in the cladding is similar for all the structures, which indicates that the curvature can not be used to increase transmission where the glass is opaque, as the fraction of power in the cladding is unaffected by the changes in the curvature of the cladding elements. [132]

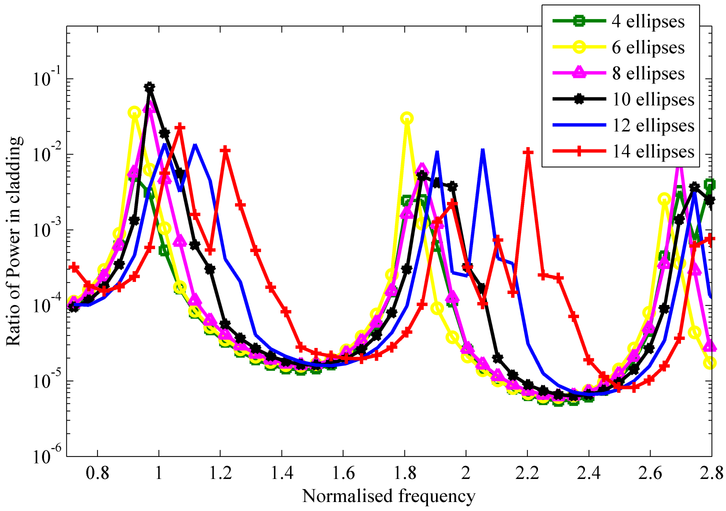

FIGURE 3.7: Calculated fraction of power in cladding for structures shown in Figure 3.5.

To verify that the reduction in loss in the different fibre designs with half elliptical elements is not due to the number of elements, the simulations have been repeated with different parameters. Using three different core radius and inner radius combinations, the leakage loss is simulated for six designs with 4, 6, 8, 10, 12 and 14 elements in the cladding of the fibre structure. In the previous case, the minimum for the leakage loss was found at 10 elements, which corresponds to a curvature of 2.29. The loss calculated for all six designs for the three different core and inner radii are shown in Figure 3.8, 3.9 and 3.10. In Table 3.1 an overview of the optimum curvature for each design are given. It can be seen that for all three parameter cases an optimum curvature is found, independent of the number of ellipses. It can also be seen that there is a similar change in the widths of the antiresonant windows. These results suggests that there exists an optimum curvature for an antiresonant fibre with half elliptical strands unrelated to the number of ellipses but connected to the curvature of the cladding elements. The simulations were repeated with different sets of varying parameters. For all the parameter sets explored, the optimum range for the curvature of the cladding elements was found to be in the range 2-2.5. This is the first key result of this study, as it points towards ways to reduce leakage loss in this type of fibre.

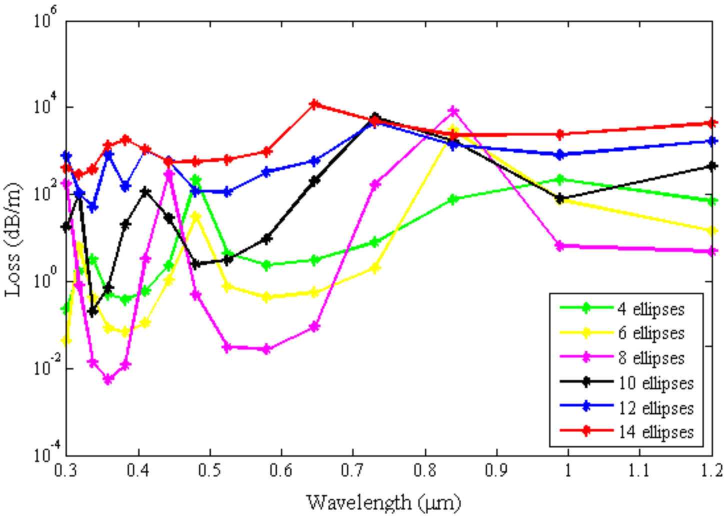

FIGURE 3.8: Leakage loss for all six fibre designs with a core radius of 10 µm and inner radius of 19 µm.

TABLE 3.1: Overview of optimum curvature and number of elements for fibre designs with different parameters for core and inner radius.

| **Core radius &** | **Inner radius &** | **Optimum number of elements** | **Corresponding curvature** |
|---|---|---|---|
| 10 µm | 19 µm | 8 | 2.13 |
| 13 µm | 23 µm | 10 | 2.36 |
| 15 µm | 24 µm | 12 | 2.13 |

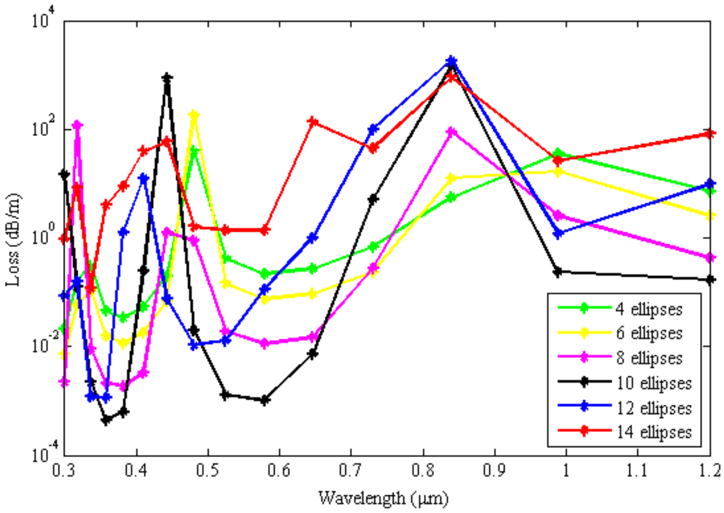

FIGURE 3.9: Leakage loss for all six fibre designs with a core radius of 13 µm and inner radius of 23 µm.

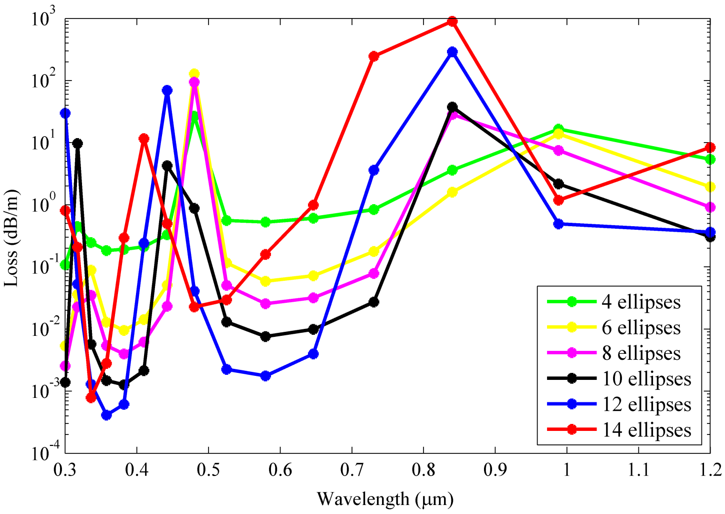

FIGURE 3.10: Leakage loss for all six fibre designs with a core radius of 15 µm and inner radius of 24 µm.

I also studied the effect of the curvature on higher order modes. In Figure 3.11, the ratio of the leakage loss between the first higher order mode (LP11) and the fundamental mode (LP01) is plotted. To avoid having to switch between boundary conditions to calculate all the modes in the fibre, the whole structure is studied instead of using symmetry to only simulate a quarter of the structure. For these calculations I used the initial fibre parameters. It can be seen that this ratio decreases and is at its lowest for the highest curvatures. This is due to the phase-matching conditions for the higher order modes. For the higher order modes the guided mode can be phase-matched with a mode in the air-gap of the elliptical elements. As the curvature increases, the area of the air-gap decreases which has a negative effect on the phase-matching conditions. For a higher curvature, the loss of the higher order mode is therefore lower.

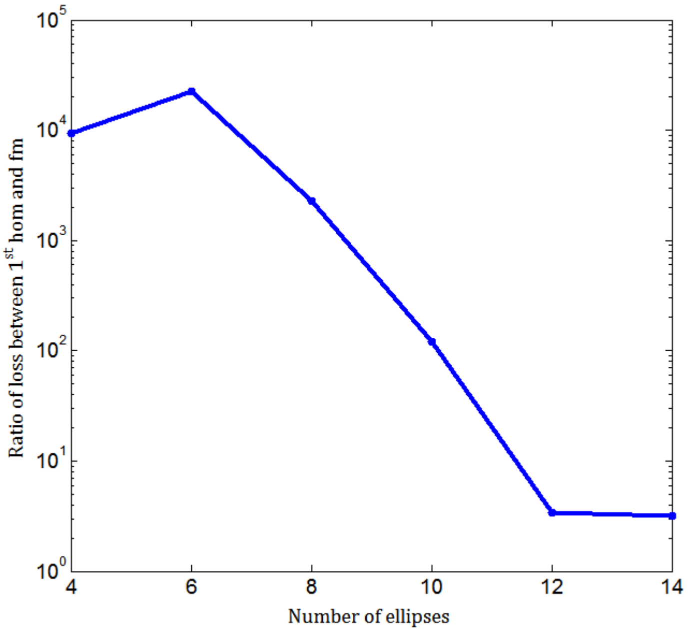

Figure 3.11: Ratio between the loss for the first higher order mode (HOM) and the fundamental mode (FM) for the 6 different fibres shown in Figure 3.5.

## 3.4 Understanding of the effect of curvature on leakage loss

To investigate whether the decrease in leakage loss is caused by the curvature alone, I simulated the same structures with solid ellipses instead of air-filled cladding elements. As can be seen in Figure 3.12, differently from the case with thin membranes and hollow cladding structures, the leakage loss for solid elements does not decrease with an increasing curvature. This indicates that the curvature alone cannot explain the reduction in loss and the reduction in leakage loss is caused by the combination of antiresonance and the curvature.

Looking at the field distribution of the fundamental mode in the six different structures that I studied shown in Figure 3.13, it can be seen that the amount of power that penetrates through the elliptical elements decreases as the curvature of the cladding elements increases. At a high curvature the field decay through the elliptical elements is lower than the leakage at lower curvatures. However, one can notice that there is also more power confined within the membranes forming the cladding elements, which leaks out to the jacket. This is the cause of the increase in loss when the curvature is increased

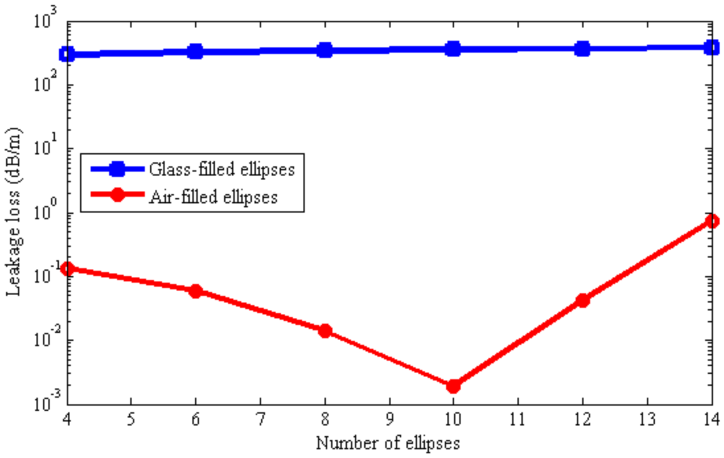

FIGURE 3.12: Loss comparison for structures with solid ellipses and air-filled ellipses using the designs from Figure 3.5 as a function of the number of ellipses. All simulations at the normalised frequency, f, 1.42.

above the optimum curvature.

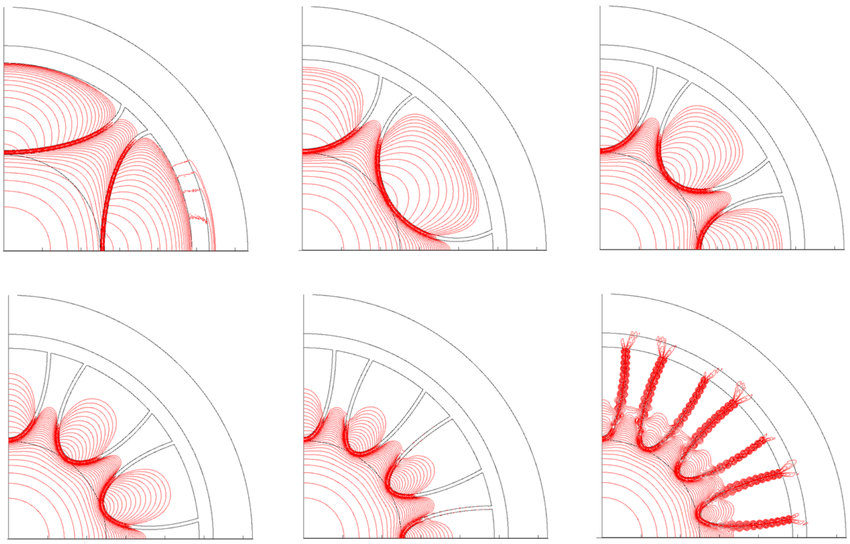

FIGURE 3.13: Mode profile for the FM for the six structures simulated from Figure 3.5

To confirm these findings, I have calculated the integral of the radial Poynting vector along the inner boundary of the fibre. This can be divided in contributions to the leakage loss through:

- the elliptical elements
- the separation between the elements
- the glass of the membranes

In Figure 3.14, these contributions normalised to the total of the integral of the radial Poynting vector along the inner boundary are shown. For 4, 6, 8 and 10 ellipses, it can be seen that the leakage through the elliptical elements dominates the leakage loss. After this point however, the leakage through the glass of the membranes starts becoming dominant. This can be understood from the path of the light rays in the fibre. The light rays from the guided core mode strike the membranes at a lower angle than compared to the lower curvature cases, where they impinge at almost 90°. When the curvature is sufficiently high, this results in total internal reflection of the ray within the membrane. Another way to see this is by thinking that the core-guided mode becomes phase-matched with a mode in the glass membranes, which then leads to an increase in leakage loss.

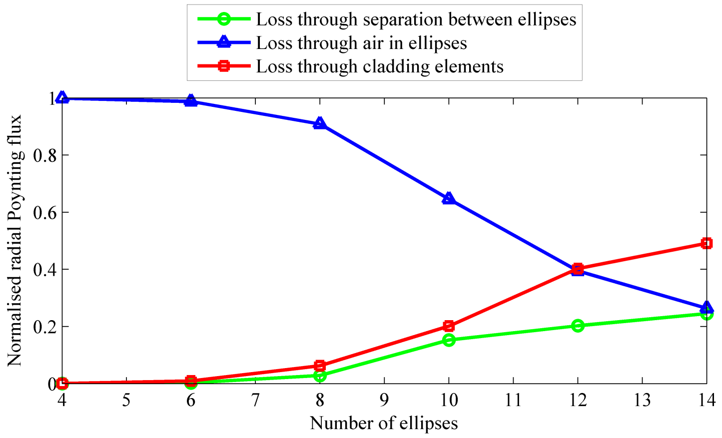

FIGURE 3.14: Calculated ratios of the contribution to the leakage loss for the different boundary areas on the fibre using the structures from Figure 3.5.

## 3.5 Conclusions

In this chapter a novel design for an ARF was studied that can be fabricated using 3D printing. The cladding design in this fibre consists of half-elliptical elements. To optimise the performance of this fibre, the influence of the curvature of the cladding membranes is studied. One of the main original conclusions was that when using half elliptical elements, the loss of the fibre can be reduced significantly by using the optimum curvature, which identifies designs where the leakage through the airclad elements matches the leakage through the glass membranes. For curvatures below the optimum curvature, there is too much leakage of the field through the elliptical elements. For curvatures above the optimum curvature, total internal reflection occurs in the cladding membranes and causes an increase in the leakage loss.

A similar reduction in loss is seen when full ellipses are used instead of half ellipses [130]. However these full ellipses take up more space in the fibre compared to half elliptical elements and could pose a tougher challenge in the fabrication due to the potential of rotation/tilt during the drawing process, caused by the pressure of only one anchor point between the cladding element and the jacket tube, instead of two as in my proposed design.

The optimum curvature depends on the core size, overall fibre size and separation between the elements in the fibre. For the design studied in this chapter, the optimum curvature was found at 2.29, but when considering the different sets of parameters studied there seems to be an optimum curvature range in the region of 2-2.5.

As mentioned before, the design with semi-elliptical elements has been optimised with the aim of it to be fabricated using 3D printing. In the next chapter, progress towards printing polymer fibre preforms using an FDM printer are reported. But preform fabrication is not the only application of this design. One of the other possible applications of this design, in addition to that of light delivery in the visible/near infrared is that the elliptical cladding design can be used for a large diameter waveguide for terahertz transmission. Due to the approximately 100 times longer wavelength in the terahertz regime compared to the near infrared, a terahertz waveguide requires an equally bigger (i.e. 100 times larger) core size compared to HC fibres for the near infrared [133]. As a result, this waveguide design could be fabricated via 3D printing directly without the need for a drawing process due to the larger dimensions of the waveguide, which will be shown and discussed in Chapter 5.

# Chapter 4

# Polymer fibre fabrication

## 4.1 Introduction

In this chapter I report the progress made towards 3D-printing polymer antiresonant fibre preforms and subsequently drawing them into fibre. As discussed in Chapter 2, the printer available for this project was a conventional, low-cost FPM printer, the UP2! plus printer. The first step in the fabrication process is the 3D printing of the preform. From the material options discussed in Chapter 2, four materials were successfully used for 3D printing ARF preforms: ABS, PLA, PC and PMMA. Initial drawing tests on these printed preforms were performed and brought to light the practical constraints and limitations imposed by the quality of the 3D printed preforms as well as the effects of intrinsic material properties of the polymers used for fabrication. Preforms printed from our FDM system showed lower density than the material used for printing, indicating the presence of bubbles introduced in the printing process. Furthermore, the fibre draws revealed non-Newtonian behaviour of the polymer materials, implying that the expertise in drawing glass fibres could not simply be transferred across.

To aid our understanding of the implications of the non-Newtonian shear-thinning behaviour of polymers, I developed and experimentally validated a numerical model for polymer capillary draw taking into account these effects. This model and experiments revealed that PC behaves more like glass whilst PMMA showed more prominent shear-thinning.

To address the issues found during the initial fibre drawing experiments, I investigated a simpler fibre design, a 'wagon wheel' fibre which requires only one pressure region during fibre draw and thus a simpler fabrication process as compared to the ARF designs of Chapter 3. In an attempt to reduce the bubbles present in the printed preforms, I

carefully investigated the annealing of printed tubes.
I conclude from the work presented in this Chapter that the quality of the preforms printed on the FDM device available for this project must be improved in order to facilitate their drawing into fibre. I show in the next Chapter however, that hollow waveguides printed directly from this printer can operate successfully in the Terahertz region.

## 4.2 3D Printing polymer fibre preforms

A crucial first step in 3D printing preforms is the development of the corresponding model using computer-aided design (CAD) tools and thorough understanding of the printer settings. The tool used for this work was the commercially available software SolidWorks. I successfully printed four different materials: ABS, PLA, PMMA and PC. A summary of the datasheets for these four polymers is given in Appendix B. ABS and PLA have both been used, as they are standard 3D printing materials and the UP printer has specific settings to print these materials. For commercial printers ABS and PLA are both suitable due to their low cost and strength. As ABS and PLA both have been printed before, the printing temperature required to print them are well known, the UP Printer has pre-defined settings for these materials, PLA is printed at 200 °C and ABS is printed at 260 °C [134]. For the other two materials that have been printed, PC and PMMA, I performed a study to optimise the printing speed and temperature. The PC filament used is commercially available, but the PMMA filament for the optimization has been drawn by my colleague Dr. W. Belardi from a PMMA rod into a 1.7 millimetre thick filament, with an approximate length of 15 metres.

The first parameter to optimise is the printing temperature for each material. For each material, I extrude a 30 cm sample at a range of different temperatures with increments of 5 °C. The range tested for each material is based on the reported softening/printing temperatures from the literature as shown in Table 4.1. I include PLA and ABS in these tests to observe what happens above and below the optimum printing temperatures, as the optimum printing temperature with the UP printer is known. The optimal temperature is chosen by comparing the extruded filament samples. It is important that the extruded filament has an equal thickness along the filament, as variations will lead to imperfections in the printed object. It is also important to pay attention to the appearance of the filament before and after extrusion. A change in colour or transparency can show that the filament has burned or crystallised. Burnt or crystallised areas would lead to higher losses in the material due to scattering. A common problem that is observed for all four materials when the printing temperature is too low is a blocked nozzle. As the viscosity of the material is too high to be extruded at lower temperatures, the material clots up in the nozzle leading to a blockage. If the temperature is too high, the material can burn. In table 4.1 the optimised printing temperatures for all four materials are shown. The given temperatures are the temperatures used on the UP2 Plus printer, and may vary for different printers as the temperature measured by the printer has an accuracy of ±7% [135].

The printing temperature is not the only setting that has to be optimised for successful 3D printing. The printer alignment is also an important factor, as a minor alignment problem could lead to major deformations of the printed object regardless of the material used. To demonstrate this, I printed three rectangles with a width of 1 cm and a length of 10 cm. I varied the height of the printing board for each rectangle. In Figure 4.1 the effects of the increase of the distance between the printing board and nozzle are shown. It can be seen that the larger the distance between the nozzle and printing board is, the more the printed object will deviate from the target model. In the case shown in Figure 4.1 the printing board is lowered to show the effect of the nozzle being too high. If the printing board was tilted, the printing quality would vary between different locations in the printed object, leading to a different object than intended. It is thus important to have the printing board aligned correctly and the nozzle height set up correctly to achieve a printed object that is an accurate model of the designed STL file.

Once the optimum printing settings were found, I printed several preform designs with the four different materials. In Figure 4.2 four of the preform designs that have been

TABLE 4.1: Printing temperatures for used materials

| **Material** | **Printing temperature** | **Observations for higher temperatures** | **Observations for lower temperatures** | **Reported temperatures** |
|---|---|---|---|---|
| *ABS* | 260 | No constant thickness of extruded filament, filament changes colour | Printer-nozzle blocks | 210-260 [87] |
| *PC* | 305 | Filament changes from translucent to opaque, breaks during extrusion | No constant thickness for extruded filament, printer-nozzle blocks | 270-300 [87] |
| *PLA* | 200 | No constant thickness for extruded filament | Printer-nozzle blocks | 180-230 [87] |
| *PMMA* | 230 | Filament changes from translucent to opaque, breaks during extrusion | Printer-nozzle blocks | 160-240 [136] |

Figure 4.1: Three printed samples with different printing bed alignment settings. The distance between the nozzle and printing board was 0.5 mm, 2.5 mm, 5 mm from left to right.

printed are shown, all with an outer diameter of 2 cm. Figure 4.2a shows the printed preform with elliptical cladding elements as designed in Chapter 3 printed in PLA and in 4.2b a structure with nested ellipses is printed. It can be seen that there appear to be gaps in the structure. The UP Plus 2 printer can print at 6 different filling settings, which are mainly designed for mechanical purposes to determine the strength of the printed object. The designs in Figure 4.2a and 4.2b were printed on the 'solid' setting. As there are gaps seen in the printed designs, I printed a rod to test how solid the printed preforms would be. When the density of the cylindrical rod was measured, it became apparent that not the whole preform was filled with the material, and its density was only 80% of that of the pristine polymer. This indicates that solid objects printed with this method typically have small air bubbles. This is a potential problem for the subsequent drawing process. Another printing setting that can be used is the surface setting. When using this setting, only the outer layer of the model is printed. To solve the problem with the density of the preform, I decided to print preform using the surface setting and use a jacket tube to increase the surrounds of the cladding whilst avoiding the air holes in the structure.

To test the surface printing setting, I printed an ARF with thin cylindrical tubes in the cladding and a design with nested tubes as seen in Figure 4.2c and 4.2d. Both preforms were printed using ABS and both were printed to the maximum length for the UP2 printer, which is about 13 cm. It can be seen that using the surface setting leaves a gap in the structure in Figure 4.2c. Drawing such a preform into fibre requires careful design of the jacketing sleeve and engineering of new ways of applying the various pressure differentials required to keep the tubular elements from collapsing.

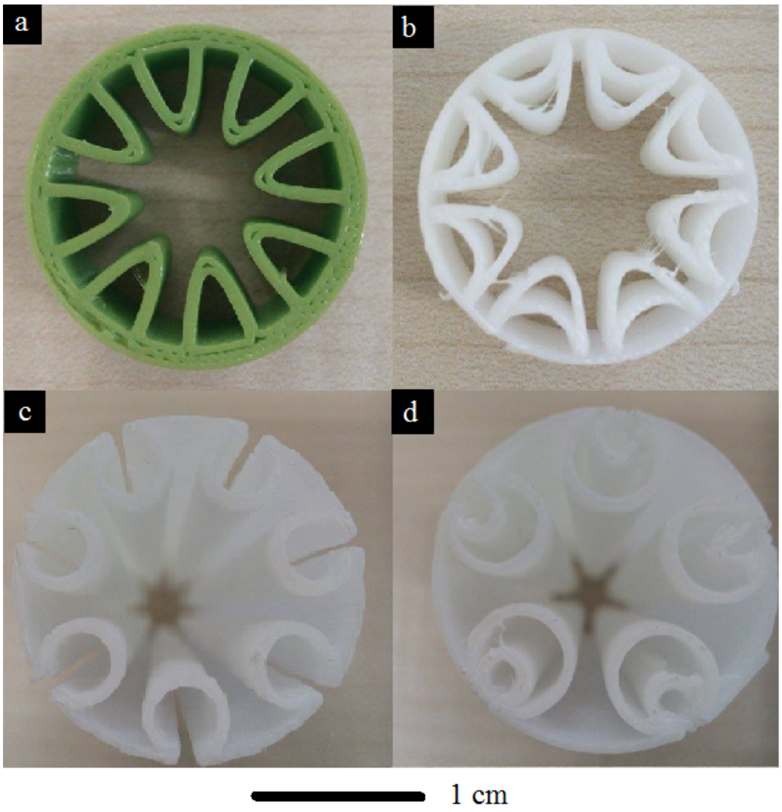

FIGURE 4.2: Four different printed antiresonant preform structures, a is printed in PLA and b, c and d are printed in ABS. The diameter of each preform structure is 2 cm. A and b are printed to a length of 1 cm, c and d are printed to a length of 13 cm.

## 4.3 Polymer fibre drawing

As the expertise within our group is primarily in drawing glass fibres, I asked my colleagues working on fibre fabrication and collaborating with me on the project to draw a 3D printed rod to investigate potential challenges in drawing 3D printed preforms. One of the potential issues lies in controlling the temperature during the drawing process. The drawing temperature for the polymers is close to the printing temperatures, around 200 °C. The drawing tower however is set-up to draw soft glasses such as chalcogenide, which softens at 310 °C [137]. We performed a first trial to see whether the lower temperatures for polymers are feasible with the set-up of the tower. The drawing work described in this Chapter is performed by my colleagues Dr. X. Feng, Dr. W. Belardi, Dr. J. Lousteau and N. White.

For the first attempt of drawing polymers, I 3D printed an ABS rod with a diameter of 1.5 cm and a length of 9 cm. My colleagues encountered problems in this first attempt due to the filling ratio in the ABS rod. To decrease the temperature in the furnace of the tower, they removed the covers around the preform to allow air to flow through. As mentioned in the previous section the UP printer can not print fully solid objects and thus leaves air bubbles in the structure. This turned out to be problematic during the drawing process, as the bubbles can expand irregularly, resulting in bursts on the surface and inflated areas along the drawn ABS.

For the second attempt we tried to pull an ABS rod with similar dimensions at a higher temperature of 350 °C. The rod was pulled into a thin fibre with a diameter of approximately 30 µm, however this draw produced fibres with large longitudinal diameter variations due to the bubbles in the rod, and due to the high temperature used during the drawing process a larger size could not be achieved. The susceptor used in the drawing tower during these draws had a minimum temperature of 330 °C. To lower the temperature and hopefully make it possible to draw preforms to a larger diameter fibre, a different susceptor was developed by my colleague N. White that can go to temperatures as low as 125 °C. The drawing tower was therefore set up with this new susceptor, as shown in Figure 4.3.

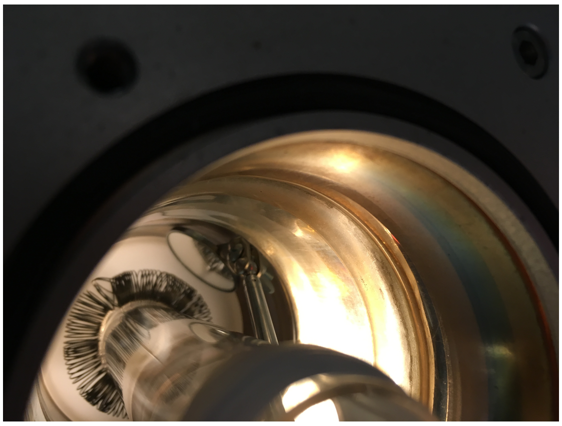

Figure 4.3: Susceptor installed in the drawing tower to enable the use of lower temperatures during the drawing process.

With the new susceptor on the drawing tower, we then focused on drawing PMMA. The PMMA rods were commercially sourced and as a result do not have the same filling ratio problems as the printed ABS rods had. The attempts to pull these purchased PMMA rods were successful, a solid rod with an initial diameter of 1.5 cm was drawn into a thinner cane with a uniform diameter of approximately 1.7 millimetre. This diameter was targeted as it is the same size as the filament needed in the UP printer and I used the drawn filament to print other test structures, but the diameter of the filament showed variations as high as ± 0.3 mm or 18%.

From these initial drawing tests and the printing analysis in the previous section, we found the following potential problems in drawing 3D printed polymer preforms:

- The difference between polymers and glasses when heated
- Bubbles in the printed preforms

In the next section, I use a capillary drawing model to aid in the understanding of the differences between polymers and glasses during the drawing process.

### 4.3.1 Modelling of Non-Newtonian fluids

To understand the differences between polymers and glasses, I consider the Non-Newtonian properties of polymers. Differently from glasses, which when heated behave like Newtonian fluids, when heated above the glass temperature polymers have Non-Newtonian properties. The viscosity, the fluids resistance to stress, behaves differently in a Non-Newtonian fluid. In glasses the viscosity is only dependent on the temperature, as per Newton's viscosity law. In polymers, the viscosity is dependent on the shear stress as well as the temperature, either thinning or thickening under stress [138].

The variations in the diameter we observed during the drawing tests of the polymer rods suggested that the Non-Newtonian nature of the materials potentially needs to be taken into account in order to fully understand and improve our fabrication processes. As a result I decided to examine the drawing process and the thermo elastic behaviour of the PC and PMMA theoretically.

There are different models that can be used to approximate the viscosity of a Non-Newtonian fluid. To calculate the viscosity of a polymer with shear-thinning/thickening taken into account, one of the approximations that can be used is the power law in Equation 4.1 [139; 140]. Although the power law is a reasonable approximation for the effective viscosity of a Non-Newtonian fluid under a certain shear rate, there are limitations to this approximation, as the power law suggests that the effective viscosity approaches zero for infinite shear stress. However, any real fluid would have a minimum and maximum viscosity [139]. Some models, for example Quemada's model, do take this into account and are adapted to converge to a minimum and maximum viscosity [139; 141]. Other models take more external parameters into account, such as the yield stress and time-dependent relaxation in the fluid [139]. However, the power law is mathematically one of the simplest approaches to include the shear-thinning effect of the polymers, whilst still being an accurate approximation and therefore I use the power law to approximate the viscosity during the drawing process [139]. The power law is defined as:

$$\mu_{eff} = K * \gamma^{N-1} \tag{4.1}$$

Where $\mu_{eff}$ is the effective viscosity, $K$ the flow consistency index (the viscosity at a shear rate of $1s^{-1}$), and $\gamma$ the shear rate, which is defined as the rate of change in the velocity. N, the flow behaviour index, indicates whether the fluid is shear thinning ($N < 1$) or shear thickening ($N > 1$). The fluid behaves in a Newtonian fashion when the flow behaviour index equals 1. The flow consistency index is a material constant, but is temperature dependent.

#### 4.3.1.1 Capillary drawing simulations

As fibre drawing is an expensive and time consuming process, it is useful to have models that can be used as a guideline for the draw parameters to use during the drawing process. The first step to modelling fibres with void regions is to study the drawing process of a capillary. Fitt et al. have developed a fluid dynamics model studying thin capillary drawing for Newtonian materials [73]. In this model they describe the behaviour of a thin tube during the drawing process. These thin tubes are a starting point towards ARF drawing, as they are a simple approximation of hollow fibres, but at the same time the thin tubes drawn could also be used to create a preform through a stacking process. Equations 4.2, 4.3, 4.4 and 4.5 report this model, which is derived from the Navier-Stokes equations and convection-diffusion equations:

$$\rho(h_2^2 - h_1^2)[u_{0t} + u_0 u_{0x} - g] = [3\mu(h_2^2 - h_1^2)u_{0x} + \Gamma(h_1 + h_2)]_x \tag{4.2}$$

$$(h_1^2)_t + (h_1^2 u_0)_x = \frac{p_0 h_1^2 h_2^2 - \Gamma h_1 h_2 (h_1 + h_2)}{\mu(h_2^2 - h_1^2)} \tag{4.3}$$

$$(h_2^2)_t + (h_2^2 u_0)_x = \frac{p_0 h_1^2 h_2^2 - \Gamma h_1 h_2 (h_1 + h_2)}{\mu(h_2^2 - h_1^2)} \tag{4.4}$$

$$\frac{h2^2 - h1^2}{2}[\rho c_p(T_0 + u_0 T_x) - k(T_x)_x - \sigma\alpha(T_a^4 - T_0^4)] = h_2 M(T_a - T_0) \tag{4.5}$$

where $h_1$ and $h_2$ are the inner and outer radius of the capillary, $\rho$ the density of the material, $g$ the gravitational constant, $\mu$ the viscosity, $\Gamma$ the surface tension, $p_0$ the pressure in the capillary, $c_p$ the specific heat, $\sigma$ the Stefan-Boltzmann constant, $\alpha$ a material constant that includes the emissivity, $T_a$ the ambient temperature in the furnace, $T_0$ the initial temperature of the capillary, $T(x)$ the temperature along the fibre, $M$ the heat-transfer constant (assumed constant for simplicity) [73]. The direction of the capillary drawing is assumed along the $x$-axis, and $t$ is the time, $u$ is the speed of the viscous softened material in the $x$ and $t$ shows the derivative of the value in $x$ and $t$ respectively.

These coupled equations are solved to find the final dimensions of a capillary when initial conditions are known. At steady-state, when all time derivatives equal zero, the equations can thus be rewritten as:

$$\rho(h_2^2 - h_1^2)[u_0 u_{0x} - g] = [3\mu(h_2^2 - h_1^2)u_{0x} + \gamma(h_1 + h_2)]_x \tag{4.6}$$

$$(h_1^2 u_0)_x = \frac{p_0 h_1^2 h_2^2 - \gamma h_1 h_2(h_1 + h_2)}{\mu(h_2^2 - h_1^2)} \tag{4.7}$$

$$(h_2^2 u_0)_x = \frac{p_0 h_1^2 h_2^2 - \gamma h_1 h_2(h_1 + h_2)}{\mu(h_2^2 - h_1^2)} \tag{4.8}$$

$$\frac{h2^2 - h1^2}{2}[\rho c_p(T_0 + u_0 T_x) - k(T_x)_x - \sigma\alpha(T_a^4 - T_0^4)] = h_2 N(T_a - T_0) \tag{4.9}$$

In Figure 4.4 a schematic overview of the problem is drawn. Although there are a lot of parameters in these coupled equations, most of them are constant. The dynamic parameters in these equations are $h_1$, $h_2$, $T$, $u$ and $\mu$, as well as derivatives of these parameters. The initial values for the inner and outer radius of the capillary are known, but the dimension profile along x needs to be solved. The profile of the speed, $u$, also needs to be solved. The initial and final value for this parameter are known, the initial value is the feeding speed of the preform ($U_f$), the final value is the drawing speed ($U_d$). In this model, I will impose a temperature profile on the fibre, so T(x) is known. If the material used was Newtonian, this would mean that the viscosity profile, $\mu$, could also be known directly. However, as shown in Equation 4.1, this is not the case for non-Newtonian materials, as the viscosity depends on the temperature and the shear rate. The shear rate, $\gamma$ from equation 4.1 is defined as:

$$\gamma = \frac{V}{x}$$

Where $V$ is the velocity difference between two points and $x$ the distance between the same two points. In the coupled equations 4.6, 4.7, 4.8 and 4.9, the speed causing the shear stress comes from the change in diameter, and thus speed $h_1$ changes at.

This means that to solve the coupled equations need to be solved for $h_1$, $h_2$, $u$ and $\frac{du}{dx}$ . In the next subsection I will discuss how these equations can be solved.

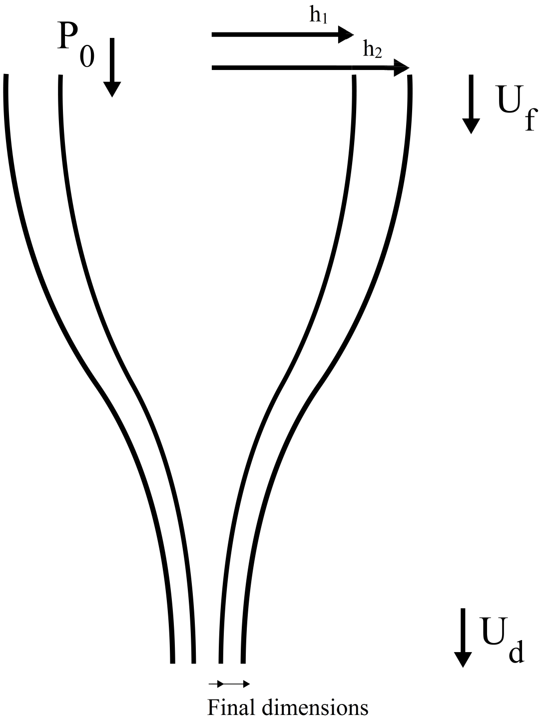

FIGURE 4.4: Schematic drawing of model and parameters used to calculate tube ID and OD during drawing process.

#### 4.3.1.2 Shooting method to solve Boundary Value Problems

Differential equations as shown in Equations 4.6, 4.7, 4.8 and 4.9 can be solved in different ways, depending on the constraints given to solve them. Differential equations can be used to describe an Initial Value Problem (IVP), in which case all initial values that need to be solved for are known and the equations can be used to calculate how the described problem will evolve from the known values. IVPs have one unique solution. In the problem described in the previous section, initial values for $h_1$, $h_2$ and $u$ are known. The missing initial value $\frac{du}{dx}$ means these equations can not be solved directly, and therefore these equations describe a Boundary Value Problem (BVP). A BVP consists of a set of differential equations, where the solution also has to satisfy the given boundary conditions. In this case, the boundary conditions are given by the initial speed and capillary dimensions, which are given at $x = 0$, the beginning of the capillary drawing. The speed at the end of the fibre drawing (the draw speed), is also a boundary condition. BVPs can have multiple (or even zero) solutions.

As the problem can't be solved directly due to the missing initial parameter, I use the shooting method to turn the problem into an IVP. Using the shooting method, a 'guess value' is used for the initial value for $\frac{du}{dx}$ [142]. The equations will be solved using this guess value, and a solution for the final inner and outer diameter as well as the final speed will be found. As the final speed is known from the boundary conditions, the solution can be compared to the boundary condition, and if it does not satisfy this boundary condition, a new guess value is chosen. This process repeats until the guess value results in a solution for the final value of $u$ that matches the drawing speed within a tolerance of 1%.

To solve the IVP using a guess value, I used a python model based on Finite Differences (FD). The x-domain of interest is divided into small differences, $\delta x$. For example, if $f(x)$ and $\frac{\delta f}{\delta x}$ are known, $f(x + \delta x)$ can be calculated using:

$$f(x + \delta x) = f(x) + \frac{\delta f}{\delta x} * \delta x \tag{4.11}$$

The behaviour of $h_1$, $h_2$, $T$ and $u$ along the x-domain between the boundary conditions can be calculated using FD when the differentials are isolated from Equations 4.6, 4.7, 4.8 and 4.9. The FD method is used to calculate what the final dimensions of the capillary would be, but also to calculate the final speed. The final speed is then compared with the boundary condition for the drawing speed. If the difference is within the set tolerance of 1%, the solution is accepted as valid. If the difference is outside of the set tolerance, a new guess value for $\frac{du}{dx}$ is chosen based on the previous value and the difference between the expected boundary and calculated boundary value [142].

I developed a Python model to solve this IVP, see Appendix A. Python is an open-source programming language that supports object orientated programming [143; 144]. Although Python was not initially developed for scientific programming, has become widely popular as a scientific computing tool, with hundreds of specific libraries and algorithms developed and made available via openSource [144]. Numpy is one of the libraries which is used to solve the BVP described in this chapter [145]. The visualisation of the results is done using Matplotlib [146].

To validate my python code, I compared its predictions to published results from Fitt et al for silica glass [73]. As silica is Newtonian, the shear rate and its effect on the viscosity do not have to be considered for these calculations. Fitt et all did six different sets of experiments, using three different temperatures (1900, 1950 and 2000 °C) and three different feeding speeds (2, 4 and 8mm/min). For each set, three different drawing speeds are used and the final ID and OD of the silica capillaries is measured. I used these same values to calculate the expected ID and OD and compared my calculations with the results as shown in the original paper, to make sure the model is set up correctly and the results are reliable. In Figure 4.5 these results are shown and it can be seen that the models are in agreement. The error margins in the calculated value are due to the tolerance of 1% in the model. Now the model is validated, the next step is to include the Non-Newtonian effects and tailor the model to fit the capillary drawing experiment as closely as possible.

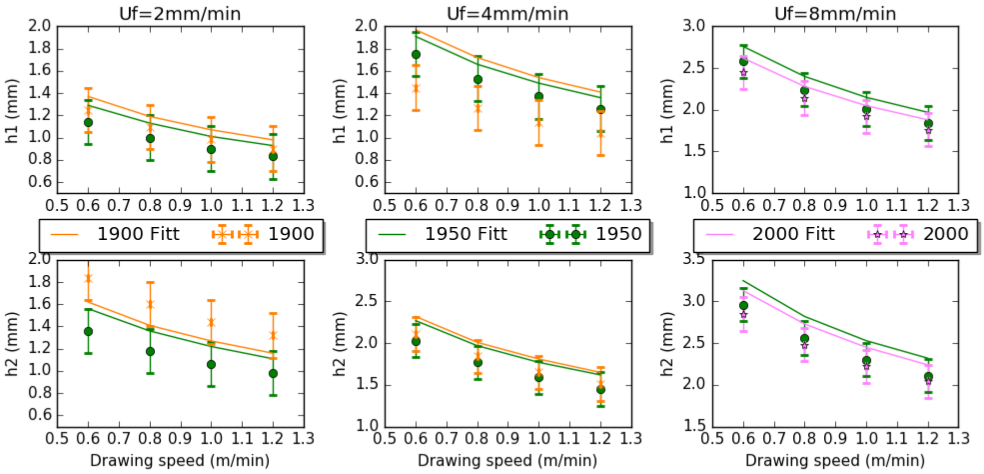

FIGURE 4.5: Silica drawing numerical results compared with the results from Fitt et all [73]. Tubes are drawn at three different temperatures using three different feeding speeds, leading to six different data sets.

There are two main uncertainties in this model: the exact viscosity of the material and the temperature profile. Instead of calculating the temperature using Equation 4.9, a temperature profile is imposed on the preform, which is the temperature profile of the furnace. As the capillary would be heated using a coil, a tapered increase and decrease in the temperature is used, from just over the softening point to the temperature of the furnace. I used a Gaussian to approximate the temperature, and the Power-Law model to approximate the viscosity.

#### 4.3.1.3 Experimental results compared to calculated results

To verify the modelling predictions and the correct implementation of the Non-Newtonian model, we draw capillaries from two different Non-Newtonian materials, PMMA and PC, at three different speeds and compare the drawn tube sizes to the calculated dimensions of the capillaries. The material properties used to model the capillary drawing for

PMMA and PC are shown in Table 4.2. The first material to be drawn and modelled is PC which has an N-index of 0.8 i.e. fairly close to 1. In contrast, PMMA has a much lower N-index of 0.25 [140]. As the N-index for PC is closer to 1, PC behaves more Newtonian and thus more glass-like than PMMA.

TABLE 4.2: Overview of material constants used for PMMA and PC in Non-Newtonian capillary drawing model

| | PMMA | PC |
|---|---|---|
| n | 0.25 | 0.8 |
| Density | 1150 $kg/m^3$ | 1200 $kg/m^3$ |
| Specific heat | 1450 $J/kg/K$ | 1200 $J/kg/K$ |
| Surface tension | 0.035 $N/m$ | 0.038 $N/m$ |
| Emissivity constant | 0.94 | 0.9 |
| Glass transition temperature | 170 °C | 147 °C |

A PC tube was extruded for this experiment by my colleague N. White, with and inner diameter (ID) of 2.5 millimetres and an outer diameter (OD) of 11 millimetres. The tube was then drawn in the tower, where the feed speed was set to 1 mm/min and three different drawing speeds were used: 1, 3 and 6 m/min. The temperature, 260 °C, stayed the same throughout the process. These values are then used in the model with the parameters for PC, and the results compared. No pressure was used during the drawing of these tubes.

Measurements of $x$ and $y$ for the drawn capillary are taken at three different points in the tube for each drawing speed and an average is taken from these measurements to account for instabilities during the drawing process. The error margins for the experimental values are calculated from the variation in these measurements. For the thinner capillary, where the cleaving may have compressed the capillary into an oval shape, the minor and major axis are used to calculate the original ID and OD for a circular tube. The error margins for the calculated value come from the tolerance in the result, the solution is accepted when the tolerance is less than 1%. The results are shown in Figure 4.6.

To study the shear-thinning effect in the PC drawing, the calculated values are also plotted for the model where the Non-Newtonian shear-thinning effects are neglected. In this case, the softened polymer is treated as a Newtonian material and the viscosity is calculated based only on the temperature dependence. It can be seen that the differences between the Newtonian and the Non-Newtonian calculation are relatively small for PC, and both results overlap with the error margin in the experimental results. This shows that when using a polymer like PC where the N-index is close to 1, the shear-thinning effect only plays a minor role in determining the final dimensions and approximating the material as Newtonian gives adequate predictions for the final ID and OD for capillary

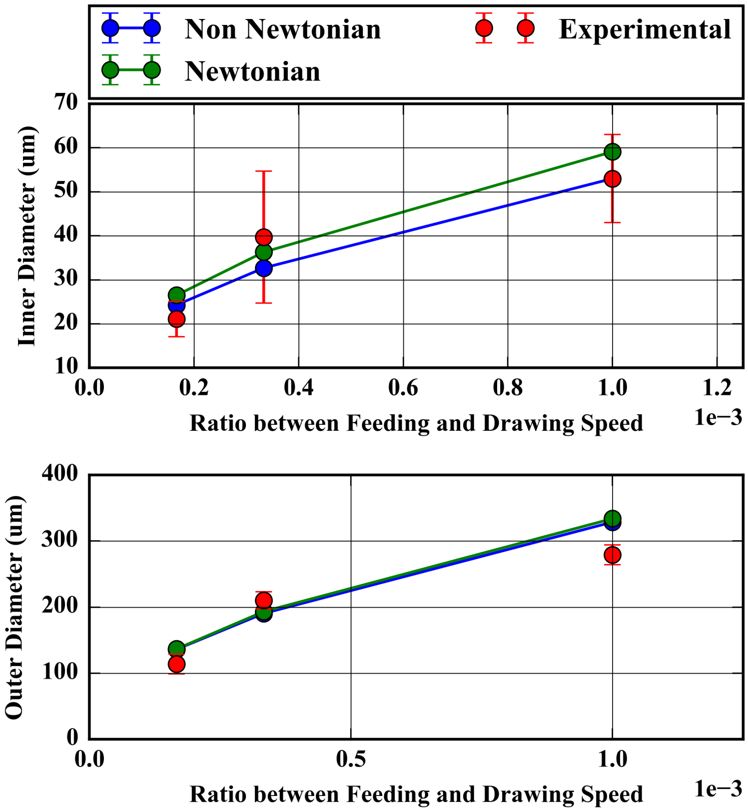

FIGURE 4.6: Comparison between calculated measured final diameter for PC tube.

drawing.

Although the differences between the Newtonian and Non-Newtonian calculation are small, it can be seen from Figure 4.6 that the shear-thinning effect leads to a smaller tube compared to a tube where no Non-Newtonian effects are present, and this is to be expected since the polymer has lower viscosity under the drawing stress as a result of its shear-thinning properties. In the experiment performed by Fitt et al, silica tubes were drawn at three different temperatures. Increasing the temperature lowers the viscosity, and the tube dimensions for the draws at higher temperature were also smaller.

The same experiment was repeated with PMMA tubes for which shear-thinning effects are expected to play a significant role. The initial dimensions of these tubes were slightly larger, with an OD of 13 millimetres and ID of 2.5 millimetres. The drawing speed in PMMA was slower than used for PC, as the aim was to create larger, cane-sized tubes to minimise measurement uncertainty. Due to the visco-elasticity in PMMA and to the larger Non-Newtonian effects, the polymer proved difficult to draw to smaller sizes whilst obtaining a stable outer diameter in previous tests. However, using a smaller draw-down ratio between, the shear rate is reduced and the drawing process is easier.

In Figure 4.7 a cross-section of one of the measurements taken for the drawn PMMA capillary is shown. In Figure 4.8 the experimental results are compared to the calculated results. In Figure 4.9 the temperature profile and viscosity for the PMMA drawing are also shown. It can be seen that at the beginning of the neck-down, the difference in the viscosity is the most significant, this is explained by the higher shear-rate at the beginning of the draw. There also appears to be a sudden drop, as the drawing in the simulation does not start until a low enough viscosity is reached for the material to be drawn. At this point, the shear stress is high, causing a significant decrease compared to the 'Newtonian' profile.

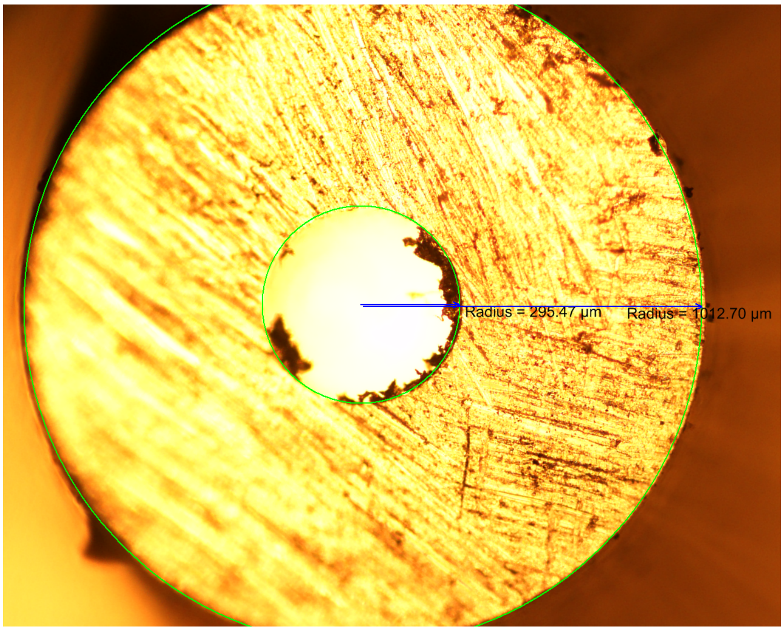

FIGURE 4.7: PMMA tube sample after drawing down from 13mm OD to 2mm OD.

It can be seen that the model is in excellent agreement with the experimental results, and it can also be seen that the difference between the Newtonian and Non-Newtonian calculations is more significant, especially for the ID of the tube. This shows that it is important to take the shear-thinning effect into account to get accurate prediction of the hole size for capillary drawing when using polymer where the N-index is much lower than 1.

The model demonstrated in this chapter so far only focuses on capillary drawing. However, this model could be expanded to more complex structures for ARF fabrication in polymers where the shear-thinning effect is significant. It can also be concluded that some polymers could be treated as Newtonian without a significant change in the final result, whilst simplifying the calculations [147]. More complex models for fibre structures are already available for Silica [74], and would need adapting for some Non-Newtonian

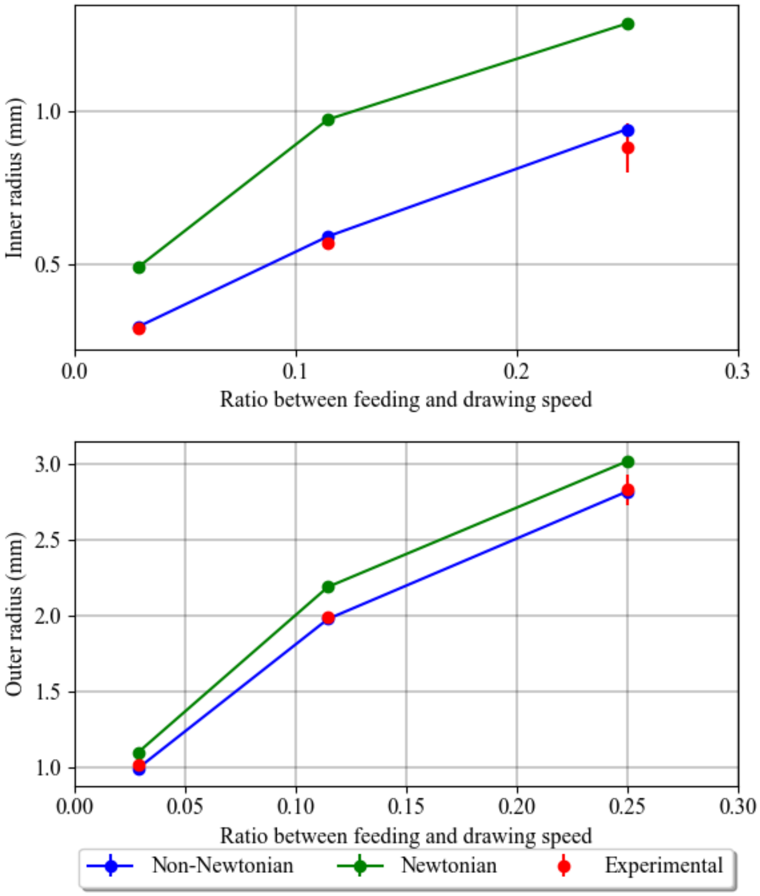

FIGURE 4.8: Comparison between calculated measured final diameter for PMMA tube.

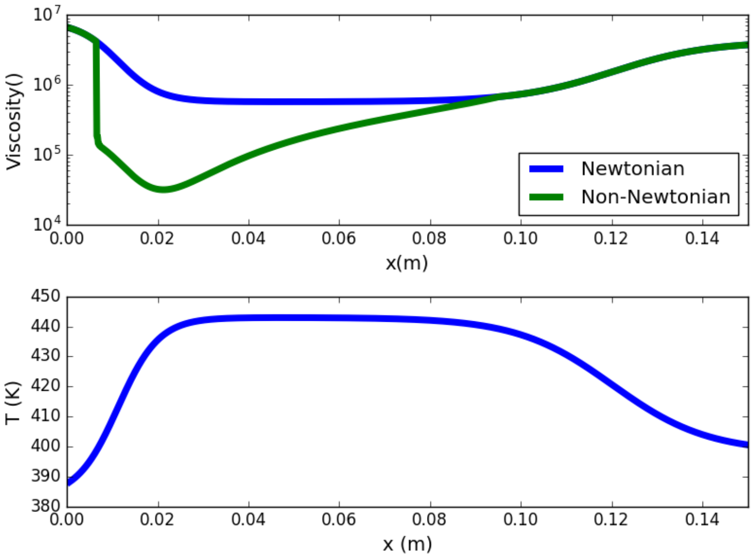

FIGURE 4.9: Viscosity and temperature profile for PMMA capillary drawing calculations.

materials where the effect of shear-stress is large.

Another important conclusion to draw from this model is that PC behaves more glass-like than PMMA and the Non-Newtonian behaviour in this material is therefore significantly lower during the drawing process. As the experience within our research group lies in drawing glasses, I therefore decide to continue the fibre fabrication process with PC instead of PMMA.

## 4.4 Wagonwheel fibre

For the first trial of a fibre drawing from a printed preform with holes, I decided to keep the geometry as simple as possible and use a wagon wheel fibre design. This design is suitable for a first trial due to the fact that all air holes are similar in size. As a result, only one pressure is needed for the whole preform , instead of multiple pressure regions as would be required for a HC ARF. The preform has four spokes and a solid core. The idea was to use this design as a simple test, and to move on to ARF designs as a next step.

The Solidworks preform design I produced to 3D print the preform for the wagon wheel fibre is shown in Figure 4.10. It can be seen that all air holes are equal in size, and the core is solid. To fabricate the fibre, a two-stage fibre draw is planned. The first step of this process is to draw the fibre down to a cane with a diameter of a few millimetres. This cane is then jacketed using a commercially sourced tube, and the resulting preform is drawn down to a fibre.

For the first try the PC preform is printed using the 'solid' setting on the UP printer. As shown in the previous section, PC behaves more like glass than PMMA, and as the expertise of our group lies in drawing glass, the wagon wheel preform is printed using PC. This preform was successfully drawn into a cane with a diameter of 1.5 mm. The cross-section of this cane is shown in Figure 4.11. However, the cross-section revealed multiple holes in the core of the preform as well as slight deformations in the fibre structure as seen in Figure 4.11. It should also be noted that the cleaving process for large HC polymer fibres can lead to imperfections on the cane/fibre end. A diagram of the cleaving tool used is shown in Figure 4.12. The cane is held in the circular hole in the metal block, and to cut it a knife blade is pushed straight down. For solid fibres, the hole in the cleaving tool can be used to maintain the circular shape. As our cane has hollow regions, deformations can arise from the pressure of the blade pressing down.

To overcome the problem of the holes in the cane, I decided to print the next preform using the surface setting. Using this setting, only the outline of the CAD model is printed. The model I made for this structure is shown in Figure 4.13. The gap between the core

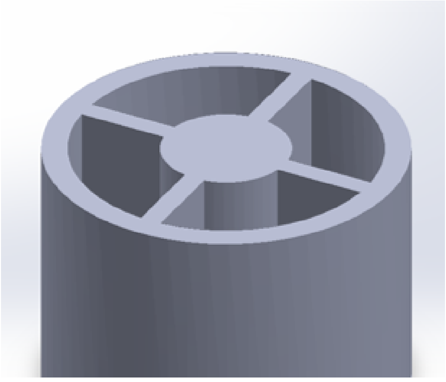

Figure 4.10: CAD model for wagon wheel fibre with four equal air holes and solid core.

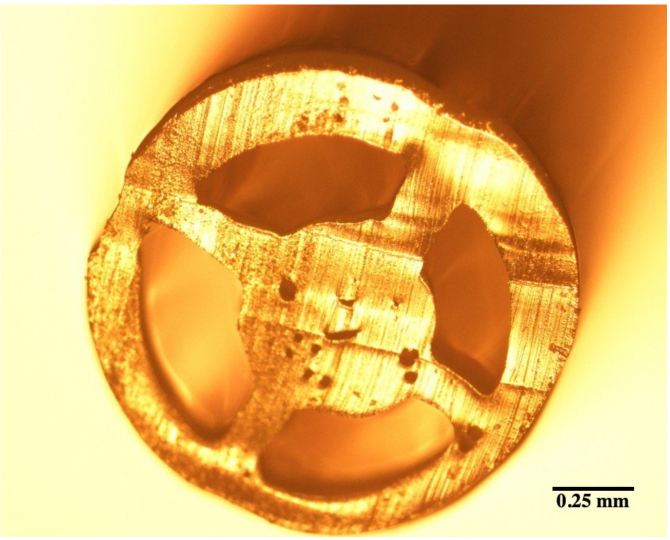

Figure 4.11: Cross-section of drawn PC wagon wheel preform into a cane with a diameter of 1.5 mm

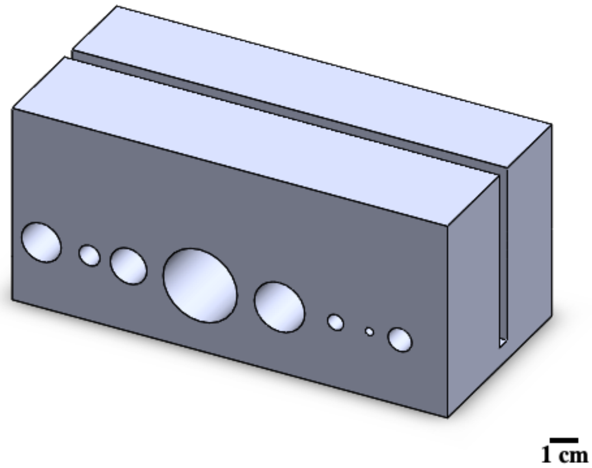

Figure 4.12: Diagram for cleaving tool used for cleaving of polymer canes and fibres.

outline and the outline of the cladding structure creating the spokes in the wagon wheel is filled when printing as the width of the printed filament is not taken into account in the model. To achieve a solid core without the air holes that result from the 3D printing process, a piece of all solid filament is inserted in the core. The core is made of the same commercially sourced filament as is used for the 3D printing of the preform. The produced preform is shown in Figure 4.14. Although this method reduces the number of air holes in the core, it also leads to less flexibility in the design. The core size is limited to the available solid rods, in this case the filament, and the thickness of the spokes in the wagon wheel is limited to the extruded filament's size. This design was nonetheless extremely useful for testing and calibrating the drawing process.

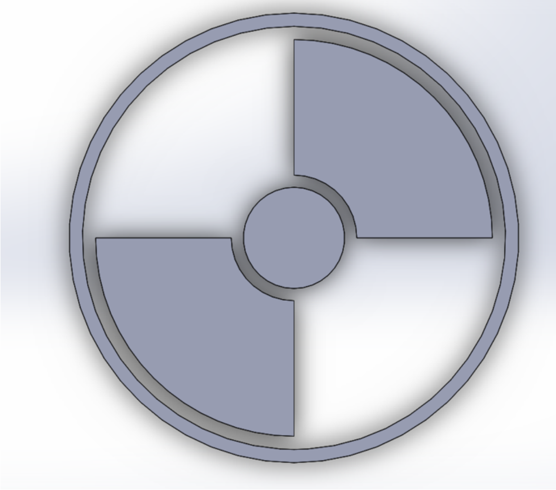

Figure 4.13: CAD design for wagon wheel preform to print using the surface setting.

Figure 4.14: Cross-section of drawn PC wagon wheel preform printed using surface setting with filament inserted into the core to create a solid core.

This preform was also drawn into a cane. The first trial with this preform uses no pressure in the preform and draws the preform down to a cane with a diameter of 1.1 mm, as shown in Figure 4.16. There are less holes in the core of this cane compared to the first trial shown in Figure 4.11. The holes in the core of this cane are caused by the imperfect fit of the filament and the printed structure, since they form a circle in the core, instead of the air holes in the printed preform. We also found that such small air-holes were present in the cladding of the cane. Further examination of the cane also revealed non-uniformities along its length, which may contribute to higher attenuation in the resulting fibre. It can also be appreciated that using this process, the spokes of the wagon wheel are significantly thicker than in the previous method. If drawn to fibre, this too may result in increased attenuation since they will deteriorate the confinement of the mode-field to the central core area. To study the effect of the thickness of the spokes, I performed a study in COMSOL to analyse the loss dependence on the thickness of the spokes. For this study I use a fibre with a core radius of 1 µm, a spoke length of 4 µm and varying spoke thickness. The loss is calculated at a wavelength of 632 nm. Figure 4.15 shows the results of these calculations which demonstrate stronger leakage and thus higher loss when the thickness of the spokes is increased.

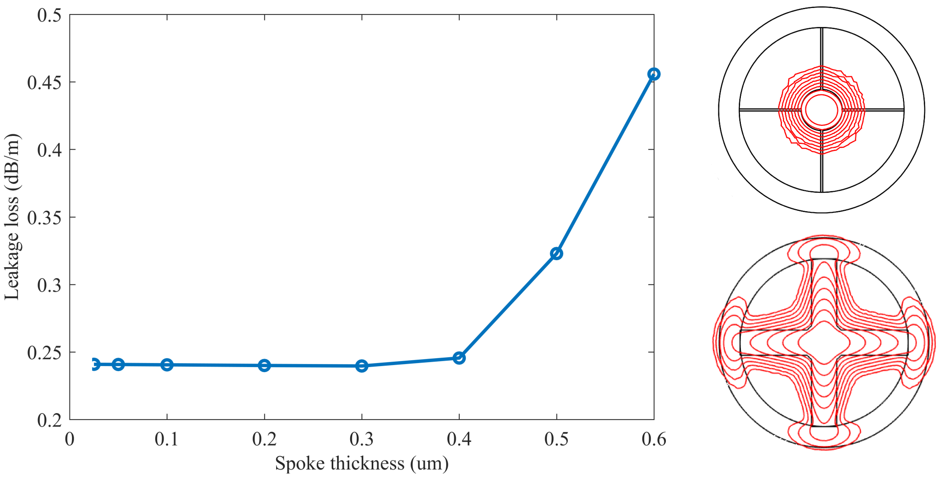

FIGURE 4.15: Leakage loss of wagon wheel design dependant on the spoke thickness. Two mode profiles for a spoke thickness of0.025 µm (top) and 0.6 µm (bottom) show that leakage through the spokes increases for increasing thickness.

In an attempt to reduce the thickness of the spokes in the structure, I printed an identical preform to repeat the drawing process, using 0.3mBar pressure within the four cladding holes to expand them and thus reduce the thickness of the spokes. The drawing temperature remained 260 °C A cane of approximately 30 cm length was fabricated. In Figure 4.17, microscope images of the cross-section of this cane are shown. It can be seen that the spoke thickness is reduced compared to the first trial. In a part of the cane, approximately 10 cm, the cane has burst due to one of the holes being over pressurised, this can be seen in Figure 4.17b. However, most of the cane is in a good condition with

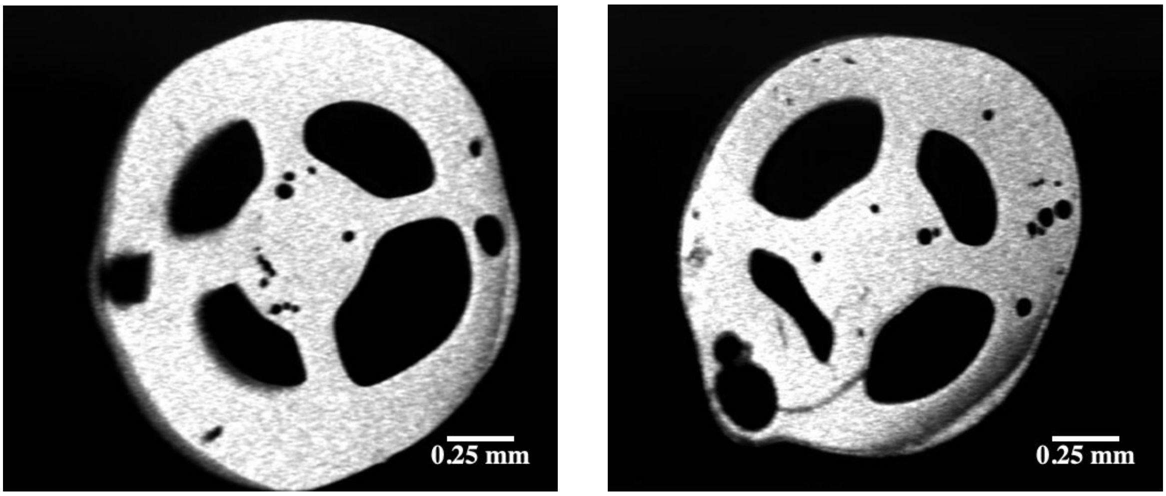

FIGURE 4.16: Cross-section of PC wagon wheel preform drawn into a cane with a diameter of 1.1 millimetres at two different points in the cane.

equal lobes in the wagon wheel, so to have a complete idea of the polymer drawing, this part was jacketed using a PC tube and drawn into a fibre.

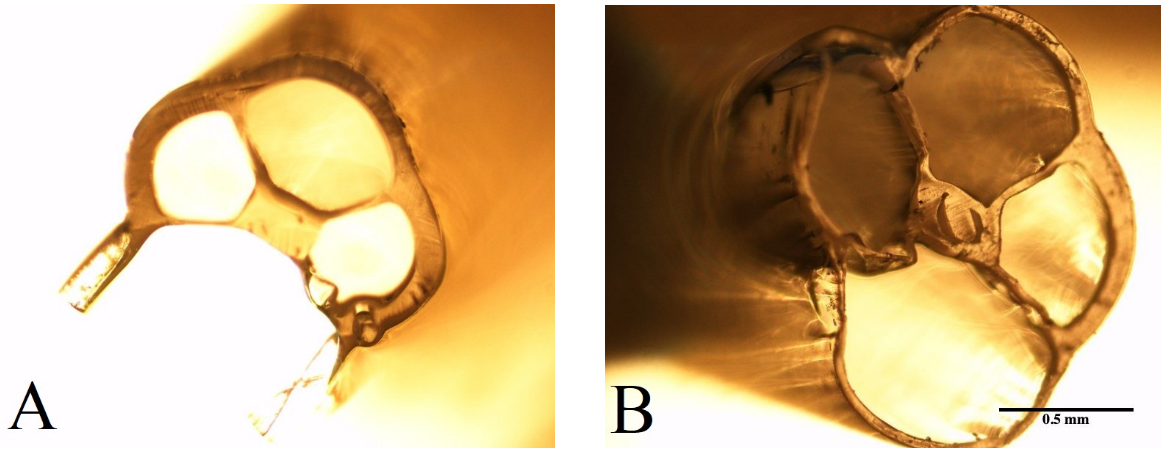

FIGURE 4.17: Wagonwheel preform cane drawn using 0.3 mBar pressure. (a) Area of drawn preform where pressure caused cane to burst. (b) Successfully drawn preform into cane for fibre fabrication.

To jacket the cane for the second step of the drawing process, a PC tube is required. To achieve the right dimensions to fit the cane in the jacket tube, it was decided to source a PC rod that could be extruded. Although PC is commercially widely available, we found that the thermal properties of the material could vary between samples.

The first rod used in extrusion had an outer diameter of 20 mm, and was extruded using a die temperature of 179 °C into a tube with an inner diameter of 2 mm and an outer diameter of 10 mm. However, the tube was not straight and there were bubbles entrapped in the extruded tube. To improve the quality of the extruded tubes, the next rod is degassed and annealed before the extrusion process. When a material is annealed, the temperature is slowly increased so that the internal stresses in the material can be released. When using pressure during this process, the material can also be degassed, which can hopefully be used to reduce the bubbles in the sample. The degassing and annealing process uses about 10 mBar pressure and a temperature of 90 °C. The rod is degassed for 42 hours. This rod is subsequently extruded into tube with a die temperature of 189 °C. This tube is clearer than the first attempt, but there were still entrapped bubbles in the tube. There was also a rippling effect on the surface.

As there is little information about the thermal and optical properties of the material bought, we decided to source rods from a different supplier. The rods for all the next tests have been made by Ensinger [148]. The rod has a diameter of 40 mm. As the degassing previously showed an improved, the same procedure is repeated for this rod, but for a longer time: 171 hours. Two different samples from the same batch have been used to extrude tubes with an inner diameter of 2.5 mm and an outer diameter of 10 mm. Surprisingly, the results are very different. The first sample is successfully extruded into a straight, clear and smooth tube. The second sample had many bubbles of different sizes and the surface shows some ripples. Both samples were clear.

The third test with the Ensinger rod used the same parameters, and resulted in a clear, straight, smooth and bubble-free tube. In the next test, the temperature for the annealing process is increased to 95 °C with the aim to improve the degassing process. The tube drawn from this sample showed small bubbles near the inner bore of the tube, and the number of bubbles seemed to increase towards the end of the tube. In an attempt to improve the surface quality of the tubes, the next rod is extruded at a higher temperature of 208 °C. This tube was clear and smooth, but due to the higher temperature the tube was slightly tapered.

The variation between the different samples could be due to different factors, for example, the time elapsed between degassing the samples and their extrusion. It could also be that the material properties vary along the length of the bought stock-rod, meaning that the viscosity characteristics vary between the different samples. To aid in understanding these differences, more tests were performed using subsequent pieces of the rod bought from Ensinger using the same extrusion parameters: a degassing temperature of 95 °C and a die heater temperature of 195 °C. In Figure 4.18 the resulting tubes for these tests are shown. It can be seen that the quality of the tube is different for each tube, and it appears that the quality of the tube is more dependent on the initial sample than the parameters used to degas and extrude the rod.

FIGURE 4.18: Four different Polycarbonate tubes all extruded from the same rod under the same conditions.

As we have smooth, clear and bubble-free jacket tubes available from the extrusion test, we decided to use the clearest part of the jacket tubes available to draw the cane. Using the jacket tube, the cane and jacket were drawn successfully into a fibre. The cross-section of this fibre is shown in Figure 4.19. One of the four holes significantly over-expanded, which shows the pressure was not equally distributed over the cane. Studying the printed preform and the cane, we concluded that the problem with the pressure may have been due to the air holes in the cane from the 3D printing.

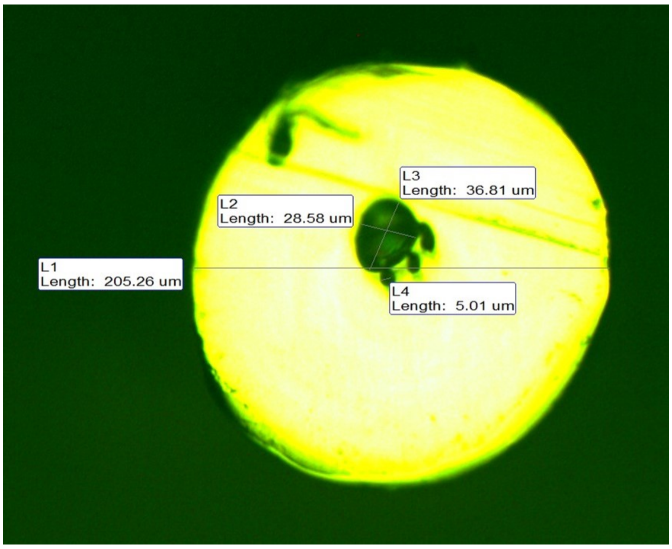

FIGURE 4.19: Wagonwheel fibre drawn from jacketed cane.

From these initial experiments it is concluded that the fabrication process of polymer fibres from 3D printed preforms poses several challenges, some of them stemming from the inherent properties of the polymer materials, but more importantly from the limited quality of the printed preforms achieved with the device available to us. Indeed, we noticed the air holes appearing in the printed preform, which along with their rough surface dictated by the printing filament pose new challenges during the draw. One of the problems is caused by the layered structure of the printed preform and the air holes that exists in these layers. One potential solution to improve the surface quality of the printed preforms would be annealing. As described in this section, annealing can be used to reduce internal stresses in a material. It could be that the air holes within the printed preform could be reduced by annealing, if the material would soften enough to reduce the holes without losing its structure. Therefore we decide to test if annealing is effective in improving the surface quality of printed preforms.

## 4.5 Annealing

Annealing is a heat treatment often used to reduce stress and toughen the material that is annealed. When a material is annealed it is heated up slowly to the annealing temperature and cooled down slowly to room temperature [149]. The annealing temperature is at a temperature where the material softens enough to relax internal stresses but is not soft enough to deform the structure [149]. Cook et al report improvement in their 3D printed preforms as a result of annealing [82; 150]. In Figure 2.7 this preform is shown where a change in the material's transparency was observed after annealing [82]. This preform however was fabricated using a polystyrene mixture containing styrene-butadienecopolymer and polystyrene instead of PC, and also had a different structure. The fibre design of their preform is a solid core surrounded by a single-layer of circular air holes. In the annealing test shown in this section, I used thin tubes which are closer to the ARF preform that I would be printing for this project.

In an attempt to reduce the bubbles, holes and surface roughness in the 3D printed preforms fabricated using the UP printer, I performed several annealing experiments on printed PC tubes. The tubes are all the same length, 5 cm. The tubes used are all printed using the same batch of PC filament and using the surface setting. For an initial test, the tubes are heated to 4 different temperatures, 125 °C , 150 °C, 175 °C and 200 °C. The tubes are initially kept at these temperatures for 30 minutes. In the annealing process, the tubes are heated up (using an increase in temperature of 5 °C per minute), kept at high temperature and then cooled down slowly (in this case 1 °C per minute). In Figure 4.20, the results are shown for each tube. Careful analysis of the samples before and after treatment indicated that for these four tests no change is seen in the tube. At 200 °C the tube has deformed, as it collapsed due to the heat, though there is no reduction in holes, bubbles or surface roughness.

PC tube after annealing for 30 minutes at 125 °C .

PC tube after annealing for 30 minutes at 150 °C .

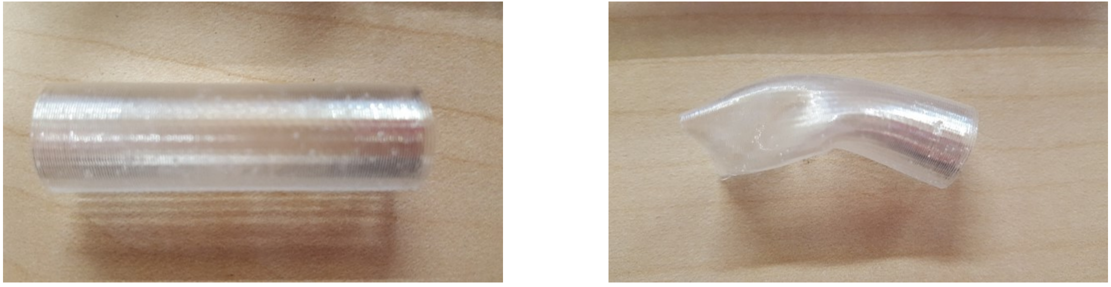

PC tube after annealing for 30 minutes at 175 °C .

PC tube after annealing for 30 minutes at 200 °C .

Figure 4.20: PC tubes annealed for 30 minutes at four different temperatures.

From this first set of experiments, it can be concluded that 200 °C is not a suitable temperature to anneal the PC tube, as it deforms before any of the surface roughness and bubbles is resolved. To see whether the material can be made smoother with less bubbles as a result of annealing, I printed another tube and annealed it at 175 °C for 72 hours, using the same temperature ramp up and down as in the previous experiments. In Figure 4.21 it can be seen that although the tube is clearly collapsed during the process, the surface is smoother and clearer than it was before the annealing process.

Figure 4.21: PC tube after annealing for 72 hours at 175 °C .

Figure 4.22: PC tube after annealing for 6 hours at 175 °C .

The next step to test whether annealing can be used to help the thin 3D printed tubes become smoother was again conducted at 175 °C , as an improvement was seen previously, but for a shorter time. It could be that the material doesn't become smoother and more clear before it collapses, so I performed more tests to see at which stage the tube collapses. In Figure 4.22 the result after 6 hours at 175 °C is seen. In this case, the tube has collapsed, but is not smoother and does not appear to have less bubbles than before the treatment.

I attempted one more annealing test in order to achieve a smoother surface and annealed a printed tube at 125 °C, for an extended period of time, 72 hours. No change was seen in the tube. A summary of all the annealing tests performed on the 3D printed PC tubes and the results are shown in Table 4.3. These results did not allow me to identify processing conditions that would improve the surface quality without the structure collapsing.

## 4.6 Conclusions and Future work

This chapter reports the progress towards drawing fibres from low-cost preforms with readily available materials and fabrication facilities. The first trials on the printed polymer preform drawing quickly showed that there were more factors to be taken into account than initially considered. In order to improve our understanding of the drawing process of polymer-based thin tubes, a model is used to study the fluid dynamics for capillary drawing with Non-Newtonian capillaries. This model was tested and proved to be a reliable method to predict the capillary dimensions after drawing at a certain speed and temperature profile. It has also been shown that depending on the polymer the Non-Newtonian effects like shear-thinning can be ignored, simplifying the calculation by avoiding the need to work out the shear rate to be able to calculate the effective viscosity.

The air holes in the 3D printed structured posed a problem during the drawing process, but also the polymers itself proved more complex to draw into fibres than expected. Although some printed preforms were drawn into fibres, there were many variations along

Table 4.3: Overview of results for annealing of 3D printed PC tube

| **Temperature** | **30 minutes** | **6 hours** | **72 hours** |
|---|---|---|---|
| 125 °C | No change | | No change |
| 150 °C | No change | | |
| 175 °C | No change | Deformed | Collapsed and clearer material |
| 200 °C | Deformed | | |

the fibre, both in the structure inside as well as in the fibre's outer diameter, leading to an unreliable fibre.

To model the behaviour of polymers with significant shear-thinning in fibre drawing with complex fibre profiles, models that are already able to calculate the final profile for different fibre profiles would have to be adapted to include the effective viscosity depending on the temperature and shear-rate. The Power Law, as used in this model, has been shown to be an accurate approximation for the viscosity, and could be used to adapt other fluid-dynamics models to include shear-thinning/shear-thickening too.

As our experiments show that commercially sourced polymers have different material properties for different batches, it would be useful to analyse the raw materials before fibre drawing. To characterise the polymers Fourier Transform Infrared Spectroscopy analysis and Raman Spectroscopy could be used to compare the different batches. The viscoelastic properties of the polymers could be measured using thermal analysis [151]. It could also be helpful to characterise the viscosity as a function of temperature and stress, as this could improve the accuracy of the model used to predict the capillary drawing experiment.

Despite the various complications we experienced in drawing 3D printed preforms produced with our consumer-grade printer, we believe that future improvements could lead to 3D printed optical fibre preforms. Indeed, adopting a printing technique like SLS (described in Chapter 2 would produce preforms with smoother surfaces and no bubbles. The simulations have shown that the shear-thinning effect in PC is limited and should not affect the structure significantly.

As discussed in Chapter 2, the properties of HC fibres simply scale with the size of the waveguide. This inspired me to explore the use of 3D-printed antiresonant waveguides in regions of the spectrum where the wavelength is long and eliminates the requirement of a second drawing step on the fibre tower.Terahertz waveguides, for example, typically have larger dimensions and therefore can be directly printed without the need for further fibre drawing. In the next chapter I present my work in designing, fabricating a characterising waveguides for use in the terahertz regime.

# Chapter 5

# 3D Printed antiresonant terahertz waveguide

## 5.1 Introduction

In this chapter, I develop and test polymer HC waveguides with half elliptical cladding elements which I studied and described in Chapter 3 for the guidance of terahertz radiation. Terahertz waveguides allow for a terahertz pulse to be delivered to remote locations in environments which may be hostile or hazardous, and for efficient coupling between components such as emitters and detectors. Terahertz waveguides have been demonstrated for industrial monitoring of chemical reactions by measuring ammonium chloride aerosol by-products [152] as well as for probing pharmaceuticals such as aspirin [153].

Due to longer wavelengths in the terahertz regime compared to the visible/near infrared which has been the focus of previous chapters, there is no need for a drawing process in the draw tower and the printed waveguides can be used directly from the 3D printer. The waveguide described in this chapter is printed using PC, which has been shown to have low-losses in the terahertz spectral range (as seen in Figure 2.14.The transmission loss is characterized and a comparison between the numerically expected loss and the measurements is conducted. Since the loss through the waveguides was found to be higher than expected from models, a more detailed study into the effect of the ribbed structure on the transmission is performed. From this study, it became clear that the waveguide's performance could be improved by finding ways to remove or reduce the ribbed pattern on the 3D printed waveguides.

## 5.2 3D printed waveguide

### 5.2.1 Design and Material choices

As discussed in Chapter 2, using the FDM printer to fabricate waveguides can significantly reduce the production time and costs and since FDM printers are commercially available this fabrication method is easily accessibly to any lab at very accessible cost. The low-cost and ease of fabrication makes it possible to design multiple waveguides to test and compare their behaviour with the predictions from simulations. From the different polymers discussed in Chapter 2, I chose PC for the fabrication for these waveguides as it has the lowest loss compared to the other available polymers for 3D printing.

As the smallest feature size of the particular FDM printer I used is 0.6 millimetre, this thickness is chosen for the cladding elements in the initial design, using 6 half ellipses. The waveguide is optimised using a core radius of 5 millimetres. To minimise the loss a major-axis of the ellipse of 5 millimetres is found to give the lowest loss, with a curvature of 2.2.

To test the behaviour of the designed waveguide, two additional waveguides are fabricated, with the designs shown in Figure 5.1. Waveguide A has an identical design as the optimised waveguide described above, but smaller dimensions. The core size is 3 millimetres and the major-axis of the ellipse is also 3 millimetres. This should result in increased attenuation, as loss in these waveguides is dominated by the leakage contribution which scales with the core size approximately as $\frac{\lambda^4}{r^5}$ [41; 105]. The optimum design mentioned above is waveguide B, as it has the largest core size and the thinnest membrane size. Waveguide C is the same size as waveguide B, but the thickness of the membranes in the cladding is double the thickness of the membrane in waveguide B, which increases the number of resonances in the same spectral range, see Equation 3.21. Six half-ellipses are used in each hollow-core waveguide, with a single layer thickness of 0.6 millimetre for waveguide A and B, and 1.2 millimetre for waveguide C. In Table 5.1 an overview of the design parameters is shown for each waveguide.

TABLE 5.1: Parameters for designed waveguides as shown in Figure 5.1

| | **Thickness (t)** | **Core size (r)** | **Ellipse length (l)** |
|---|---|---|---|
| A | 0.6mm | 3mm | 3mm |
| B | 0.6mm | 5mm | 5mm |
| C | 1.2mm | 5mm | 5mm |

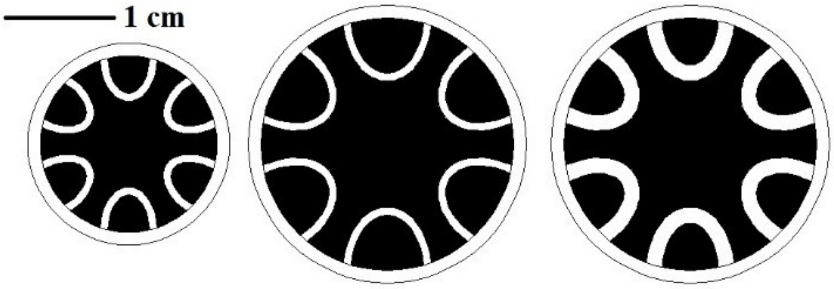

Figure 5.1: All three waveguide designs shown on scale. Left to right: waveguide A, waveguide B and waveguide C.

As discussed in Chapter 2, there are different polymers to choose from when fabrication a terahertz waveguide. However, in antiresonant waveguides, the bulk loss of the material is less important for the design, as only a small fraction of the power propagates into the polymer cladding. It is thus more important to take into account the feasibility of printing the design in a specific material, and for this reason I chose PC to fabricate the waveguides [90; 20]. For PC the refractive index in the terahertz range is 1.6 [154] and the loss is 17 dB/cm at 0.3 THz as shown in Figure 2.14. The loss in each waveguide is calculated for frequencies between 0.05 and 0.6 terahertz using the same model described in Chapter 3. The results for these simulations are shown in Figure 5.2. In waveguide B it can be seen that in the antiresonance regions the loss reaches minima that are over 2500 times lower than the material loss [90], showing that this type of waveguide could be suitable for terahertz guidance. The antiresonance frequencies could be shifted by changing the thickness of the membranes depending on the specific requirements of the waveguide and its application. A different nozzle for the FDM printer (or a different printing method) would need to be used in order to achieve this, as the UP printer only has one printing nozzle. The thickness of the extruded filament varies slightly depending on the material, temperature and printing speed used.

The production time of waveguide B is less than an hour for a waveguide length of 9 centimetres. Waveguide A is produced even quicker, but waveguide C takes nearly two hours due to the double layer in the cladding element. The material cost for each waveguide is also low. The PC filament can be bought from different suppliers, but on average a spool with 300 grams of PC can be bought for less than £20. Waveguide B weighs just under 15 grams (including the printed support layers that are removed before using the waveguide), bringing the total material cost for the waveguide to less than £1, therefore this is an extremely cost-effective method to replace expensive terahertz components, such as the 3D printed components described in Chapter 2.

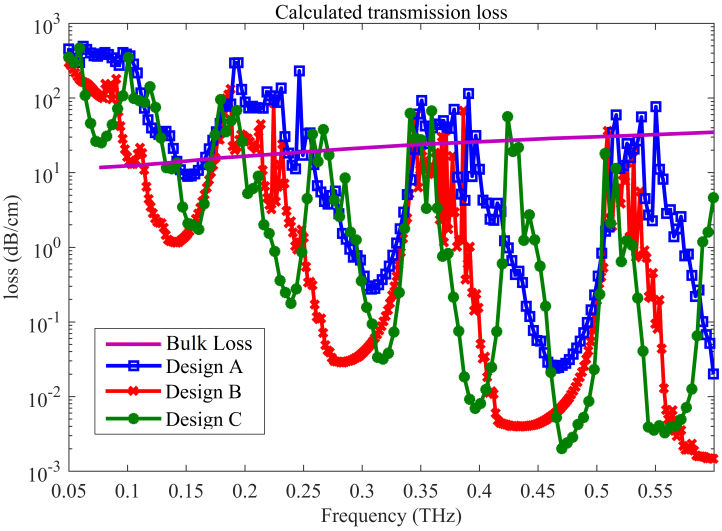

FIGURE 5.2: Simulation results for transmission loss for all three waveguides compared to the bulk loss of Polycarbonate.

### 5.2.2 Measurement set-up experimental results

To measure the transmission through the waveguide, a suitable terahertz spectroscopy set-up has to be found. I identified a terahertz group in the physics department, the Terahertz Laboratories, who were very keen to collaborate, and instigated a collaboration. The measurements for the transmission and loss calculation in this chapter are performed by J. Gorecki. The terahertz spectroscopy set-up used for the transmission measurements was initially developed for material characterization. The original terahertz time domain spectrometer (THz-TDS) set-up is shown in Figure 5.3a. In this spectroscopy set-up, the electromagnetic radiation is measured as a function of time instead of as a function of frequency. As a result, a Fast Fourier Transform (FFT) has to be used to obtain the frequency domain spectrum. The terahertz emitter is Tera-SED from Laser Quantum GMBH, a GaAs photo-conductive emitter that emits broadband terahertz waves up to 2.5 THz [155]. The detector used is a Menlo GMBH TERA8-1 photo-conductive antenna [156] that has a bandwidth of up to 4 THz. Although the emitter and detector are active up to 2.5 THz and 4 THz respectively the spectroscopic bandwidth is limited by ambient noise and component alignment, the latter having greater effect at higher frequencies. The resultant effective bandwidth over which useful spectroscopic data can be obtained is in the range of 0.1 THz to 1.0 THz. The object to test is put in the focus of the terahertz beam and the output is collected on the detector. Two measurements are taken, one with the testing object in the set-up and one reference scan without an object present. The transmission spectrum is then calculated by normalising the scan with the testing object using the reference scan.

We performed this same measurement by inserting the 3D printed waveguide as the object in the set-up. The 3D printed waveguides A, B and C are printed to a length of 8.7 centimetres in length and the measurement is repeated three times. The results for this measurement is shown in Figure 5.4. Each measurement is normalised by dividing the measured transmission by the reference transmission. For each measurement, the waveguide is placed into the set-up separately, which I believe is the cause of the differences between the different measurements as the alignment of the waveguide can be difficult. It can also be seen that there are no distinct antiresonance peaks in the transmission spectrum, which were expected from the calculations as shown in 5.2.

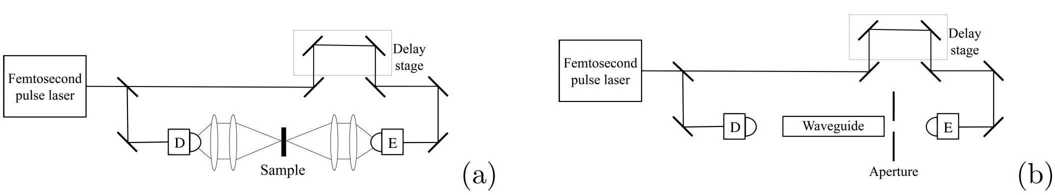

Original THz-TDS set-up used for material characterisation.

Adapted THz-TDS set-up used for waveguide characterisation.

Figure 5.3: Original and adapted THz-TDS set-up used for characterisation of waveguides in this chapter.

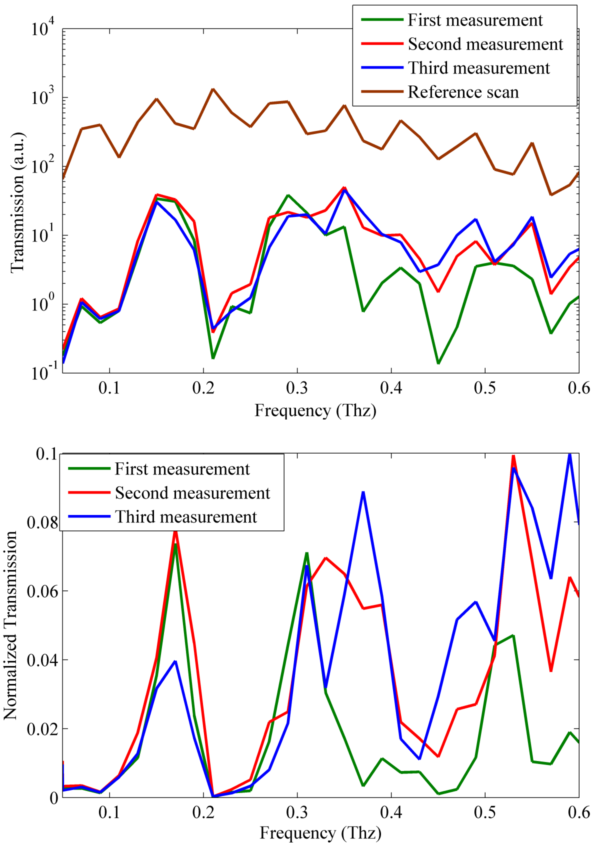

Figure 5.4: (top) FFT of measured signals for reference and three different scans for waveguide B using original THz-TDS set-up as shown in Figure 5.3a. (bottom) Three different transmission measurements for waveguide B normalised using reference scan.

One potential cause of this problem could be the alignment between the waveguide, terahertz source and lenses system used to couple the focused beam into the waveguide. As the waveguide is placed into the set-up, its position depends on the quality of the alignment. If the waveguide is tilted slightly, this leads to changes in the coupling between the beam and waveguide. A small deviation of 1 degree would lead to a shift of 1.6 millimetres in the position of the core of the waveguide. To negotiate the difficulty in aligning the waveguides, metal disks to hold the waveguide in place on the optical rail are fabricated and held in clamps. Using these clamps and disks stabilises the position of the core of the waveguide with respect to the incoming beam, with less changes in the waveguide's position when the waveguide is placed in the set-up repeatedly. The metal disks also function as an aperture to only allow the beam into the core of the waveguide. An image of the clamps used is shown in Figure 5.5. The waveguide is glued onto the metal disk with the core overlapping with the aperture. However, using this method did not improve the reliability of the results when the measurement was repeated using the same set-up. As the spectroscopy set-up is not usually used for transmission measurements, we decided to modify the set-up in order to simplify the coupling into the waveguide, as will be described in the next section.

#### 5.2.2.1 Characterisation of waveguide guidance

To facilitate alignment and improve the reliability of the measurements, we explore two other methods of measuring the waveguides transmission. The first was to put the waveguide into a collimated beam, with an aperture blocking the part of the beam that does not overlap with the core. The second was to use no lenses at either side. This

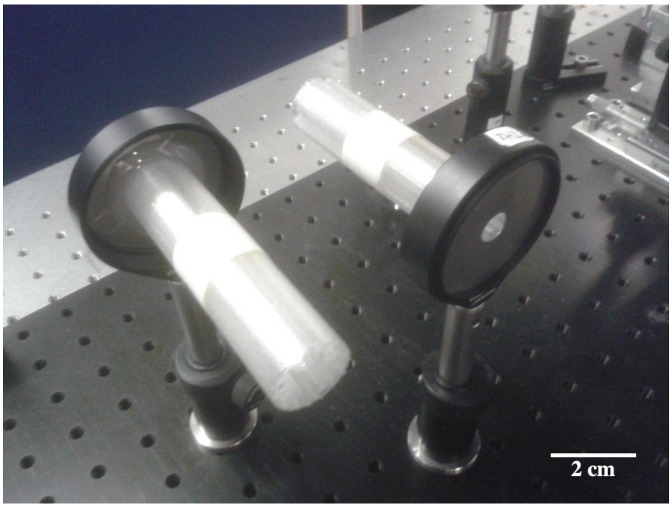

Figure 5.5: Metal disks fabricated to hold waveguides aligned in THz spectroscopy set-up, with the aperture the same size of the core of the waveguide.

arrangement facilitates the characterisation of the waveguides ability to guide THz radiation without the complex and difficult procedure to align lens systems.

In Figure 5.6 the normalised transmission results when using a collimated beam are shown. The results are normalised using a reference scan, where the waveguide is not present in the set-up. It can be seen that in this case the waveguide is not very effective, as almost all the frequencies transmitted show a relative transmission of less than one, which means the transmission is lower when the waveguide is present in the set-up. We therefore repeated the experiment without input and output lenses. The set-up for this experiment is shown in Figure 5.3b. In this set-up we tried to minimise the distance between the waveguide and detector/emitter, so that at both ends of the waveguide we had about a 6 mm gap. As can be seen in Figure 5.7, we could now see spectral regions with a transmission higher than 1, showing that the waveguide is more effective than free space guiding, without the need for complex lenses systems. The antiresonances are also clearly visible for waveguide A and B, though they are less clear for waveguide C. This is potentially due to the way the double layer in the waveguide is printed, as from what we have seen in Chapter 4 there are air-gaps between the two layers which can cause the waveguide to behave differently than expected from the calculations. Another potential cause is that the air gaps might be affecting the thickness of the membranes in the cladding and thus shifting the antiresonant regions. A direct conclusion from this experimental study is therefore that when designing a antiresonant waveguide for different frequency ranges, one will need to alter the nozzle size in order to tailor the position of the antiresonance frequencies.

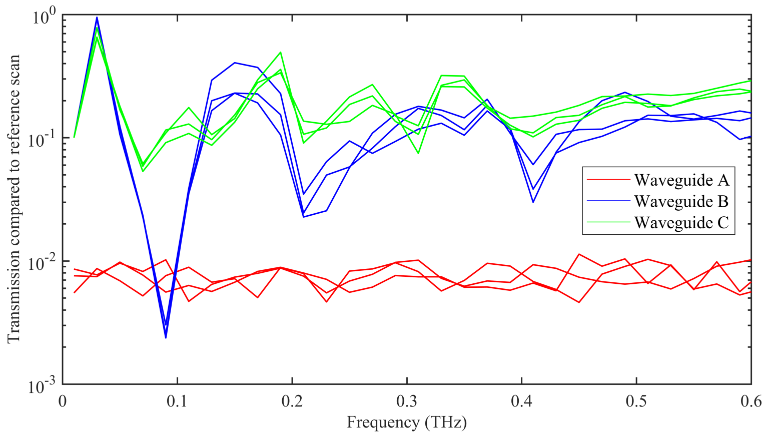

Figure 5.6: Transmission results for all three waveguides with collimated beam as input.

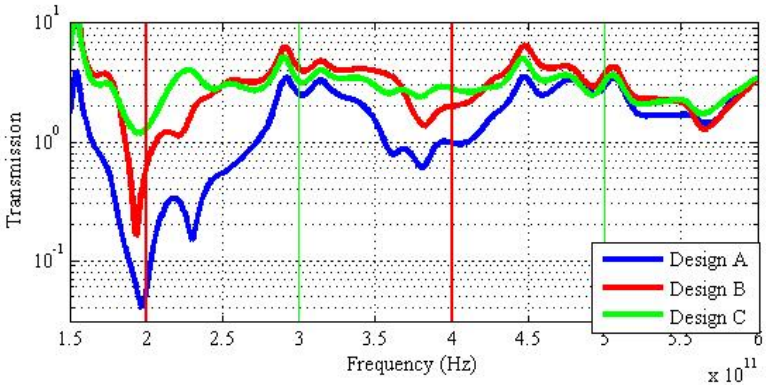

FIGURE 5.7: Transmission measured for each waveguide. The transmission is normalised using a reference scan without a waveguide in the set-up as shown in Figure 5.3b. Red vertical lines indicate expected resonances (high loss, transmission dips) for all three waveguides, green lines indicate additional expected resonances for waveguide C.

#### 5.2.2.2 Loss measurement

Although transmission measurements are commonly used to characterise materials in THz-TDS, a more conventional way of characterizing a waveguide is a loss measurement. In fibre optics, a loss measurement is usually performed using the cut-back method. In this approach a long length of the fibre is used in the set-up and the output power is measured. The fibre does not get removed from the set-up, and the input coupling end in the set-up does not change. A long piece of fibre is cut-off, and the output power is then measured on the remaining short piece of fibre. The difference between these two measurements provides the transmission loss. When this method was used for the waveguides described in this chapter, it became clear the cutting of the waveguide would be a problem. The only way of cutting the waveguide would be to use a saw, which would create a rough surface that could lead to scattering. Debris from such a cutting process in the waveguide after the cutting could also effect the measurement. To work around these challenges, three different lengths of waveguide are fabricated and studied. Multiple scans for each waveguide length are taken to average out discrepancies due to coupling differences.

As waveguide B has the best performance, this waveguide is used for the loss characterization. Three different lengths of waveguide B are printed: 8.6, 6.6 and 3.9 cm. The waveguides are all aligned using the clamps as shown in Figure 5.5 and five scans are taken for each waveguide. The comparison between the calculated and measured average loss can be seen in Figure 5.8.

It can be seen that there are two antiresonance windows near the expected spectral position at 0.3 THz and 0.45 THz, where the loss is up to ten times lower than the bulk loss. This is a good result in itself, however, the measured loss is still considerably higher than predicted from the simulations. The most likely explanation in my view is that the incoming beam suffers from scattering from the rough surfaces in the 3D printed waveguide [157], which was not taken into account in the simulations. The surfaces of the tubes are considerably rougher in FDM printed samples than for other 3D printing methods, due to the layer thickness of 0.1-0.4 millimetre, as already explained in Chapter 4. The extruded filament is circular and gets distributed on top of a previously printed layer of filament, which is also circular. As a result, the vertical surface along the printed object has a ribbed effect and is not smooth. The impact of this ribbed surface needs to be studied in more detail to determine whether it can be an explanation for the discrepancy between the calculated and measured loss.

To use the waveguide for terahertz spectroscopy, it is also useful to know the spot radius of the output beam from the waveguide. To determine the output beam of the waveguide, a free space simulation is performed for the mode at the end of the waveguide [158]. The result of this simulation is compared with the beam profile measured 6 mm behind the waveguide using a knife-edge measurement. The knife-edge measurement is done with the same emitter and detector, but the beam after the knife-edge is focussed on the detector using two lenses. The beamwidth is extracted from the measurements and a corresponding Gaussian for the beam profile is calculated. It can be seen in Figure 5.9 that the calculated and measured beams are very similar, with 15% deviation in the beamwidth. The discrepancy can be explained by the fitting of the Gaussian beam and the error function to the data. An error of roughly 10% existed in the calculation of the beamwidth, corresponding to a beam diameter of 9.2 ± 0.9 mm. Although the beam is assumed to be Gaussian, there is probably a small deviation between a Gaussian beam and the output beam from the waveguide. Using this beam profile to calculate the mode propagation in free space, it can be seen from Figure 5.9 that the beam is divergent. However, the simulated divergence angle is 3.4°, which is small enough to allow experiments to be conducted in the proximity of the waveguide tip without need of any further lenses. To obtain a collimated beam, a combination of lenses needs to be used. However, due to the increase in transmission compared to free space propagation,

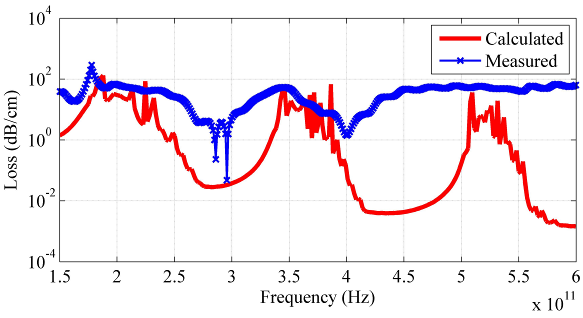

Figure 5.8: Calculated loss and measured loss for waveguide B compared.

the 3D printed AR waveguide could be beneficial to use for terahertz transmission.

## 5.3 Wave propagation simulations

It can be seen from Figure 5.8 the loss in the waveguide is higher than expected from the simulations. In the simulations, the structure of the surface of the 3D printed waveguide was not taken into account. As the FDM printer layers the filament on top of each previous layer, the surface that results from this is not smooth, but ribbed as described in Chapter 4. If the layer height setting of the printer is set to a higher setting, it leads to a more pronounced ribbed pattern on the printed waveguide.

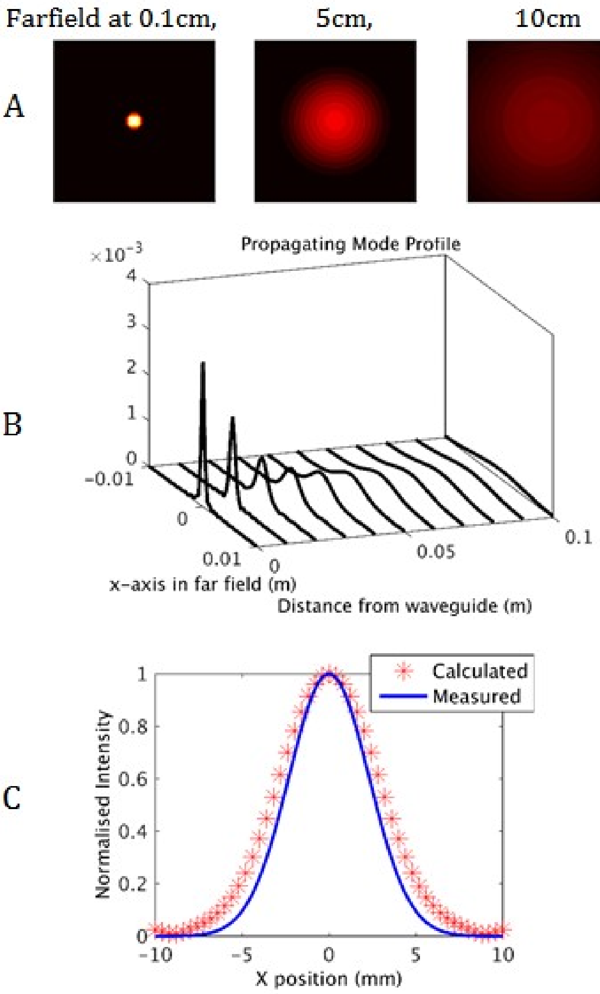

FIGURE 5.9: (a) Calculated THz mode profile at different positions in the far field. (b) Mode profile propagating in free space at 0.32 THz. (c) Measured beam shape at 0.32 THz compared to calculated beam shape at 0.32 THz 6 mm behind the waveguide.

To study the impact of this ribbed pattern on the propagation in more detail, I simulated the propagation in a 2D waveguide using the wave optics package of COMSOL. For simplicity, I study a simple 2D structure where the core consists of air and the cladding is made of two thin rectangles. I compare this with a similar sized waveguide where the cladding has a ribbed pattern on the boundary as if it was 3D printed. In Figure 5.10 the two waveguide structures are shown. The waveguides studied using this simulation are tubes with a diameter of 1 cm and a wall thickness of 1 mm. The diameter of the waveguide studied are similar to the core dimensions of the waveguide from the previous section. To study the effect of the ribbed pattern, I simulate a worst case scenario. The ribbed pattern from the 3D printer used in this project has a variation of 0.6 mm, so I rounded this to 1 mm to study the effect of the ribbed pattern. In the terahertz regime, wavelengths of 0.6 mm-1 mm correspond with frequencies between 0.3 and 0.5THz, which is the part of the spectrum used to analyse the waveguides. The pattern of the ribbed structure of the waveguide used for the simulation is sinusoidal.

To propagate light through both of these waveguides, a port is added on each end of the waveguide. One port functions to couple the light into the waveguide, the other port can be used to read the output power. In Figure 5.11 the transmission at 0.3THz is shown. This frequency corresponds to a wavelength of 1 mm, the same as the variation on the boundary. It can easily be seen that the ribbed pattern leads to more reflections and scattering in the structure, thereby increasing its attenuation. In Figure 5.12 the normalised amplitude of the power along the length of the two waveguides is shown. It can be seen that the power in both waveguides decays with an increasing waveguide length, but for the ribbed waveguide the decay is faster, which shows that there is an increase in the attenuation as a result of the ribbed pattern.

The increase in loss can also be seen when studying the transmission through the waveguides over a range of frequencies. Using the output port of the waveguide in COMSOL, the transmission can be calculated by evaluating the S21 parameter [118; 159]. The frequency domain studied is 0.1-0.6THz, the same as the experimentally studied domain in the previous section. In Figure 5.13 the transmission through each waveguide is shown.

It can be seen from these transmission spectra that the transmission is reduced due to the ribbed surface, even in a short waveguide of only 4.5 cm. Although the reduced transmission through the 3D printed waveguide can not quantitatively be compared to the transmission penalty shown in Figure 5.13 due to the ribbed pattern, these results indicate that the ribbed pattern on the boundary of the waveguide has a negative impact on the transmission. The 3D printed waveguide for the terahertz regime could be improved if a method was found to avoid the ribbed pattern on the surface. In Chapter 4 I described how I attempted to use annealing as a way of smoothing the surface, however

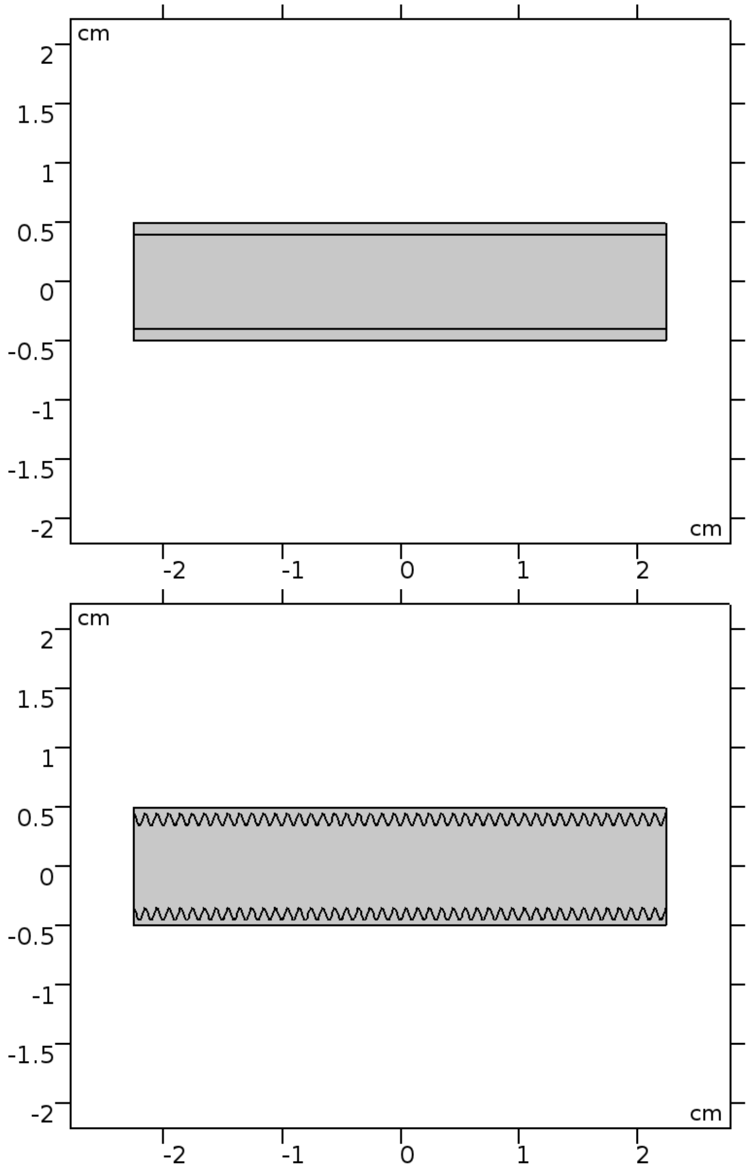

Figure 5.10: The geometric model for the two waveguides to study the effect of the ribbed pattern on the waveguide.

this unfortunately did not work on the 3D printed PC tubes. As discussed in Chapter 2, other 3D printing methods could be used to achieve smoother surfaces, although the cost of the printer and material will likely be higher. Other options to achieve a smoother surface could include chemical treatment to the polymer waveguide.

## 5.4 Conclusions

In this chapter I have shown the design and fabrication process of a 3D printed antiresonant waveguide for the terahertz regime. The waveguide, made of commercially

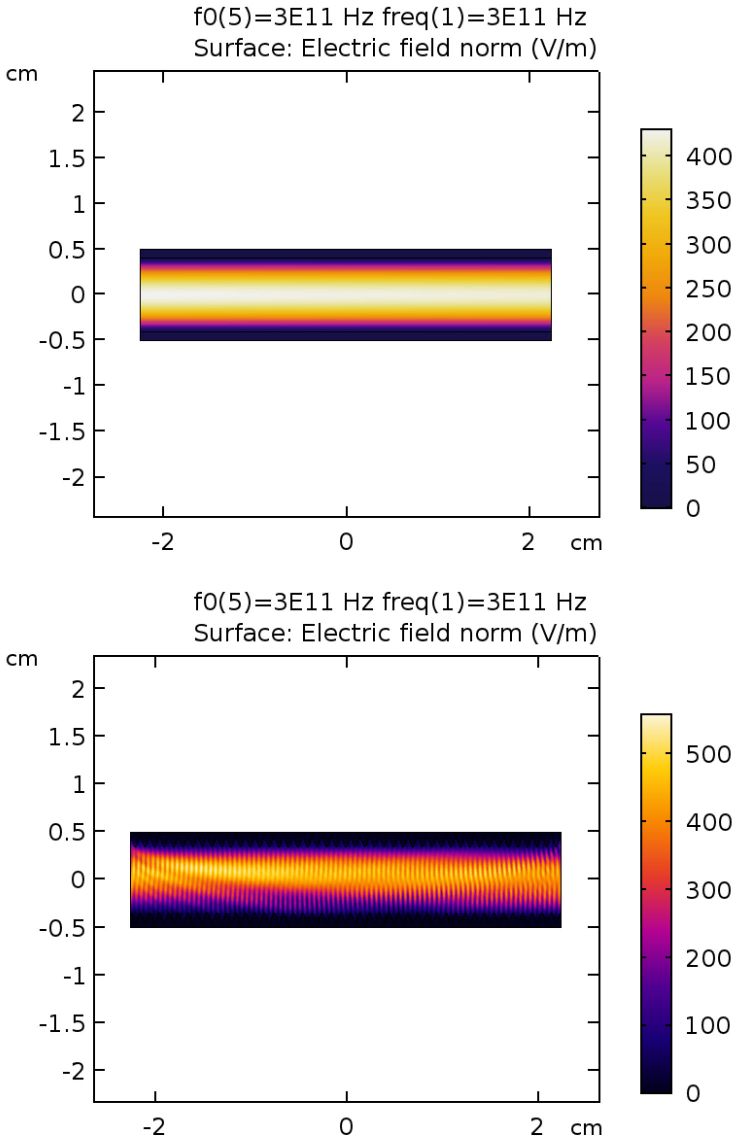

Figure 5.11: Wave propagation through smooth waveguide (top) and ribbed waveguide (bottom) at 0.3THz.

available PC, can be used to guide in the antiresonant regions without the need for complicated lens systems to focus and collimate the beam. The guiding of the short AR waveguide (up to 10cm) could be used in a variety of different table-top terahertz spectroscopy set-ups instead of the lens system which is currently needed to collimate and focus the terahertz beam. Because the waveguides are hollow they could also be used for gas spectroscopy with a species introduced in the fibre.

Although the fabrication time depends on the 3D printer used, 3D printing is a rapid and cost-effective way to fabricate a short-range terahertz waveguide. A different thickness of the cladding elements could be used to change the antiresonance frequencies to

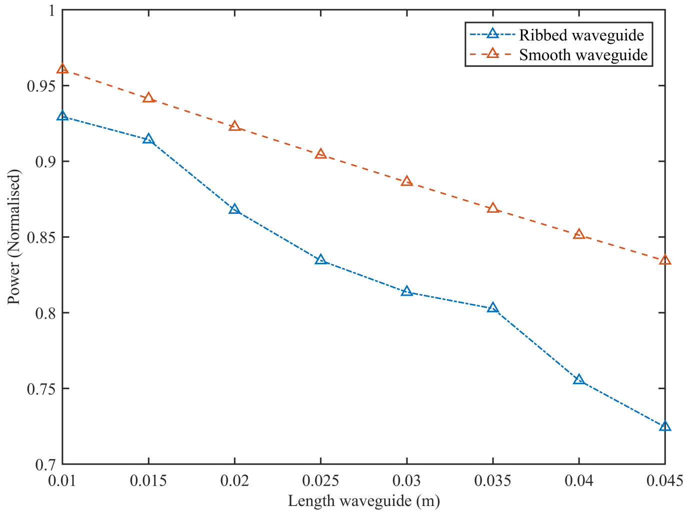

FIGURE 5.12: Normalised power along the two simulated waveguides at 0.3THz.

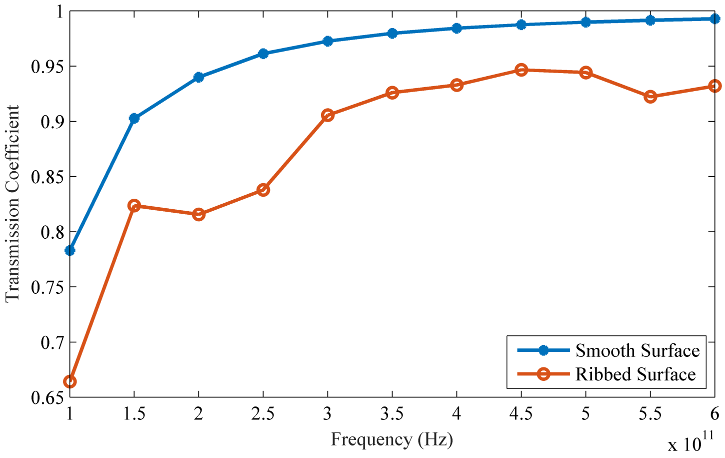

FIGURE 5.13: Calculated transmission through smooth waveguide and ribbed waveguide.

cater for different applications for the waveguides, though a different 3D printer with adjustable nozzle sizes would be required to achieve this. Different HC waveguide designs could also be produced using the FDM printer, as long as the minimum feature size does not exceed the nozzle size used.

The waveguide fabricated in this chapter could further be improved by looking into ways of smoothing the surfaces of the waveguide, as the ribbing on the surface of the waveguide leads to higher losses compared to a smooth surface. Potential options to achieve this include chemical treatment, or using a different printer that can achieve smoother surfaces. Other polymers with lower transmission loss in the terahertz regime like Topas could also be used. Although improvements could certainly be made, this inexpensive waveguide has already improved the transmission compared to the bulk loss and could be used for transmission in the antiresonance regions.

# Chapter 6

# Conclusions

## 6.1 Overview

Hollow core optical fibres are an exciting technology that offers many benefits over conventional fibres due to the fact that more than 99.9% of the light is being guided in air. In one of the most promising types of HC fibres, called antiresonant hollow core fibre (ARF), light is guided in the core of the fibre thanks to antiresonances from thin membranes disposed around it. Current ARFs are typically fabricated by stacking cylindrical capillaries, which restricts considerably the range and topology of transverse HC fibres that one can achieve. A considerably greater degree of freedom would be achieved if preforms could be fabricated by 3D printing or additive manufacturing. 3D printing is a fast expanding manufacturing technique to produce three dimensional objects of various materials from CAD computer models. In this project, I have investigated the feasibility of using 3D printing as a technique to produce hollow core fibre preforms of arbitrary inner shape. Given the fact that 3D printing of ceramic/glass materials is still in its infancy, I have focused my project on polymer based materials. The rationale was that a large number of polymers can already be 3D printed using widely available consumer grade machines, and the findings of this work could be applied to 3D printing of glass preforms, once glass 3D printing technology will become available.

At the beginning of the project, I have explored different ARF types in order to find a design that was 1) suitable for manufacturing via 3D printing and 2) that provided a low propagation loss. After assessing many possible alternatives, I have decided to focus my study on ARFs with half-elliptical cladding elements. This particular design was chosen not only for its ease of fabrication with 3D printing methods, but because it also enabled the study of the effect of the curvature of the ellipses on the propagation loss in the fibre. It was thus important to find a way of varying the curvature whilst affecting as little as possible the other parameters. In order to do this, I chose to vary the number of semi-elliptical elements, while keeping constant the distance between the half ellipses, the core size and fibre size. As a result, the curvature is lower when fewer cladding elements are present and it increases when the number of cladding elements is increased.

A large number of finite element method simulations have been performed to compare different fibres with half-elliptical cladding elements. One of the main conclusions of this study was that an optimum curvature of these core surrounding membranes appears to exist at which the loss is at its minimum. The loss of a fibre can be reduced by utilising this optimum curvature in the design. At curvatures above the optimum value, total internal reflection occurs in the cladding membranes; below the optimum curvature value I found evidence of more leakage through the elliptical elements, leading to a fibre with a higher total leakage loss than the optimum curvature would have. Several different fibre designs were tested for this project, showing that the optimum curvature was in the range of 2-2.5 for each of these cases.

A similar dependence of loss on the curvature of the thin membranes is also seen in ARFs with full rather than half ellipses. Full ellipses however would take up more space in the fibre, and as a result this would lead to a smaller core size in a fibre with the same outer diameter, or in a fibre with a larger outer diameter if the core size is kept unchanged. A preform with full ellipses in the cladding could potentially also be more complex to draw into a fibre, as the cladding elements can easily tilt during the stretching process, which would not happen with half ellipses due to the presence of two anchoring points.

I then moved on to study the feasibility of using 3D printing techniques to manufacture the optimum designs I had developed. Different types of printers have been compared and based on costs and availability an FDM printer was chosen. FDM printers are commercially widely available, and there are several polymers that can be commercially sourced and printed using this technique. The printer used in this project, the UP! printer, had a fixed nozzle size, and therefore the layer thickness it could produce was limited to a multiple number of the nozzle size. For the ARF preforms designed, this meant that the preform size would have to be chosen such that the final thickness of the cladding elements would correspond to the calculated thickness needed to achieve antiresonance at the wavelengths the fibre is supposed to operate best.

Throughout the project, I have experimented with different polymers for the production of preforms and fibres. ABS and PLA, the most commonly printed polymers using FDM printers, are not the best option available for the fabrication of optical grade fibres or waveguides as they are totally opaque to light. Therefore, after an initial set of tests with these two materials, I focused on more transparent polymers, like the commercially available PMMA and PC, the transparency of which is much better than that of ABS and PLA in both the visible and the terahertz regime.

Several preforms were 3D printed from various polymers and according to different designs. After the first few fibre drawing trials of these printed preforms however, it became clear that the preform quality directly affected the effectiveness and reliability of the fibre drawing process. Due to the inherent layered structure of FDM printing and the imperfections in the printing process, gaps and bubbles ended up being incorporated in the preform, leading to problems during the fibre drawing process. We therefore momentarily stepped back and tested the drawing process of commercially purchased rods. These tests indicated evident differences in drawing behaviour between polymer and glass. The known Non-Newtonian behaviour of polymers seemed to play a non-negligible role in the fibre drawing dynamics.

To understand the differences between the draw of non-Newtonian polymers as compared to Newtonian glasses, a fluids dynamics model was developed to study the Non-Newtonian shear-thinning effect when drawing PC and PMMA. The model I developed is an extension of Fitt's original model that studies the fluid's behaviour for the draw of Newtonian capillary tubes. Here I added a numerical routine to take into account the effective viscosity, which for Non-Newtonian shear thinning or thickening materials is a function of the shear stress applied locally. To calculate the effective viscosity for polymers during the stretching process I used a simple but adequately accurate Power-law equation. The model, which I fully coded in Python, was used to study the effect of variation in speed and temperature when drawing PC and PMMA tubes. It was tested and validated through comparison with experimentally drawn tubes, and found to be a reliable method to predict the behaviour of a polymer tube in the drawing tower. This study indicated that shear thinning effects in polymers are non-negligible and in general tend to make the fabrication of fibres with thin membranes more complicated than in glass. It was also found that some polymers have stronger shear-thinning effects than others. For example, in the tube drawing experiment as shown in Chapter 4, the shear-thinning effect in PC was not as significant as for PMMA, and therefore that PC would be a preferable material for ARF fabrication.

Further analysis of the fabrication process indicated that gaps present between the printed layers caused difficulties with effective pressurisation during the fibre draw. As these gaps cannot be avoided with the FDM printer, I studied extensively ways to remove them after the 3D print phase, for example by heating-based annealing and out-gassing phases. The conclusion was unfortunately that in order for these bubbles to be removed, the polymer had to be heated at temperatures well above its glass transition temperature, typically too high for the structure to be retained. I therefore decided that it would be too challenging to try and achieve good quality ARF polymer fibres from a 3D printed preform fabricated with the UP! Printer. Despite a somewhat negative conclusion on this part of the project, the investigation has produced valuable knowledge that can be used, in future works, to improve the 3D printing of drawable optical quality fibre preforms.

At this point, I decided to explore ways of utilising the FDM printer for optical devices that did not need a subsequent fibre drawing process. Hollow core waveguides for the terahertz regime, for example, require a larger core size due to the longer wavelength, and therefore can be directly 3D printed. To be able to test the design with half ellipses in the cladding, a waveguide with a design optimised for guidance in the terahertz regime was printed using the FDM printer in PC.

To test the performance of this device, I initiated a collaboration with a terahertz research group in the Physics Department. The PC-based hollow waveguide with half ellipses showed experimentally an effective guidance at terahertz frequencies, and proved to be a useful tool in my colleagues set-up. The waveguide had up to ten times higher transmission compared to free space and a loss ten times lower than in the bulk material. Although there is clearly still scope to improve on these initial results, these values already make the waveguide a worthy addition in many terahertz experimental set-ups. I then studied in more detail the loss of this 3D printed hollow core waveguide. This was found to be higher than expected from the numerical studies. Modelling indicated that the most likely causes for this discrepancy were the longitudinal imperfections in the waveguide and the ribbed structure arising from the 3D printer. To improve the surface quality, I attempted annealing the waveguide, but this was not found to be effective at removing the ribbed structure from the surface. If the performance obtained in this work are already adequate for a particular terahertz experiment, this work opens up the possibility any THz group to quickly and cheaply fabricate useful terahertz waveguides with antiresonant designs to improve their own set-ups, using commercially available materials and equipment. For improved waveguide performance, different types of 3D printers will need to be investigated in future works.

## 6.2 Future work

Several improvements to the work presented in this thesis could be made to enable the use of 3D printers to fabricate ARF preforms for fibre production, as well as improvements that could enhance the performance of the 3D printed terahertz waveguides.

To improve the terahertz waveguide, other printer types could be used to achieve a smoother surface, which should lead to lower leakage loss through the waveguide as the ribbed structure on the surface of the waveguide should be reduced. Some of the alternative printing techniques discussed in Chapter 2 such as SLS printing might be able to achieve this, although this would come at a somewhat higher purchasing and running cost. The resin and powders used are generally speaking more expensive than the filament used in this project, however this might also mean the material purity is improved and the printed objects could therefore have a better optical performance as a result. Alternatively, chemical post-treatment of the preform could be another route towards reducing the surface roughness.

Different printing methods should also be considered for the fabrication of printed preforms for fibre drawing. The FDM printer used in this project appears unsuitable due to the many holes and air gaps it creates in the printed object, which caused problems during the drawing process. Other 3D different printing methods could create a solid preform without these imperfections that potentially could be drawn into fibre.

To aid the fibre drawing of these preforms, the model discussed in Chapter 4, which simulates the behaviour of polymer capillary drawing would have to be extended to include more complex structures. This type of simulations have already been performed for Newtonian materials [74], which could likely be used as an approximation for PC as the shear-thinning effects in this polymer are minor, but would not be adequate for polymers such as PMMA where the shear-thinning is more significant.

To improve the fabrication, it could also be helpful to study the polymers' properties in more detail for each polymer used for fabrication. For example, Fourier Transform Infrared spectroscopy analysis and Raman spectroscopy could be used to compare the composition of different polymer samples. Thermal analysis experiments could be utilised to measure a range of properties in polymers, such as the viscoelastic properties [151]. To aid improvements in both the fabrication as well as the fluid dynamics model's accuracy viscosity measurements would also be beneficial, as a function of temperature and as a function of stress. The material properties found in these tests could potentially help identify the difficulties found with drawing these polymers after 3D printing.

Besides improvements that could be made on the fabrication of polymer preforms, there is also a possibility to take 3D printing further and print optically clear glasses, as already demonstrated in a very preliminary study [12]. Improvements in the size of the 3D printed objects would be needed, but if successful this would open up a very interesting opportunity to reproducibly fabricate ARF preforms of arbitrary topology.

# Appendices

# Appendix A

# Python model for Non-Newtonian Capillary drawing

## A.1 Model

Python model used for PC and PMMA with parameters as shown in Table 4.2.

---

### Models

---

```
from matplotlib import pyplot as plt
from numpy import linspace, sqrt, exp, log, isnan


class Fitt_solver:
    def __init__(self):
        self.size = #number of data points
        self.xmax= #length of fibre studied (in hotzone)
        self.dx = self.xmax/(self.size-1)
        self.fidg=0.01
        self.count=0

        self.ID = #initial ID of tube
        self.OD = #initial OD of tube
        self.mu = #viscosity at room T
        self.g = 9.8
```

```
        self.sig = #boltzman constant

        self.gam = #surface tension
        self.a = #emissivity constant
        self.rho = #density
        self.cp = #specific heat
        self.Tglass= #Tg for material (in K)

        self.Ta= #maximum temperature of furnace (in K)
        self.Troom= #room temperature  (in K)
        self.p0= #pressure
        self.Uf= #Feeding speed (m/s)
        self.Ud= #Drawing speed (m/s)

        self.dmudz=[0]

        self.max=0.006
        self.guess= #guess value for dudx
        self.shootpart=10**-8
        self.guess2=self.guess+0.0003
        self.du=self.guess
        self.dy = [self.guess]
        self.Tstart=273+180
        self.T=[self.Tstart]
        self.Tgaus=[self.Tstart]
        self.mu_cold=4*10**13*exp(-0.046*self.Tstart)
        self.mu=[self.mu_cold]
        self.mu_newt=[self.mu_cold]

        self.h1=[self.ID]
        self.h2=[self.OD]
        self.maxit =10000
        self.criterion=0.01
        self.counter=0
        self.m=[]
        self.x=linspace(0,self.xmax,self.size)
        self.y = [self.Uf]
        self.fi=[]
        self.currentX=0
        self.Adu=[self.guess]
        self.shears=[0,0,0,0,0,0]
```

```
     self.step()

 def step(self):
     self.du=self.guess
     self.dy = [self.guess]
     for j in range(self.maxit):
         if len(self.x)!=len(self.y):
             for i in range(self.size-1):
                 self.d2udx2()
                 self.tempX=self.x[i]
                 self.Tgauss()
                 if self.T[-1]>self.Tglass:
                     self.y.append(self.y[-1]+self.dx*(
self.dy[-1]+self.dx*\

self.d2udx22))

                     self.h1.append(self.h1[-1]+self.
dh1dx*self.dx)
                     self.h2.append(self.h2[-1]+self.
dh2dx*self.dx)
                     self.dy.append(((self.y[-1] - self.y
[-2]) /
                                     (self.x[-1]-self.x
[-2])))
                 else:
                     self.y.append(self.y[-1])
                     self.h1.append(self.h1[-1])
                     self.h2.append(self.h2[-1])
                     self.dy.append(self.dy[-1])

         if len(self.x)==len(self.y):

             if self.checkifdone():
                 print(len(self.shears))
                 self.plot()
                 self.muplot()
                 print('Solution found')
                 print(self.h1[-1],self.h2[-1])
                 print(self.Adu[-1])
                 break
```

```
            print(self.y[-1]-self.Ud, self.Adu[-1])

            self.shoot()
            if isnan(self.y[-1])==True:
                self.Adu.append(self.Adu[-2]*1.01)
                print('NaN element - the solution does
not converge')

            self.du = self.Adu[-1]
            self.dy=[self.du]
            self.y=self.y[:1]
            self.h1=self.h1[:1]
            self.h2=self.h2[:1]
            self.mu_cold=4*10**13*exp(-0.046*self.Tstart
)
            self.mu=[self.mu_cold]
            self.T=[self.Tstart]
            self.mu_newt=[self.mu_cold]
            self.shears=[0,0,0,0,0,0]
            self.count=0
            if j==self.maxit-1:
                print(self.du)
                print('no solution for tested range of
dudx0 guesses')

 def autostep(self,n=1):
     while self.auto:
         for i in range(10**(n-1)):
             self.step()
             if not self.auto:
                 break
         self.draw()
         plt.pause(self.delay)
     self.auto = False

 def plot(self):
     plt.rcdefaults()
     plt.ion()
     plt.interactive(False)
     self.fig = plt.figure("Solution")
```

```
        self.fig.clf()
        ax1 = self.fig.add_subplot(3,1,1)
        ax2 = self.fig.add_subplot(3,1,2)
        ax3 = self.fig.add_subplot(3,1,3)

        ax1.set_ylabel('u (m/s)',fontsize=14)
        ax1.set_title('Velocity along preform x-axis',
fontsize=14)
        ax2.set_title('Inner and outer radius of tube along
x-axis',
                      fontsize=14)
        ax2.set_ylabel('h (m)',fontsize=14)
        ax2.set_xlabel('x (m)',fontsize=14)
        plt.tight_layout()
        ax1.plot(self.x,self.y,lw=5,label='u')

        ax2.plot(self.x,self.h1,color=[0,.5,0],lw=5,label='
h1')
        ax2.plot(self.x,self.h2,color=[1,.5,1],lw=5,label='
h2')

        ax3.set_title('Temperature along preform x-axis',
fontsize=14)
        ax3.set_ylabel('T (K)',fontsize=14)
        ax3.set_xlabel('x (m)',fontsize=14)
        ax3.plot(self.x,self.Tgaus,lw=5)

        plt.savefig('solution.png')
        plt.show()

  def muplot(self):
        plt.plot(self.x,self.mu,lw=5,label='Non-Newtonian')
        plt.plot(self.x,self.mu_newt,lw=5,label='Newtonian')
        plt.plot(self.x,self.shears)
        plt.ylabel('Viscosity')
        plt.xlabel('x (m)')
        plt.title('Viscosity difference Newtonian and non-
Newtonian')
        plt.yscale('log')
        plt.legend()
        plt.show()
```

```
    def checkifdone(self):
        self.fi.append(self.y[-1]-self.Ud)
        return (abs(self.y[-1]-self.Ud) < 0.01*self.Ud)

    def shoot(self):
        self.fidg=self.fi[-1]*self.shootpart
        self.Adu.append(self.Adu[-1]-self.fidg)
        return self.Adu

    def d2udx2(self):
        g=self.g
        gam=self.gam
        a=self.a
        rho=self.rho
        cp=self.cp
        Ta=self.Ta
        p0=self.p0
        sig=self.sig
        mu = self.mu[-1]
        dmudz=self.dmudz[-1]
        h1=self.h1[-1]
        h2=self.h2
        u=self.y
        T=self.T[-1]
        dh1dx2=(((p0*h1**2*h2[-1]**2-gam*h1\
                            *h2[-1]*(h1+h2[-1]))/(mu*(h2
  [-1]\
                                    **2-h1**2)))-h1**2*self.
  dy[-1])/(u[-1])

        dh2dx2=(((p0*(h1**2)*(h2[-1]**2)-gam*h1\
                               *h2[-1]*(h1+h2[-1]))/(mu*(h2
  [-1]\
                                    **2-h1**2)))-h2[-1]**2*
  self.dy[-1])/(u[-1])
        self.dh1dx=dh1dx2/(h1*2)
        self.dh2dx=dh2dx2/(h2[-1]*2)
        At=(3*mu*(h2[-1]**2-h1**2))
        Bt=rho*(h2[-1]**2-h1**2)*(u[-1]*self.dy[-1]-g)
        Ct=3*dmudz*(h2[-1]**2-h1**2)*self.dy[-1]
```

```
     Dt=3*mu*(dh2dx2-dh1dx2)*self.dy[-1]
     Et=gam*(self.dh1dx+self.dh2dx)
     self.mucalc()

     self.d2udx22=(Bt-Et-Ct-Dt)/At
     return self.d2udx22

 def Tgauss(self):
     self.currentX=self.currentX+1
     m1=75
     m2=800
     t1=30
     t2=70
     Ta=self.Ta-self.Tstart
     Tb=self.Ta-self.Tglass
     self.T.append(self.Ta-Ta/(1+exp((self.currentX-m1)/
t1))-Tb/\
                   (1+exp((-self.currentX+m2)/t2)))
     if self.currentX==999: self.currentX=0
     self.Tgaus=self.T
     return self.T

 def mucalc(self):
     n = 0.82
     a = 4*10**13
     b = -0.046
     if self.count >4:
         mu_newt = a * exp(b * self.T[-1])
         shears = (self.h2[-2]-self.h2[-1]) / self.dx**2
         if shears <= 0:
             shears=self.shears[-1]
             self.mu.append(mu_newt * (shears ** (n-1)))
         else:
             self.mu.append(mu_newt * (shears ** (n-1)))
         self.shears.append(shears)
     else:
         mu_newt = a * exp(b * self.T[-1])
         self.mu.append(mu_newt)
         self.count = self.count + 1
     self.mu_newt.append(a * exp(b * self.T[-1]))
```

```
graph = Fitt_solver()
```

# Appendix B

# Datasheets for ABS, PC, PLA, PMMA

## B.1 ABS

The data in Table B.1 shows material properties for ABS 3D printing filament. This is not the datasheet from the exact material used for this project, as only limited data was available for the material used. The properties given are therefore an average range as given by an online database for material properties.

TABLE B.1: Material properties for ABS, data taken from [160; 161].

| **Mechanical** | |
|---|---|
| Modulus of Elasticity | $1000 - 2650 MPa$ |
| Tensile Strength at yield | $13 - 65 MPa$ |
| Notched impact strength at 23 °C | $10.5 kJ/m^2$ |
| | |
| **Thermal** | |
| Glass transition temperature | 108-109 °C |
| Thermal Conductivity | $0.15 - 0.2 W/(K * m)$ |
| | |
| **Optical** | |
| Refractive index | Not applicable |

## B.2 PC

The data in Table B.2 shows the material properties of the PC purchased from Ensinger, used for the capillary drawing experiments and extrusion of jacket tubes in Chapter 4.

TABLE B.2: Material properties for PC, data taken from [162].

| **Mechanical** | |
|---|---|
| Modulus of Elasticity | $2300 MPa$ |
| Tensile Strength at yield | $> 60 MPa$ |
| Notched impact strength at 23 °C | $50 kJ/m^2$ |
| | |
| **Thermal** | |
| Thermal Expansion (23-60 °C) | $6.8 * 10^{-5} K^{-1}$ |
| Thermal Conductivity | $0.2 W/(K * m)$ |
| | |
| **Optical** | |
| Refractive index | 1.586 |

## B.3 PLA

The data in Table B.3 shows material properties for ABS 3D printing filament. This is not the datasheet from the exact material used for this project, as only limited data was available for the material used. The properties given are therefore an average as given by an online database for material properties.

TABLE B.3: Material properties for PLA, data taken from [160].

| **Mechanical** | |
|---|---|
| Modulus of Elasticity | $2790 MPa$ |
| Tensile Strength at yield | $36.3 MPa$ |
| Notched impact strength at 23 °C | $1.39 J/cm^2$ |
| | |
| **Thermal** | |
| Glass transition temperature | 51.4 °C |
| | |
| **Optical** | |
| Refractive index | Not applicable |

## B.4 PMMA

The data in Table B.4 shows the material properties for the PMMA rods purchased from RS components that were drawn into filament that was used for 3D printing. The tubes for the capillary drawing experiment in Chapter 4 were also bought from RS components.

Table B.4: Material properties for PMMA, data taken from [163; 164; 78].

| | |
|---|---|
| **Mechanical** | |
| Modulus of Elasticity | $3200MPa$ |
| Tensile Strength | $65MPa$ |
| Notched impact strength at 23 °C | $2kJ/m^2$ |
| | |
| **Thermal** | |
| Thermal Expansion (23-60 °C) | $9 * 10^{-5}K^{-1}$ |
| Thermal Conductivity | $0.19W/(K * m)$ |
| | |
| **Optical** | |
| Refractive index | 1.491 |

# Bibliography

[1] "Cisco visual networking index: Forecast and methodology, 20162021." `https://www.cisco.com/c/en/us/solutions/collateral/service-provider/visual-networking-index-vni/complete-white-paper-c11-481360.html`. Document ID: 1465272001663118.

[2] E. A. J. Marcatili and R. A. Schmeltzer, "Hollow metallic and dielectric waveguides for long distance optical transmission and lasers," *Bell System Technical Journal*, vol. 43, no. 4, pp. 1783–1809, 1964.

[3] R. Carter, P. Jaworski, F. Yu, W. Belardi, W. Wadsworth, A. Urich, and D. S. D.P. Hand, J.C. Knight, "Applications of microstructured negative curvature fibre, for high power and mid-ir transmission," 9 2014.

[4] F. Benabid, J. C. Knight, G. Antonopoulos, and P. S. J. Russell, "Stimulated raman scattering in hydrogen-filled hollow-core photonic crystal fiber," *Science*, vol. 298, no. 5592, pp. 399–402, 2002.

[5] C. Smith, N. Venkataraman, M. Gallagher, D. Muller, J. West, N. Borrelli, D. Allan, and K. Koch, "Low-loss hollow-core silica/air photonic bandgap fibre," *Nature*, vol. 424, no. 6949, pp. 657–659, 2003. 10.1038/nature01849.

[6] A. Argyros, M. A. van Eijkelenborg, M. C. Large, and I. M. Bassett, "Hollow-core microstructured polymer optical fiber," *Opt. Lett.*, vol. 31, pp. 172–174, Jan 2006.

[7] S.-f. Gao, Y.-y. Wang, W. Ding, D.-l. Jiang, S. Gu, X. Zhang, and P. Wang, "Hollow-core conjoined-tube negative-curvature fibre with ultralow loss," *Nature Communications*, vol. 9, no. 1, p. 2828, 2018.

[8] B. J. Mangan, L. Farr, A. Langford, P. J. Roberts, D. P. Williams, F. Couny, M. Lawman, M. Mason, S. Coupland, R. Flea, H. Sabert, T. A. Birks, J. C. Knight, and P. S. J. Russell, "Low loss (1.7 db/km) hollow core photonic bandgap fiber," in *Optical Fiber Communication Conference, 2004. OFC 2004*, vol. 2, pp. 3 pp. vol.2–, Feb 2004.

[9] F. Poletti, N. Wheeler, M. Petrovich, N. Baddela, E. N. Fokoua, J. Hayes, D. Gray, Z. Li, R. Slavík, and D. Richardson, "Towards high-capacity fibre-optic communications at the speed of light in vacuum," *Nature Photonics*, vol. 7, no. 4, p. 279, 2013.

[10] T. Bradley, J. Hayes, Y. Chen, G. Jasion, S. Sandoghchi, R. Slavik, E. Fokoua, S. Bawn, H. Sakr, I. Davidson, A. Taranta, J. Thomas, M. Petrovich, D. Richardson, and F. Poletti, "Record low-loss 1.3db/km data transmitting antiresonant hollow-core fibre," in *Optical Communication (ECOC), 2018 European Conference on*, pp. 1–3, September 2018.

[11] F. Rengier, A. Mehndiratta, H. von Tengg-Kobligk, C. M. Zechmann, R. Unterhinninghofen, H.-U. Kauczor, and F. L. Giesel, "3d printing based on imaging data: review of medical applications," *International Journal of Computer Assisted Radiology and Surgery*, vol. 5, pp. 335–341, Jul 2010.

[12] J. Klein, M. Stern, G. Franchin, M. Kayser, C. Inamura, S. Dave, J. Weaver, P. Houk, P. Colombo, M. Yang, and N. Oxman, "Additive manufacturing of optically transparent glass," *3D Printing and Additive Manufacturing*, vol. 2, no. 3, pp. 92–105, 2015.

[13] F. Kotz, K. Arnold, W. Bauer, D. Schild, N. Keller, K. Sachsenheimer, T. M. Nargang, C. Richter, D. Helmer, and B. E. Rapp, "Three-dimensional printing of transparent fused silica glass," *Nature*, vol. 544, no. 7650, p. 337, 2017.

[14] D. W. Vogt and R. Leonhardt, "3d-printed broadband dielectric tube terahertz waveguide with anti-reflection structure," *Journal of Infrared, Millimeter, and Terahertz Waves*, vol. 37, pp. 1086–1095, Nov 2016.

[15] L. Thrane, R. Jacobsen, P. U. Jepsen, and S. Keiding, "Thz reflection spectroscopy of liquid water," *Chemical Physics Letters*, vol. 240, no. 4, pp. 330 – 333, 1995.

[16] N. Nagai, R. Kumazawa, and R. Fukasawa, "Direct evidence of inter-molecular vibrations by thz spectroscopy," *Chemical Physics Letters*, vol. 413, no. 4, pp. 495 – 500, 2005.

[17] F. Benabid and P. Roberts, "Linear and nonlinear optical properties of hollow core photonic crystal fiber," *Journal of Modern Optics*, vol. 58, no. 2, pp. 87–124, 2011.

[18] Y. Chen, Z. Liu, S. Sandoghchi, G. Jasion, T. D. Bradley, E. Numkam, J. R. Hayes, N. V. Wheeler, D. R. Gray, B. J. Mangan, R. Slavík, F. Poletti, M. N. Petrovich, and D. J. Richardson, "Demonstration of an 11km hollow core photonic bandgap fiber for broadband low-latency data transmission," in *Optical Fiber Communication Conference Post Deadline Papers*, p. Th5A.1, Optical Society of America, 2015.

[19] M. Kuschnerov, V. A. Sleiffer, Y. Chen, E. de Man, Y. Chen, Z. Liu, S. R. Sandoghchi, G. T. Jasion, T. Bradley, E. N. Fokoua, *et al.*, "Data transmission through up to 74.8 km of hollow-core fiber with coherent and direct-detect transceivers," in *Optical Communication (ECOC), 2015 European Conference on*, pp. 1–3, IEEE, 2015.

[20] F. Poletti, "Nested antiresonant nodeless hollow core fiber," *Opt. Express*, vol. 22, pp. 23807–23828, Oct 2014.

[21] E. N. Fokoua, *Ultralow loss and wide bandwidth hollow-core photonic bandgap fibres for telecom applications.* PhD thesis, University of Southampton, 2015.

[22] M. Michieletto, *Hollow core fibers for high power laser applications.* PhD thesis, Technical University of Denmark, 2016.

[23] M. Michieletto, J. K. Lyngsø, C. Jakobsen, J. Lægsgaard, O. Bang, and T. T. Alkeskjold, "Hollow-core fibers for high power pulse delivery," *Optics express*, vol. 24, no. 7, pp. 7103–7119, 2016.

[24] J. M. Fini, J. W. Nicholson, B. Mangan, L. Meng, R. S. Windeler, E. M. Monberg, A. DeSantolo, F. V. DiMarcello, and K. Mukasa, "Polarization maintaining single-mode low-loss hollow-core fibres," *Nature communications*, vol. 5, p. 5085, 2014.

[25] H. K. Kim, M. J. Digonnet, and G. S. Kino, "Air-core photonic-bandgap fiber-optic gyroscope," *Journal of lightwave technology*, vol. 24, no. 8, p. 3169, 2006.

[26] M. Digonnet, S. Blin, H. K. Kim, V. Dangui, and G. Kino, "Sensitivity and stability of an air-core fibre-optic gyroscope," *Measurement Science and Technology*, vol. 18, no. 10, p. 3089, 2007.

[27] F. Benabid, P. Light, F. Couny, and P. S. J. Russell, "Electromagnetically-induced transparency grid in acetylene-filled hollow-core pcf," *Optics express*, vol. 13, no. 15, pp. 5694–5703, 2005.

[28] S.-J. Im, A. Husakou, and J. Herrmann, "High-power soliton-induced supercontinuum generation and tunable sub-10-fs vuv pulses from kagome-lattice hc-pcfs," *Opt. Express*, vol. 18, pp. 5367–5374, Mar 2010.

[29] J. M. Fini, "Microstructure fibres for optical sensing in gases and liquids," *Measurement Science and Technology*, vol. 15, no. 6, p. 1120, 2004.

[30] B. M. Fischer, M. Walther, and P. U. Jepsen, "Far-infrared vibrational modes of dna components studied by terahertz time-domain spectroscopy," *Physics in Medicine & Biology*, vol. 47, no. 21, p. 3807, 2002.

[31] F. Lord Rayleigh, "Xviii. on the passage of electric waves through tubes, or the vibrations of dielectric cylinders," *The London, Edinburgh, and Dublin Philosophical Magazine and Journal of Science*, vol. 43, no. 261, pp. 125–132, 1897.

[32] K. S. Packard, “The origin of waveguides: A case of multiple rediscovery,” *IEEE Transactions on Microwave Theory and Techniques*, vol. 32, pp. 961–969, September 1984.

[33] P. Yeh, A. Yariv, and E. Marom, “Theory of bragg fiber∗,” *J. Opt. Soc. Am.*, vol. 68, pp. 1196–1201, Sep 1978.

[34] P. Yeh and A. Yariv, “Bragg reflection waveguides,” *Optics Communications*, vol. 19, no. 3, pp. 427 – 430, 1976.

[35] E. Garmire, T. McMahon, and M. Bass, “Flexible infrared waveguides for high-power transmission,” *IEEE Journal of Quantum Electronics*, vol. 16, pp. 23–32, January 1980.

[36] E. Yablonovitch, “Inhibited spontaneous emission in solid-state physics and electronics,” *Phys. Rev. Lett.*, vol. 58, pp. 2059–2062, May 1987.

[37] J. Broeng, D. Mogilevstev, S. Barkou, and A. Bjarklev, “Photonic crystal fibers: A new class of optical waveguides,” *Optical Fiber Technology*, vol. 5, no. 3, pp. 305 – 330, 1999.

[38] R. F. Cregan, B. J. Mangan, J. C. Knight, T. A. Birks, P. S. J. Russell, P. J. Roberts, and D. C. Allan, “Single-mode photonic band gap guidance of light in air,” *Science*, vol. 285, no. 5433, pp. 1537–1539, 1999.

[39] N. V. Wheeler, A. M. Heidt, N. K. Baddela, E. N. Fokoua, J. R. Hayes, S. R. Sandoghchi, F. Poletti, M. N. Petrovich, and D. J. Richardson, “Low-loss and low-bend-sensitivity mid-infrared guidance in a hollow-core&#x2013;photonic-bandgap fiber,” *Opt. Lett.*, vol. 39, pp. 295–298, Jan 2014.

[40] F. Couny, F. Benabid, and P. S. Light, “Large-pitch kagome-structured hollow-core photonic crystal fiber,” *Opt. Lett.*, vol. 31, pp. 3574–3576, Dec 2006.

[41] F. Poletti, J. R. Hayes, and D. Richardson, “Optimising the performances of hollow antiresonant fibres,” in *37th European Conference and Exposition on Optical Communications*, p. Mo.2.LeCervin.2, Optical Society of America, 2011.

[42] Y. Y. Wang, N. V. Wheeler, F. Couny, P. J. Roberts, and F. Benabid, “Low loss broadband transmission in hypocycloid-core kagome hollow-core photonic crystal fiber,” *Opt. Lett.*, vol. 36, pp. 669–671, Mar 2011.

[43] A. D. Pryamikov, A. S. Biriukov, A. F. Kosolapov, V. G. Plotnichenko, S. L. Semjonov, and E. M. Dianov, “Demonstration of a waveguide regime for a silica hollow - core microstructured optical fiber with a negative curvature of the core boundary in the spectral region &gt; 3.5 $\mu$m,” *Opt. Express*, vol. 19, pp. 1441–1448, Jan 2011.

[44] F. Yu, W. J. Wadsworth, and J. C. Knight, "Low loss silica hollow core fibers for 3–4 $\mu$m spectral region," *Opt. Express*, vol. 20, pp. 11153–11158, May 2012.

[45] A. Kolyadin, A. Kosolapov, A. Pryamikov, A. Biriukov, V. Plotnichenko, and E. Dianov, "Light transmission in negative curvature hollow core fiber in extremely high material loss region," *Opt. Express*, vol. 21, pp. 9514–9519, Apr 2013.

[46] A. Hartung, J. Kobelke, A. Schwuchow, K. Wondraczek, J. Bierlich, J. Popp, T. Frosch, and M. A. Schmidt, "Double antiresonant hollow core fiber – guidance in the deep ultraviolet by modified tunneling leaky modes," *Opt. Express*, vol. 22, pp. 19131–19140, Aug 2014.

[47] W. Belardi and J. Knight, "Hollow antiresonant fibers with reduced attenuation," *Opt. Lett.*, vol. 39, pp. 1853–1856, Apr 2014.

[48] J.-L. Archambault, R. Black, S. Lacroix, and J. Bures, "Loss calculations for antiresonant waveguides," *Lightwave Technology, Journal of*, vol. 11, pp. 416–423, Mar 1993.

[49] X. Zhang, H. Pan, H. Bai, M. Yan, J. Wang, C. Deng, and T. Wang, "Transition of fabry perot and antiresonant mechanisms via a smf-capillary-smf structure," *Opt. Lett.*, vol. 43, pp. 2268–2271, May 2018.

[50] P. Yeh, *Optical Waves in Layered Media.* Wiley, 2004.

[51] P. J. Roberts, F. Couny, H. Sabert, B. J. Mangan, D. P. Williams, L. Farr, M. W. Mason, A. Tomlinson, T. A. Birks, J. C. Knight, and P. S. Russell, "Ultimate low loss of hollow-core photonic crystal fibres," *Opt. Express*, vol. 13, pp. 236–244, Jan 2005.

[52] E. N. Fokoua, F. Poletti, and D. J. Richardson, "Analysis of light scattering from surface roughness in hollow-core photonic bandgap fibers," *Opt. Express*, vol. 20, pp. 20980–20991, Sep 2012.

[53] F. Yu and J. Knight, "Spectral attenuation limits of silica hollow core negative curvature fiber," *Opt. Express*, vol. 21, pp. 21466–21471, Sep 2013.

[54] W. Belardi and J. Knight, "Hollow antiresonant fibers with low bending loss," *Opt. Express*, vol. 22, pp. 10091–10096, Apr 2014.

[55] W. Belardi and J. C. Knight, "Effect of core boundary curvature on the confinement losses of hollow antiresonant fibers," *Opt. Express*, vol. 21, pp. 21912–21917, Sep 2013.

[56] T. Bradley, Y. Wang, M. Alharbi, B. Debord, C. Fourcade-Dutin, B. Beaudou, F. Gerome, and F. Benabid, "Optical properties of low loss (70db/km) hypocycloid-core kagome hollow core photonic crystal fiber for rb and cs based

optical applications," *Lightwave Technology, Journal of*, vol. 31, pp. 2752–2755, Aug 2013.

[57] M. D. Nielsen, N. A. Mortensen, M. Albertsen, J. R. Folkenberg, A. Bjarklev, and D. Bonacinni, "Predicting macrobending loss for large-mode area photonic crystal fibers," *Opt. Express*, vol. 12, pp. 1775–1779, Apr 2004.

[58] H. Renner, "Bending losses of coated single-mode fibers: a simple approach," *Lightwave Technology, Journal of*, vol. 10, pp. 544–551, May 1992.

[59] L. C. Klein, *Sol-Gel Optics: Processing and Applications.* Boston, MA: Springer US, 1994.

[60] S. Nagel, J. MacChesney, and K. Walker, "An overview of the modified chemical vapor deposition (mcvd) process and performance," *IEEE Journal of Quantum Electronics*, vol. 18, pp. 459–476, April 1982.

[61] U. Paek, C. Schroeder, and C. Kurkjian, "Determination of the viscosity of high silica glasses during fibre drawing," vol. 29, pp. 263–266, 12 1988.

[62] X. Cheng and Y. Jaluria, "Feasibility of high speed furnace drawing of optical fibers," *Journal of Heat Transfer*, vol. 126, no. 5, pp. 852–857, 2004. 10.1115/1.1795246.

[63] S. Sandoghchi, *Characterisation of Imperfections in Hollow Core Photonic Bandgap Fibres.* PhD thesis, Opto Electronics Research Centre, Southampton, 2016.

[64] A. S. Webb, F. Poletti, D. J. Richardson, and J. K. Sahu, "Suspended-core holey fiber for evanescent-field sensing," *Optical Engineering*, vol. 46, no. 1, p. 010503, 2007.

[65] X. Feng, A. K. Mairaj, D. W. Hewak, and T. Monro, "Nonsilica glasses for holey fibers," vol. 23, pp. 2046 – 2054, 07 2005.

[66] H. Ebendorff-Heidepriem, Y. Li, and T. M. Monro, "Reduced loss in extruded soft glass microstructured fibre," *Electronics Letters*, vol. 43, pp. 1343–1345, Nov 2007.

[67] K. Wang, "Die swell of complex polymeric systems," in *Viscoelasticity* (J. de Vicente, ed.), ch. 4, Rijeka: IntechOpen, 2012.

[68] H. Ebendorff-Heidepriem and T. M. Monro, "Analysis of glass flow during extrusion of optical fiber preforms," *Opt. Mater. Express*, vol. 2, pp. 304–320, Mar 2012.

[69] K. Kiang, K. Frampton, T. Monro, R. Moore, J. Tucknott, D. Hewak, D. Richardson, and H. Rutt, "Extruded single-mode non-silica glass holey optical fibres," *Electronics Letters*, vol. 38, no. 12, pp. 546–547, 2002.

[70] R. R. Gattass, D. Rhonehouse, D. Gibson, C. C. McClain, R. Thapa, V. Q. Nguyen, S. S. Bayya, R. J. Weiblen, C. R. Menyuk, L. B. Shaw, and J. S. Sanghera, "Infrared glass-based negative-curvature anti-resonant fibers fabricated through extrusion," *Opt. Express*, vol. 24, pp. 25697–25703, Oct 2016.

[71] J. Knight, "Photonic crystal fibres," *Nature*, vol. 424, no. 6950, pp. 847–851, 2003. 10.1038/nature01940.

[72] M. J. Chen, Y. M. Stokes, P. Buchak, D. G. Crowdy, and H. Ebendorff-Heidepriem, "Microstructured optical fibre drawing with active channel pressurisation," *Journal of Fluid Mechanics*, vol. 783, p. 137165, 2015.

[73] A. Fitt, K. Furusawa, T. Monro, C. Please, and D. Richardson, "The mathematical modelling of capillary drawing for holey fibre manufacture," *Journal of Engineering Mathematics*, vol. 43, pp. 201–227, Aug 2002.

[74] G. T. Jasion, J. S. Shrimpton, Y. Chen, T. Bradley, D. J. Richardson, and F. Poletti, "Microstructure element method (msem): viscous flow model for the virtual draw of microstructured optical fibers," *Opt. Express*, vol. 23, pp. 312–329, Jan 2015.

[75] Y. Chen and T. A. Birks, "Predicting hole sizes after fibre drawing without knowing the viscosity," *Opt. Mater. Express*, vol. 3, pp. 346–356, Mar 2013.

[76] G. Jasion, E. N. Fokoua, J. S. Shrimpton, D. J. Richardson, and F. Poletti, "Combined structural and optical modelling tool to optimise design and fabrication of hollow core photonic band gap fibres," in *Optical Communication (ECOC), 2015 European Conference on*, pp. 1–3, June 2015.

[77] R. J. Bartlett, R. Philip-Chandy, P. Eldridge, D. F. Merchant, R. Morgan, and P. J. Scully, "Plastic optical fibre sensors and devices," *Transactions of the Institute of Measurement and Control*, vol. 22, no. 5, pp. 431–457, 2000.

[78] G. B. M. Large, L. Poladian and M. van Eijkelenborg, *Microstructured Polymer Optical Fibres.* Springer, 2008.

[79] A. Argyros, M. A. van Eijkelenborg, M. C. Large, and I. M. Bassett, "Hollow-core microstructured polymer optical fiber," *Optics letters*, vol. 31, no. 2, pp. 172–174, 2006.

[80] F. M. Cox, A. Argyros, and M. C. J. Large, "Liquid-filled hollow core microstructured polymer optical fiber," *Opt. Express*, vol. 14, pp. 4135–4140, May 2006.

[81] J. Sun, W. Zhou, D. Huang, J. Y. H. Fuh, and G. S. Hong, "An overview of 3d printing technologies for food fabrication," *Food and Bioprocess Technology*, vol. 8, pp. 1605–1615, Aug 2015.

[82] K. Cook, J. Canning, S. Leon-Saval, Z. Reid, M. ArafatHossain, J. Comatti, Y. Luo, and G.-D. Peng, "Air-structured optical fiber drawn from a 3d-printed preform," *Optics Letters*, vol. 40, no. 17, pp. 3966–3969, 2015.

[83] D. Pham and R. Gault, "A comparison of rapid prototyping technologies," *International Journal of Machine Tools and Manufacture*, vol. 38, no. 10, pp. 1257 – 1287, 1998.

[84] E. Napadensky, *Inkjet 3D Printing.* 07 2009.

[85] B. C. Gross, J. L. Erkal, S. Y. Lockwood, C. Chen, and D. M. Spence, "Evaluation of 3d printing and its potential impact on biotechnology and the chemical sciences," *Analytical Chemistry*, vol. 86, no. 7, pp. 3240–3253, 2014. PMID: 24432804.

[86] T. Finnes, "High definition 3d printing–comparing sla and fdm printing technologies," *The Journal of Undergraduate Research*, vol. 13, no. 1, p. 3, 2015.

[87] E. Canessa, C. Fonda, and M. Zennaro, "Low-cost 3d printing for science, education sustainable development," *ICTP - The Abdus Salam International Centre for Theoretical Physics*, vol. 1st Edition, 2013.

[88] "Up plus 2." `https://www.tiertime.com/up-plus-2/`. Accessed: 2018-06-08.

[89] "Up plus temperature control (oled)." `http://www2.artaylor.co.uk/store/index.php?route=product/product&path=57&product_id=55/`. Accessed: 2018-06-08.

[90] A. Argyros, "Microstructures in polymer fibres for optical fibres, thz waveguides, and fibre-based metamaterials," *ISRN Optics*, vol. 2013, p. ID 785162, 2013.

[91] K. Nielsen, H. Rasmussen, A. Adam, P. Planken, O. Bang, and P. Jepsen, "Bendable, low-loss topas fibers for the terahertz frequency range," *Optics express*, vol. 17, no. 10, pp. 8592–8601, 2009.

[92] O. P. Database, "Young's Modulus."

[93] O. P. Database, "Glass transition Temperature."

[94] O. P. Database, "Polymer Density."

[95] J. Gooch, *Encyclopedic Dictionary of Polymers.* No. v. 1 in Encyclopedic Dictionary of Polymers, Springer, 2010.

[96] A. I. M. Greer, I. Vasiev, B. Della-Rosa, and N. Gadegaard, "Fluorinated ethylen propylene: a complementary alternative to pdms for nanoimprint stamps," *Nanotechnology*, vol. 27, no. 15, p. 155301, 2016.

[97] K. Balani, V. Verma, A. Agarwal, and R. Narayan, *Biosurfaces: a materials science and engineering perspective.* John Wiley & Sons, 2015.

[98] "Filmetrics refractive index database." Available: `https://www.filmetrics.com/refractive-index-database`. Accessed 5-11-2018.

[99] "Topas advanced polymers." Available: `https://topas.com/sites/default/files/files/optical_e.pdf`. Accessed 5-11-2018.

[100] G. Boisdé and A. Harmer, *Chemical and Biochemical Sensing with Optical Fibers and Waveguides.* Artech House optoelectronics library, Artech House, 1996.

[101] D. H. Auston, K. P. Cheung, and P. R. Smith, "Picosecond photoconducting hertzian dipoles. appl. phys. lett. 45, 284-286," *Applied Physics Letters*, vol. 45, pp. 284 – 286, 09 1984.

[102] M. C. Beard, G. M. Turner, and C. A. Schmuttenmaer, "Terahertz spectroscopy," *The Journal of Physical Chemistry B*, vol. 106, no. 29, pp. 7146–7159, 2002.

[103] W. Withayachumnankul and M. Naftaly, "Fundamentals of measurement in terahertz time-domain spectroscopy," *Journal of Infrared, Millimeter, and Terahertz Waves*, vol. 35, pp. 610–637, Aug 2014.

[104] G. M. Png, R. J. Falconer, B. M. Fischer, H. A. Zakaria, S. P. Mickan, A. P. Middelberg, and D. Abbott, "Terahertz spectroscopic differentiation of microstructures in protein gels," *Opt. Express*, vol. 17, pp. 13102–13115, Jul 2009.

[105] D. Bird, "Attenuation of model hollow-core, anti-resonant fibres," *Opt. Express*, vol. 25, pp. 23215–23237, Sep 2017.

[106] J. Yang, J. Zhao, C. Gong, H. Tian, L. Sun, P. Chen, L. Lin, and W. Liu, "3d printed low-loss thz waveguide based on kagome photonic crystal structure," *Opt. Express*, vol. 24, pp. 22454–22460, Oct 2016.

[107] D. Jahn, M. Weidenbach, J. Lehr, L. Becker, F. Beltrán-Mejía, S. F. Busch, J. C. Balzer, and M. Koch, "3d printed terahertz focusing grating couplers," *Journal of Infrared, Millimeter, and Terahertz Waves*, vol. 38, pp. 708–716, Jun 2017.

[108] A. I. Hernandez-Serrano and E. Castro-Camus, "Quasi-wollaston-prism for terahertz frequencies fabricated by 3d printing," *Journal of Infrared, Millimeter, and Terahertz Waves*, vol. 38, pp. 567–573, May 2017.

[109] A. I. Hernandez-Serrano, E. Castro-Camus, and D. Lopez-Mago, "q-plate for the generation of terahertz cylindrical vector beams fabricated by 3d printing," *Journal of Infrared, Millimeter, and Terahertz Waves*, vol. 38, pp. 938–944, Aug 2017.

[110] A. D. Squires and R. A. Lewis, "Mechanical and optical viability of eighteen filaments for 3d printing of terahertz components," in *2017 42nd International Conference on Infrared, Millimeter, and Terahertz Waves (IRMMW-THz)*, pp. 1–2, Aug 2017.

[111] D. J. Griffiths, *Introduction to electrodynamics; 3d ed.* Boston, MA: Pearson, 2008. Re-published by Cambridge University Press in 2017.

[112] G. Agrawal, *Nonlinear Fiber Optics.* Optics and Photonics, Elsevier Science, 2001.

[113] R. Boyd and D. Prato, *Nonlinear Optics.* Nonlinear Optics Series, Elsevier Science, 2008.

[114] A. Logg, K.-A. Mardal, and G. N. Wells, eds., *Automated Solution of Differential Equations by the Finite Element Method*, vol. 84 of *Lecture Notes in Computational Science and Engineering.* Springer, 2012.

[115] B. A. Rahman and A. Agrawal, *Finite element modeling methods for photonics.* Artech House USA, 2013.

[116] Z. Zhang and S. Satpathy, "Electromagnetic wave propagation in periodic structures: Bloch wave solution of maxwell's equations," *Phys. Rev. Lett.*, vol. 65, pp. 2650–2653, Nov 1990.

[117] B. Rahman and A. Agrawal, *Finite Element Modeling Methods for Photonics.* Optoelectronics, Artech House, 2013.

[118] "Wave Optics Module Users Guide." Comsol Multiphysics.

[119] M. Turner, R. Clough, H. Martin, and L. Topp, "Stiffness and deflection analysis of complex structures," *Journal of the Aeronautical Science*, vol. 23, no. 9, pp. 805–823, 1956.

[120] G. Dhatt, E. Lefrançois, and G. Touzot, *Finite Element Method.* ISTE, Wiley, 2012.

[121] M. K. Haldar, "Introducing the finite element method in electromagnetics to undergraduates using matlab," *International Journal of Electrical Engineering Education*, vol. 43, no. 3, pp. 232–244, 2006.

[122] J. P. Webb, "Application of the finite-element method to electromagnetic and electrical topics," *Reports on Progress in Physics*, vol. 58, no. 12, p. 1673, 1995.

[123] S. Ahmed, "Finite-element method for wavaguide problems," *Electronic Letters*, vol. 4, pp. 387–389, 1968.

[124] M. Saitoh and K. Koshiba, "Numerical verification of degeneracy in hexagonal photonic crystal fibers," *IEEE Photonics Technology Letters*, vol. 13, no. 12, pp. 1313–1315, 2001.

[125] J. Jin, *The Finite Element Method in Electromagnetics.* John Wiley  Sons, 2015.

[126] *Implementation of the Perfectly Matched Layer to Determine the Quality Factor of Axisymmetric Resonators in COMSOL*, 2010.

[127] Z. Sacks, D. Kingsland, R. Lee, and J.-F. Lee, “A perfectly matched anisotropic absorber for use as an absorbing boundary condition,” *Antennas and Propagation, IEEE Transactions on*, vol. 43, pp. 1460–1463, Dec 1995.

[128] I. The MathWorks, “Matlab 2012b.”

[129] M. Habib, O. Bang, and M. Bache, “Low-loss hollow-core anti-resonant fibers with semi-circular nested tubes,” *Selected Topics in Quantum Electronics, IEEE Journal of*, vol. PP, no. 99, pp. 1–1, 2016.

[130] S. Chaudhuri, L. D. V. Putten, F. Poletti, and P. J. A. Sazio, “Low loss transmission in negative curvature optical fibers with elliptical capillary tubes,” *Journal of Lightwave Technology*, vol. 34, pp. 4228–4231, Sept 2016.

[131] L. Vincetti, “Empirical formulas for calculating loss in hollow core tube lattice fibers,” *Opt. Express*, vol. 24, pp. 10313–10325, May 2016.

[132] S. Février, B. Beaudou, and P. Viale, “Understanding origin of loss in large pitch hollow-core photonic crystal fibers and their design simplification,” *Opt. Express*, vol. 18, pp. 5142–5150, Mar 2010.

[133] B. Temelkuran, S. Hart, G. Benoit, J. Joannopoulos, and Y. Fink, “Wavelength-scalable hollow optical fibres with large photonic bandgaps for co2 laser transmission,” *Nature*, vol. 420, no. 6916, pp. 650–653, 2002.

[134] S. Busch, M. Weidenbach, M. Fey, F. Schfer, T. Probst, and M. Koch, “Optical properties of 3d printable plastics in the thz regime and their application for 3d printed thz optics,” *Journal of Infrared, Millimeter, and Terahertz Waves*, vol. 35, no. 12, pp. 993–997, 2014.

[135] ARTaylor.co.uk, “3d printer temperature controller.” `http://www2.artaylor.co.uk/images/pp3dp/Temperature_Control_User_Manual.pdf`, 2014.

[136] M. Gad-el Hak, *The MEMS Handbook*. Mechanical and Aerospace Engineering Series, CRC Press, 2001.

[137] D. H. Cha, H.-J. Kim, H. S. Park, Y. Hwang, J.-H. Kim, J.-H. Hong, and K.-S. Lee, “Effect of temperature on the molding of chalcogenide glass lenses for infrared imaging applications,” *Appl. Opt.*, vol. 49, pp. 1607–1613, Mar 2010.

[138] G. W. S. Blair, J. C. Hening, and A. Wagstaff, “The flow of cream through narrow glass tubes.,” *The Journal of Physical Chemistry*, vol. 43, no. 7, pp. 853–864, 1939.

[139] M. A. Rao, *Flow and Functional Models for Rheological Properties of Fluid Foods*, pp. 27–58. Boston, MA: Springer US, 2007.

[140] Q.-H. Nguyen and N.-D. Nguyen, “Incompressible non-newtonian fluid flows,” in *Continuum Mechanics* (Y. X. Gan, ed.), ch. 3, Rijeka: IntechOpen, 2012.

[141] D. Quemada, P. Flaud, and P. Jezequel, “Rheological properties and flow of concentrated disperse media i - modelling of steady and unsteady behaviour,” *Chemical Engineering Communications*, vol. 32, no. 1-5, pp. 61–83, 1985.

[142] H. Keller, *Numerical Methods for Two-Point Boundary-Value Problems.* Dover Books on Mathematics, Dover Publications, 2018.

[143] T. E. Oliphant, “Python for scientific computing,” *Computing in Science Engineering*, vol. 9, pp. 10–20, May 2007.

[144] K. J. Millman and M. Aivazis, “Python for scientists and engineers,” *Computing in Science Engineering*, vol. 13, pp. 9–12, March 2011.

[145] O. Travis E, “A guide to numpy,” 2006.

[146] J. D. Hunter, “Matplotlib: A 2d graphics environment,” *Computing in Science Engineering*, vol. 9, pp. 90–95, May 2007.

[147] S. C. Xue, M. C. J. Large, G. W. Barton, R. I. Tanner, L. Poladian, and R. Lwin, “Role of material properties and drawing conditions in the fabrication of microstructured optical fibers,” *J. Lightwave Technol.*, vol. 24, p. 853, Feb 2006.

[148] “Pc polycarbonate plastic.” `https://www.ensingerplastics.com/en-gb/shapes/engineering-plastics/pc-polycarbonate`. Accessed: 2018-06-25.

[149] F. Twyman, “The annealing of glass,” *Trans. Faraday Soc.*, vol. 16, pp. 112–113, 1920.

[150] K. Cook, G. Balle, J. Canning, L. Chartier, T. Athanaze, M. A. Hossain, C. Han, J.-E. Comatti, Y. Luo, and G.-D. Peng, “Step-index optical fiber drawn from 3d printed preforms,” *Opt. Lett.*, vol. 41, pp. 4554–4557, Oct 2016.

[151] J. D. Menczel and R. B. Prime, *Thermal analysis of polymers: fundamentals and applications.* John Wiley & Sons, 2014.

[152] B. You and J.-Y. Lu, “Remote and in situ sensing products in chemical reaction using a flexible terahertz pipe waveguide,” *Opt. Express*, vol. 24, pp. 18013–18023, Aug 2016.

[153] N. Laman, S. S. Harsha, and D. Grischkowsky, “Narrow-line waveguide terahertz time-domain spectroscopy of aspirin and aspirin precursors,” *Appl. Spectrosc.*, vol. 62, pp. 319–326, Mar 2008.

[154] M. Naftaly and R. E. Miles, “Terahertz time-domain spectroscopy for material characterization,” *Proceedings of the IEEE*, vol. 95, pp. 1658–1665, Aug 2007.

[155] "Laserquantum, laser quantum, tera-sed, [online]." Available: `http://www.laserquantum.com`. Accessed 11-07-2017.

[156] "Menlosystems, terahertz antennas and components, [online]." Available: `http://www.menlosystems.com/`. Accessed 11-07-2017.

[157] Z. Wang, H. Wu, X. Hu, N. Zhao, Q. Mo, and G. Li, "Rayleigh scattering in few-mode optical fibers," *Nature*, p. 35844, 2016.

[158] M. Born and E. Wolf, *Principles of Optics: Electromagnetic Theory of Propagation, Interference and Diffraction of Light.* Pergamon, 1959.

[159] S. J. Orfanidis, *Electromagnetic Waves and Antennas.* Rutgers University, 2016.

[160] "Abs technical datasheet [online]." Available: `http://www.matweb.com/`, note = Accessed 25-01-2019.

[161] "Ultimaker abs technical datasheet [online]." Available: `https://ultimaker.com/en/resources/49912-abs`. Accessed 25-01-2019.

[162] "Ensinger plastics - polycarbonate [online]." Available: `https://www.ensingerplastics.com/en-gb/shapes/industrial-plastics/polycarbonate`. Accessed 25-01-2019.

[163] "Datasheet acrylic tube [online]." Available: `https://docs-emea.rs-online.com/webdocs/1580/0900766b815803d2.pdf`. Accessed 25-01-2019.

[164] "Datasheet acrylic rod [online]." Available: `https://docs-emea.rs-online.com/webdocs/150f/0900766b8150f6f5.pdf`. Accessed 25-01-2019.

# List of Publications

## 6.5 Articles

L.D. van Putten, J. Gorecki, E. Numkam Fokoua, V. Apostolopoulos, F. Poletti, ”3D-printed polymer antiresonant waveguides for short-reach terahertz applications” in *Applied Optics*, 57, 14, p. 3953-3958, 2018

L. Van Putten, E. Numkam Fokoua, S. Abokhamis Mousavi, W. Belardi, S. Chaudhuri, J.V. Badding, F. Poletti, ”Exploring the effect of the core boundary curvature in hollow antiresonant fibers” in *IEEE Photonics Technology Letters*, 29, 2, p. 263-266, 2017

S. Chaudhuri, L. Van Putten, F. Poletti, P-J. Sazio, ”Low loss transmission in negative curvature optical fibers with elliptical capillary tubes” in *Journal of Lightwave Technology*, 34, 18, p. 4228-4231, 2016

## 6.6 Conferences

M. Posner, A. Jantzen, L. Van Putten, A. Ravagli, A.L. Donko, N. Soper, N.H.L. Wong, P. John, ”Cathedral outreach: student-led workshops for school curriculum enhancement in non-traditional environments” in *SPIE PROCEEDINGS: 14th Conference on Education and Training in Optics and Photonics: ETOP 2017*, 2017

L.D. van Putten, G. Jasion, N.M. White, J. Lousteau, F. Poletti, ”Modelling the behaviour of Non-Newtonian materials for Capillary Drawing” in *SPIE FOCUS Conference Optics and Photonics Technologies*, 2018

M.T. Posner, P.V. John, D. Standen, N.V. Wheeler, L. Van Putten, N. Soper, T.L. Parsonage, N.H.L. Wong, G. Brambilla, ”Reflecting photonics: reaching new audiences through new partnerships IYL 2015 and the Royal Horticultural Society Flower Show” in *SPIE Optical Engineering + Applications Symposium (9946), Optics Education and*

*Outreach IV*, 2016

L.D. van Putten, E. Numkam Fokoua, S. Abokhamis Mousavi , W. Belardi, F. Poletti, ”Optimizing the Curvature of Elliptical Cladding Elements to Reduce Leakage Loss in Antiresonant Hollow Core Fibres” in *ECOC 2016 - 42nd European Conference and Exhibition on Optical Communication*, 2016

G. Brambilla and L. Van Putten, ”Low-temperature Manufacture of Optical Fibres” in *Workshop on Specialty Optical Fibers and Their Applications*, p. WF1A.2, Optical Society of America, 2015